

7777 FILE COPY

2

RADC-TR-89-198
Final Technical Report
October 1989

AD-A217 011



NEAR-FIELD BISTATIC RCS MEASUREMENTS

The BDM Corporation

Dr. Everett G. Farr, Dr. Robert B. Rogers, Glen R. Salo, Theodore N. Truska

DTIC
ELECTE
JAN 19 1990
S B D

APPROVED FOR PUBLIC RELEASE; DISTRIBUTION UNLIMITED.

ROME AIR DEVELOPMENT CENTER
Air Force Systems Command
Griffiss Air Force Base, NY 13441-5700

90 01 19 011

This report has been reviewed by the RADC Public Affairs Division (PA) and is releasable to the National Technical Information Service (NTIS). At NTIS it will be releasable to the general public, including foreign nations.

RADC-TR-89-198 has been reviewed and is approved for publication.

APPROVED:



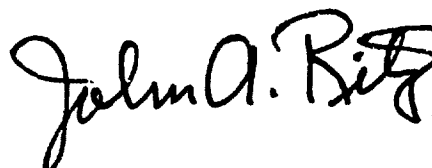
KEITH D. TROTT, MAJ, USAF
Project Engineer

APPROVED:



JOHN K. SCHINDLER
Director of Electromagnetics

FOR THE COMMANDER:



JOHN A. RITZ
Directorate of Plans & Programs

If your address has changed or if you wish to be removed from the RADC mailing list, or if the addressee is no longer employed by your organization, please notify RADC (EECT) Hanscom AFB MA 01731-5000. This will assist us in maintaining a current mailing list.

Do not return copies of this report unless contractual obligations or notices on a specific document require that it be returned.

UNCLASSIFIED

SECURITY CLASSIFICATION OF THIS PAGE

REPORT DOCUMENTATION PAGE				Form Approved OMB No. 0704-0188	
1a. REPORT SECURITY CLASSIFICATION UNCLASSIFIED			1b. RESTRICTIVE MARKINGS N/A		
2a. SECURITY CLASSIFICATION AUTHORITY N/A			3. DISTRIBUTION/AVAILABILITY OF REPORT Approved for public release; distribution unlimited.		
2b. DECLASSIFICATION/DOWNGRADING SCHEDULE N/A			5. MONITORING ORGANIZATION REPORT NUMBERS		
4. PERFORMING ORGANIZATION REPORT NUMBERS BDM/ABO-88-0996-TR			RADC-TR-89-198		
6a. NAME OF PERFORMING ORGANIZATION The BDM Corporation		6b. OFFICE SYMBOL (If applicable)	7a. NAME OF MONITORING ORGANIZATION Rome Air Development Center (EECT)		
6c. ADDRESS (City, State, and ZIP Code) 1901 Randolph Rd SE Albuquerque NM 87106		7b. ADDRESS (City, State, and ZIP Code) Hanscom AFB MA 01731-5000			
8a. NAME OF FUNDING/SPONSORING ORGANIZATION Rome Air Development Center		8b. OFFICE SYMBOL (If applicable) EECT	9. PROCUREMENT INSTRUMENT IDENTIFICATION NUMBER P19628-86-C-0208		
6c. ADDRESS (City, State, and ZIP Code) Hanscom AFB MA 01731-5000		10. SOURCE OF FUNDING NUMBERS			
		PROGRAM ELEMENT NO 61102F	PROJECT NO. 2305	TASK NO. J4	WORK UNIT ACCESSION NO. 60
11. TITLE (Include Security Classification) NEAR-FIELD BISTATIC RCS MEASUREMENTS					
12. PERSONAL AUTHOR(S) Dr. Everett G. Farr, Dr. Robert B. Rogers, Glen R. Salo, Theodore N. Truske					
13a. TYPE OF REPORT Final		13b. TIME COVERED FROM Sep 86 to Mar 89		14. DATE OF REPORT (Year, Month, Day) October 1989	
15. PAGE COUNT 176					
16. SUPPLEMENTARY NOTATION N/A					
17. COSATI CODES			18. SUBJECT TERMS (Continue on reverse if necessary and identify by block number)		
FIELD	GROUP	SUB-GROUP	Near-Field RCS measurement; Planar near-field scanning; Bistatic radar cross-section (BRCS); Plan wave scattering matrix (PWSM)		
09	03				
09	06				
19. ABSTRACT (Continue on reverse if necessary and identify by block number) The Final Technical Report presents the results of a feasibility investigation of a technique for calculating the far-field radar cross section of an object based upon measurements made in the near-field of the object. This technique is an extension of existing planar near-field antenna measurement technology, and is capable of measuring monostatic radar cross section and bistatic radar cross section at both narrow and wide angles. Included are the detailed formulation of the theory of near-field planar bistatic radar cross section measurement, and discussion of details of the mechanical scanner and software implementations. The comparison of measurement with prediction is presented; the agreement is excellent, and suggests that a larger scale demonstration would be appropriate. Also included are concepts for reducing the amount of data required from reconstructing radar cross section, and a discussion of limitations of this method of radar cross section measurement. (Continued on reverse)					
20. DISTRIBUTION/AVAILABILITY OF ABSTRACT <input type="checkbox"/> UNCLASSIFIED/UNLIMITED <input checked="" type="checkbox"/> SAME AS RPT <input type="checkbox"/> DTIC USERS			21. ABSTRACT SECURITY CLASSIFICATION UNCLASSIFIED		
22a. NAME OF RESPONSIBLE INDIVIDUAL Keith D. Trott, Maj, USAF			22b. TELEPHONE (Include Area Code) (617) 377-4239		22c. OFFICE SYMBOL RADC (EECT)

DD Form 1473, JUN 86

Previous editions are obsolete.

SECURITY CLASSIFICATION OF THIS PAGE

UNCLASSIFIED

UNCLASSIFIED

Item 19 Continued:

Specific recommendations are presented for technology development areas that should be pursued to mature this measurement technique into a viable, operational technology. Among these areas are calibration, data handling, computational optimization, data analysis, operational considerations, and additional theoretical development.

UNCLASSIFIED

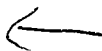
SUMMARY

This Final Technical Report presents the results of a feasibility investigation of a technique for calculating the far-field radar cross section of an object based upon measurements made in the near-field of the object. This technique is an extension of existing planar near-field antenna measurement technology, and is capable of measuring monostatic radar cross section and bistatic radar cross section at both narrow and wide angles.

Included are the detailed formulation of the theory of near-field planar bistatic radar cross section measurement, and discussion of details of the mechanical scanner and software implementation. The comparison of measurement with predictions is presented; the agreement is excellent, and suggests that a larger-scale demonstration would be appropriate. Also included are concepts for reducing the amount of data required for reconstructing radar cross section, and a discussion of limitations of this method of radar cross-section measurement.

Specific recommendations are presented for technology development areas that should be pursued to mature this measurement technique into a viable, operational technology. Among those areas are calibration, data handling, computational optimization, data analysis, operational considerations, and additional theoretical development.

(KR)



Accession For	
NTIS GRA&I	<input checked="" type="checkbox"/>
DTIC TAB	<input type="checkbox"/>
Unannounced	<input type="checkbox"/>
Justification	
By	
Distribution/	
Availability Codes	
Dist	Avail and/or Special
A-1	

FOREWORD

The BDM Corporation, 1801 Randolph Road SE, Albuquerque, NM 87106, is pleased to submit this report, titled "Final Technical Report for Near-Field Bistatic RCS Measurement," to the Rome Air Development Center as required by CDRL DI-A-3591A/M.

This document presents a description of the work performed under contract number F19628-86-C-0208 during the period of September 30, 1986 to March 20, 1989.

TABLE OF CONTENTS

Chapter		Page
I	INTRODUCTION	I-1
II	FORMULATION OF NEAR-FIELD THEORY	II-1
	A. INTRODUCTION	II-1
	B. SCATTERING MATRIX	II-1
	C. MEASUREMENTS	II-3
	D. OUTLINE OF SOLUTION	II-4
	E. CALCULATING $\hat{F}_1(\hat{R}, \hat{K})$	II-5
	F. COMPUTING $\hat{F}_2(\hat{R}, \hat{K})$	II-7
	G. VECTOR COUPLING PRODUCE	II-8
	H. CALCULATING THE SCATTERING MATRIX	II-9
III	DEVELOPMENT OF SOFTWARE TO COMPUTE SCATTERING	III-1
	A. INTRODUCTION	III-1
	B. DFT ORIGIN AND PHASE SHIFT	III-1
	C. DISCUSSION OF CALCULATED SCATTERING MATRIX	III-3
	D. GRIDDED VALUES OF \hat{K} AND \hat{L}	III-4
	E. SIGNAL PROCESSING	III-5
	F. OVER-SAMPLING	III-6
	G. DIGITIZATION RATE	III-7
	H. PHASE WRAP DETECTION	III-8
	I. SPATIAL FILTERING	III-15
	J. POWER SPECTRUM ANALYSIS	III-17
IV	DESIGN AND CONSTRUCTION OF SCANNER	IV-1
	A. SCAN TABLE	IV-1
	B. PROBE ANTENNAS	IV-1
	C. SCAN PATTERNS	IV-3
	D. MEASUREMENT CONFIGURATION	IV-3
	E. DATA ACQUISITION SYSTEM	IV-3
V	COMPARISON OF MEASUREMENTS WITH SOLUTIONS	V-1
	A. INTRODUCTION	V-1
	B. COHERENT BACKGROUND SUBTRACTION	V-1
	C. DATA TAPERING	V-4
	D. PROBE-PROBE COUPLING	V-11
	E. REGION OF DEFINITION	V-11
	F. CUT PLOTS	V-16
	G. SUMMARY	V-32

VI	DATA REDUCTION INVESTIGATION	VI-1
	A. INTRODUCTION	VI-1
	B. MATRIX OPERATIONS	VI-2
	C. FUNCTIONAL EXPANSION	VI-12
VII	DEFINITION OF MEASUREMENT LIMITATIONS	VII-1
	A. INTRODUCTION	VII-1
	B. DATA ACQUISITION LIMITATIONS	VII-1
	1. Receiver Design	VII-1
	2. Data Storage	VII-3
	3. Existing Technology	VII-5
	C. WIDE-ANGLE BISTATIC RCS	VII-5
	D. CONCLUSIONS	VII-9
VIII	CONCLUSIONS	VIII-1
	A. INTRODUCTION	VIII-1
	B. REALISTIC RCS MEASUREMENT REQUIREMENTS	VIII-2
	C. THEORETICAL BASIS	VIII-3
	D. CALIBRATION	VIII-3
	E. MEASURING THE NECESSARY DATA	VIII-3
	F. DATA ANALYSIS	VIII-6
	G. OPERATIONAL CONSIDERATIONS	VIII-7
	REFERENCES	R-1
Appendix A	COORDINATE SYSTEMS	A-1
	A. COORDINATE SYSTEMS	A-1
	B. COORDINATE SYSTEM TRANSFORMATIONS	A-3
	C. ILLUMINATING PLANE WAVE	A-4
	D. SCATTERED PLANE WAVE	A-6
	E. SCATTERING CALCULATION	A-7
	F. TRANSFORMATION OF SCATTERED WAVE	A-12
Appendix B	PROBE ANTENNAS	B-1
	A. PROBE ANTENNA E-FIELD	B-1
	B. METHOD OF STATIONARY PHASE	B-3
	C. OPEN-ENDED WAVEGUIDE	B-5
	D. PROBE ANTENNA CHARACTERISTIC	B-15
	E. FAR-FIELD OF PYRAMIDAL HORN ANTENNA	B-17
Appendix C	SCATTERING BY CONDUCTING SPHERE	C-1
Appendix D	SCATTERING BY CONDUCTING DISK	D-1

LIST OF FIGURES

Figure		Page
III-1	Gain and Phase (High SNR)	III-9
III-2	Gains and Phase (Low SNR)	III-10
III-3	Real and Imaginary Parts (High SNR)	III-12
III-4	Real and Imaginary Parts (Low SNR)	III-13
III-5	Difference between Real Parts (High SNR versus Low SNR)	III-14
III-6	Smoothing Filter Characteristics	III-19
III-7	Autocorrelation and PSD of Real Part (High SNR)	III-20
III-8	Autocorrelation and PSD of Imaginary Part (High SNR)	III-21
III-9	Autocorrelation and PSD of Real Part (Low SNR)	III-22
III-10	Autocorrelation and PSD of Imaginary Part (Low SNR)	III-23
III-11	Signal Cleanup of Real Part (High SNR)	III-24
III-12	Signal Cleanup of Imaginary Part (High SNR)	III-25
III-13	Signal Cleanup of Real Part (Low SNR)	III-26
III-14	Signal Cleanup of Imaginary Part (Low SNR)	III-27
III-15	PSD of Real and Imaginary Parts after Cleanup (High SNR)	III-28
III-16	PSD of Real and Imaginary Parts after Cleanup (Low SNR)	III-29
IV-1	Scan Table Platforms	IV-2
IV-2	Scan Patterns and Probe Orientations	IV-4
IV-3	FORTTRAN Code for Antenna Measurement Scan Pattern	IV-5
IV-4	FORTTRAN Code for Bistatic Scan Pattern	IV-6
IV-5	Equipment Configuration	IV-7

V-1	Co-polarization Magnitude	V-2
V-2	Co-polarization Background Magnitude	V-3
V-3	Co-polarization after Background Subtraction	V-5
V-4	Co-polarization Imaginary Part before Background Subtraction	V-6
V-5	Co-polarization Imaginary Part after Background Subtraction	V-7
V-6	Co-polarization DFT without Taper	V-8
V-7	Co-polarization DFT with Cosine Taper	V-9
V-8	Co-polarization DFT with Partial Cosine Taper	V-10
V-9	S_θ DFT without Taper	V-12
V-10	S_θ DFT with Cosine Taper	V-13
V-11	S_θ DFT with Partial Cosine Taper	V-14
V-12	S_θ Phase	V-15
V-13	S_θ Phase Cut Along $k_x = 0$	V-17
V-14	Predicted and Measured S_θ Magnitude Cut: $k_x = 0$	V-18
V-15	Predicted and Measured S_ϕ Magnitude Cut: $k_x = 0$	V-19
V-16	Predicted and Measured S_y Magnitude Cut: $k_x = 0$	V-20
V-17	Predicted and Measured S_θ Phase Cut: $k_x = 0$	V-21
V-18	Predicted and Measured S_y Phase Cut: $k_x = 0$	V-22
V-19	Predicted and Measured S_θ Magnitude Cut: $k_y = 65.4$	V-23
V-20	Predicted and Measured S_ϕ Magnitude Cut: $k_y = 65.4$	V-24
V-21	Predicted and Measured S_x Magnitude Cut: $k_y = 65.4$	V-25
V-22	Predicted and Measured S_y Magnitude Cut: $k_y = 55.4$	V-26

V-23	Predicted and Measured S_{θ} Phase Cut: $k_y = 65.4$	V-27
V-24	Predicted and Measured S_{ϕ} Phase Cut: $k_y = 65.4$	V-28
V-25	Predicted and Measured S_x Phase Cut: $k_y = 65.4$	V-29
V-26	Predicted and Measured S_y Phase Cut: $k_y = 65.4$	V-30
VII-1	Synchronous Detector Receiver Design	VII-2
VII-2	Near-field Measurement Timer for Fixed Aperture Antennas	VII-2
VII-3	Data Storage Requirements	VII-4
VII-4	Near-field Measurement Times at 100 Mhz	VII-4
VII-5	Near-field Measurement Times at 500 Mhz	VII-6
VII-6	Near-field Measurement Times at 1 Ghz	VII-6
VII-7	Near-field Measurement Times at 5 Ghz	VII-7
VII-8	Near-field Measurement Times at 10 Ghz	VII-7
A-1	Coordinate Systems	A-2
A-2	Scattering Geometry	A-8
B-1	Open-End Waveguide Geometry	B-2
B-2	Open-End Waveguide Coordinate System for Far-Field	B-6
B-3	Open-End Waveguide Reference Plane	B-8
B-4	Coordinate Conventions for Horn Measurements	B-12
B-5	Pyramidal Horn and Coordinate Systems	B-18
C-1	Coordinate System for Sphere Scattering Prediction	C-2
D-1	Coordinate System for Disk Scattering Prediction	D-2

LIST OF TABLES

Table

Page

VII-1

Practical Target Size Limitations Versus Frequency
Using Current Probe Scanning Techniques

VII-8

CHAPTER I

INTRODUCTION

Radar cross-section (RCS) measurement is an important ingredient of design verification and maintenance of contemporary aircraft and missile systems. RCS is becoming more and more important for both tactical and strategic weapons systems, due in part to increasingly sophisticated radar systems and the resulting need for low-observable aircraft and missiles.

BDM is currently under contract to Rome Air Development Center to validate a technique for calculating far-field monostatic and bistatic RCS using planar measurements in the near-field of a test object. This technique, developed by BDM in 1984, is of increasing relevance to the national need in this area, particularly in view of some of the unique capabilities that the planar near-field technique may provide.

The goal of this contract effort is to demonstrate the feasibility of near-field measurement of bistatic radar cross section. The proposed technical approach is divided into six tasks which may be summarized as follows:

- Task 1: Formulation of probe-corrected near-field RCS theory
- Task 2: Development of software to compute scattering
- Task 3: Design and construction of scanner
- Task 4: Comparison of measurements with solutions
- Task 5: Data reduction investigation
- Task 6: Investigation of method's limitations

Those six tasks are addressed in Chapters II through VII of this final report, while Conclusions are presented in Chapter VIII.

It is important to realize that some of today's RCS measurement requirements simply cannot be met with existing measurement technologies. For example, measuring the RCS of low-observable aircraft is difficult on conventional far-field ranges: the signature is small and hard to measure; range effects (ground and air scattering) degrade

accuracy and repeatability; airborne surveillance during long observation times compromises security; and bistatic RCS is difficult to measure (particularly at small angles).

BDM has been working on near-field RCS measurement and prediction concepts since 1983. In 1984 Mike Dinallo developed and published the mathematical foundations of a proposed near-field RCS (NFRCS) measurement approach which we called "planar near-field RCS measurement." In 1987 Rogers and Farr published the explicit solution to Dinallo's scattering equations and described BDM's ongoing work in near-field RCS measurement.

Our planar NFRCS measurement technology is an outgrowth and extension of the near-field antenna measurement theory and techniques developed by the National Bureau of Standards (NBS) in the 1960s. The NBS theoretical and experimental programs demonstrated that traditional far-field antenna patterns can be calculated based upon pattern data measured in the near-field of an antenna. These results were backed up by extensive error analyses and validation tests of antennas on near-field and far-field ranges. The analyses and tests showed that patterns measured using near-field techniques are more accurate, repeatable, and economical to obtain than patterns measured on traditional antenna ranges. The near-field measurement facilities are also smaller than far-field ranges and are fully enclosed, providing excellent security for sensitive military applications. The NBS near-field antenna measurement methods are now in daily use by most major antenna fabrication and test facilities.

Since 1984 BDM has been extending the NBS near-field antenna measurement theory to include the near-field RCS measurement problem. Our work has been both theoretical and experimental; we have developed the mathematics of near-field RCS measurement and have carried on an active experimental program to validate the mathematics. Our planar near-field RCS measurement technique is the result of this work.

The key feature of this technique is the mathematical algorithm that allows us to efficiently compute the RCS of an object based upon many scattering measurements made near the object. The measurements are conceptually easy to obtain by a computerized data control and acquisition system similar to the one we have prototyped in the BDM Laboratory.

The unknown object is illuminated by a single broad-beam transmitting antenna and the scattered signal from the object is received by one or more receiving antennas. The transmitting and receiving antennas are in the near-field of the object (typically within a few feet of it when using gigahertz frequencies). A computerized data acquisition system controls where the transmit and receiving antennas are placed (using servo control) and measures and stores the received signals. The transmitting and receiving antennas are moved around in a plane (i.e., a planar scan pattern), so our measurement approach is more correctly called near-field bistatic RCS measurement using planar scanning.

Other noteworthy features are that bistatic measurements are feasible both at large and small angles, monostatic measurements are feasible, sensitivity is excellent (so low-observables can be measured), and the measurement facility is totally enclosed (which enhances security).

CHAPTER II

FORMULATION OF NEAR-FIELD THEORY

A. INTRODUCTION

In this chapter we present the analysis of near-field bistatic scattering data. This analysis is based upon Dinallo's [16] formulation of bistatic scattering in terms of the plane wave scattering matrix. Note that for the bulk of this section we carry out the mathematics in the unprimed coordinates of the object under test.

B. SCATTERING MATRIX

The goal is to calculate for an arbitrary object a scattering matrix

$$\underline{\underline{I}}_{11}(\vec{k}, \vec{l}) = \begin{bmatrix} I_{11\theta\theta}(\vec{k}, \vec{l}) & I_{11\theta\phi}(\vec{k}, \vec{l}) \\ I_{11\phi\theta}(\vec{k}, \vec{l}) & I_{11\phi\phi}(\vec{k}, \vec{l}) \end{bmatrix},$$

which describes the scattering of an incident plane wave by that object, and

$$\vec{k} = k_x \hat{e}_x + k_y \hat{e}_y + k_z \hat{e}_z$$

$$\vec{l} = l_x \hat{e}_x + l_y \hat{e}_y + l_z \hat{e}_z.$$

It is worth noting explicitly that the elements of the scattering matrix $\underline{\underline{I}}_{11}(\vec{k}, \vec{l})$ are specified by means of two polarization-related indices and two propagation vectors. For example, $I_{11\theta\phi}(\vec{k}, \vec{l})$ refers to the θ -component of the angular spectrum of the wave that is scattered when the object is illuminated by the ϕ -component of the angular spectrum of the incident wave. The incident wave has propagation vector \vec{l} , and the scattered wave has propagation vector \vec{k} . Taking all four elements together, $\underline{\underline{I}}_{11}(\vec{k}, \vec{l})$ specifies how the θ and ϕ components of the angular spectrum of the incident wave \vec{l} are scattered into θ and ϕ components of the angular spectrum of a scattered wave \vec{k} .

The incident and scattered waves are generally a superposition of plane waves which we will model as a continuum of plane waves. A complicated wavefront illuminating the object may be decomposed into a spectrum of plane waves. Measuring the transverse components E_{ix} and E_{iy} of that E-field in some plane, such as $z = z_0$, the angular

spectrum (of plane waves) is the Fourier transform in the x-y plane

$$\begin{aligned} I_1(\vec{l}) &= I_{1\theta}(\vec{l})\hat{e}_\theta + I_{1\phi}(\vec{l})\hat{e}_\phi \\ &= \iint E_1(\vec{r}') e^{-i\vec{l} \cdot \vec{r}'} d\vec{r}', \end{aligned}$$

where

$$\vec{r}' = r_x \hat{e}_x + r_y \hat{e}_y + z_0 \hat{e}_z.$$

The multitude of plane waves that makes up that angular spectrum of incident plane waves is scattered by the object, yielding an infinity of emergent plane waves whose angular spectrum is

$$\begin{aligned} \vec{I}_2(\vec{k}) &= I_{2\theta}(\vec{k})\hat{e}_\theta + I_{2\phi}(\vec{k})\hat{e}_\phi \\ &= \begin{bmatrix} I_{11\theta\theta}(\vec{k}, \vec{l}) & I_{11\theta\phi}(\vec{k}, \vec{l}) \\ I_{11\phi\theta}(\vec{k}, \vec{l}) & I_{11\phi\phi}(\vec{k}, \vec{l}) \end{bmatrix} \cdot \begin{bmatrix} I_{1\theta}(\vec{l}) \\ I_{1\phi}(\vec{l}) \end{bmatrix}. \end{aligned}$$

Note that the θ - and ϕ -components of the angular spectrum of the scattered plane waves are a linear combination of both the θ - and the ϕ -components of the angular spectrum of the incident plane waves.

For a source at \vec{r}_1 having angular spectrum $\vec{I}_1(\vec{l})$, the scattered angular spectrum at the origin is denoted by $\vec{F}(\vec{r}_1, \vec{k})$, where

$$\begin{aligned} \vec{F}(\vec{r}_1, \vec{k}) &= \begin{bmatrix} F_{\theta}(\vec{r}_1, \vec{k}) \\ F_{\phi}(\vec{r}_1, \vec{k}) \end{bmatrix} \\ &= \iint \begin{bmatrix} I_{11\theta\theta}(\vec{k}, \vec{l}) & I_{11\theta\phi}(\vec{k}, \vec{l}) \\ I_{11\phi\theta}(\vec{k}, \vec{l}) & I_{11\phi\phi}(\vec{k}, \vec{l}) \end{bmatrix} \cdot \begin{bmatrix} I_{1\theta}(\vec{l}) \\ I_{1\phi}(\vec{l}) \end{bmatrix} \cdot e^{-i\vec{l} \cdot \vec{r}_1} d\vec{l}. \end{aligned}$$

(As written here, $\vec{F}(\vec{r}_1, \vec{k})$ is related directly to the sampling plane coordinates rather than the object coordinates.) The far-field scattered \vec{E} at \vec{r}_2 is calculated with the results from a previous section. Hence,

$$\vec{E}_s(\vec{r}_2) = \frac{-2\pi i k \cos \theta}{r_2} e^{+ik \cdot \vec{r}_2} \vec{F}(\vec{r}_2, \vec{k})$$

where \vec{k} is parallel to \vec{r}_2 . If the incident wave is in fact planar, then the angular spectrum

of the incident wave is

$$\vec{I}_1(\vec{I}) = \begin{bmatrix} I_{1\theta} \\ I_{1\phi} \end{bmatrix} \delta(\vec{I} - \vec{I}_1)$$

and the integral above reduces to a matrix multiplication. The far-field scattered E-field is

$$\vec{E}_s(\vec{r}_2) = \frac{-2\pi i \cos\theta}{r_2} \begin{bmatrix} I_{11\theta\theta}(\vec{k}, \vec{I}_1) & I_{11\theta\phi}(\vec{k}, \vec{I}_1) \\ I_{11\phi\theta}(\vec{k}, \vec{I}_1) & I_{11\phi\phi}(\vec{k}, \vec{I}_1) \end{bmatrix} \cdot \begin{bmatrix} I_{1\theta}(\vec{I}) \\ I_{1\phi}(\vec{I}) \end{bmatrix} e^{+i\vec{k} \cdot \vec{r}_2} e^{-i\vec{I} \cdot \vec{r}_1}$$

C. MEASUREMENTS

Given illumination of the test object by the transmit antenna in transmit orientation #1, we will first calculate the θ - and ϕ -components of the scattered angular spectrum over the area scanned by the receive probe antenna in order to calculate the scattering matrix. Next, the transmit probe antenna is rotated 90° to illuminate the test object with a different angular spectrum of plane waves, and we then repeat the measurements and calculations in order to determine the θ - and ϕ -components of the scattered angular spectrum for this second transmit probe antenna orientation. From these two sets of data, we can calculate the manner in which the test object scatters the θ - and ϕ -components of the incident wave into the θ - and ϕ -components of scattered waves.

The laboratory measurements for bistatic near-field scattering consist of gain and phase measurements made by a receive probe as it is swept through a pattern of probe locations. The receive probe scan pattern is swept repeatedly (and gain and phase measurements made) for a set of transmit probe locations, as the transmit probe itself steps through a set of locations in the transmit probe scan pattern.

The transmit probe and receive probe we use are identical, although they need not be so. The receive probe's receiving characteristic

$$\vec{I}_{01}(\vec{k}) = \begin{bmatrix} I_{01\theta}(\vec{k}) \\ I_{01\phi}(\vec{k}) \end{bmatrix},$$

and the transmit probe's transmitting characteristic

$$\vec{I}_{10}(\vec{I}) = \begin{bmatrix} I_{10\theta}(\vec{I}) \\ I_{10\phi}(\vec{I}) \end{bmatrix},$$

are assumed to be known (either analytically or empirically). As in the case of near-field antenna measurements, neither probe antenna should have nulls in a direction \vec{r} for which one wishes to calculate the scattering matrix.

D. OUTLINE OF SOLUTION

In this section we outline the approach we take to determine the scattering matrix $\underline{I}_{11}(\vec{k}, \vec{I})$. The scattering matrix $\underline{I}_{11}(\vec{k}, \vec{I})$ of an object is a tensor of rank two that describes how an incident plane wave (\vec{I}) with arbitrary polarization is scattered by that object and transformed into one or more scattered plane waves (\vec{k}). The scattering of an arbitrary wavefront follows directly, since the superposition principle allows us to create complex wavefronts as a superposition of plane waves.

The scattering object is at the origin, and we define

- \vec{I} = propagation vector of incident wave (from transmit probe),
- \vec{r}_1 = coordinates of source of incident wave (transmit probe),
- \vec{k} = propagation vector of scattered wave (to receive probe), and
- \vec{r}_2 = coordinates of receive probe.

The measurement equation for near-field bistatic RCS is [17]

$$b_o(\vec{r}_1, \vec{r}_2) = \underbrace{\vec{I}_{01}^T(\vec{k})}_{\{5\}} \cdot \underbrace{\left[\underbrace{\int \int \underline{I}_{11}(\vec{k}, \vec{I})}_{\{3\}} \cdot \underbrace{\vec{I}_{10}(\vec{I})}_{\{2\}} e^{-i\vec{I} \cdot \vec{r}_1}_{\{1\}} d\vec{L} \right]}_{\{4\}} e^{+i\vec{k} \cdot \vec{r}_2} d\vec{k} d\vec{L}.$$

The scalar b_o is a measurable quantity that is the complex gain factor describing the transmission path from the transmit probe to the receive probe via the scattering object. The incident wave is represented by the factor {2}. The exponential {1} represents propagation of the incident wave from the transmitting antenna to the object, and the multiplication with {3} represents scattering by the object. The resulting scattered

spectrum of waves propagates {4} from the object to the receive probe; {5} represents the interaction of the propagated, scattered wave with the receiving probe itself. The gain and phase ratios measured by the Hewlett-Packard network analyzer are the values of b_0 .

If we consider the scattering object as a transmitting "antenna," the complicated wavefront generated by it can be represented by a superposition of plane waves. We denote that superposition by $\vec{F}_1(\vec{r}_1, \vec{k})$, where \vec{r}_1 is the location of the actual transmit source and \vec{k} is the wavevector of the scattered plane waves. Since the scattered spectrum is

$$\vec{F}_1(\vec{r}_1, \vec{k}) = \iint \underline{I}_{11}(\vec{k}, \vec{l}) \cdot \vec{l}_{10}(\vec{l}) e^{-i\vec{l} \cdot \vec{r}_1} d\vec{l},$$

the measurement equation above becomes

$$b_0(\vec{r}_1, \vec{r}_2) = \iint \vec{l}_{01}(\vec{k}) \cdot \vec{F}_1(\vec{r}_1, \vec{k}) e^{+i\vec{k} \cdot \vec{r}_2} d\vec{k}.$$

This is the measurement equation for near-field antenna measurement which may be solved to determine $\vec{F}_1(\vec{r}_1, \vec{k})$.

Furthermore, the above two equations are very similar, except that $b_0(\vec{r}_1, \vec{r}_2)$ is a scalar equation while $\vec{F}_1(\vec{r}_1, \vec{k})$ is a vector equation. The techniques of an earlier section can be applied to solving for $\vec{F}_1(\vec{r}_1, \vec{k})$, except that two independent solutions must be found (representing the \hat{e}_θ and \hat{e}_ϕ components of $\vec{F}_1(\vec{r}_1, \vec{k})$).

E. CALCULATING $\vec{F}_1(\vec{r}_1, \vec{k})$

Using the above definition of the scattered spectrum $\vec{F}_1(\vec{r}_1, \vec{k})$, the measurement equation can be written

$$b_{01}(\vec{r}_1, \vec{r}_2) = \iint \vec{l}_{01}(\vec{k}) \cdot \vec{F}_1(\vec{r}_1, \vec{k}) e^{+i\vec{k} \cdot \vec{r}_2} d\vec{k},$$

which is a Fourier integral that can be inverted formally [18] as

$$\vec{l}_{01}(\vec{k}) \cdot \vec{F}_1(\vec{r}_1, \vec{k}) = \frac{1}{4\pi^2} \iint b_{01}(\vec{r}_1, \vec{r}_2) e^{-i\vec{k} \cdot \vec{r}_2} d\vec{r}_2.$$

The integral is over all positions of the receive probe, holding the transmit probe position fixed. Since the receive probe moves in the plane $z = d$ (a constant), we define

$$\vec{R}_2 = r_{2x}\hat{e}_x + r_{2y}\hat{e}_y + d\hat{e}_z,$$

and the integral becomes

$$\vec{I}_{01}(\vec{k}) \cdot \vec{F}_1(\vec{r}_1, \vec{k}) = \frac{e^{-idk_z}}{4\pi^2} \iint b_{01}(\vec{r}_1, \vec{r}_2) e^{-i\vec{k} \cdot \vec{R}_2} d\vec{R}_2.$$

We define the right-hand side of the equation as a coupling product $D_1(\vec{r}_1, \vec{k})$, so

$$\vec{I}_{01}(\vec{k}) \cdot \vec{F}_1(\vec{r}_1, \vec{k}) = D_1(\vec{r}_1, \vec{k}),$$

where $D_1(\vec{r}_1, \vec{k})$ is the calculable quantity

$$\begin{aligned} D_1(\vec{r}_1, \vec{k}) &= \frac{e^{-idk_z}}{4\pi^2} \iint b_{01}(\vec{r}_1, \vec{r}_2) e^{+i\vec{k} \cdot \vec{R}_2} d\vec{R}_2 \\ &= I_{01\phi}(\vec{k})F_{1\phi}(\vec{r}_1, \vec{k}) + I_{01\phi}(\vec{k})F_{1\phi}(\vec{r}_1, \vec{k}). \end{aligned}$$

Let the measurements be repeated with the same transmit probe but with a different receive probe antenna that has receiving characteristic

$$I_{01}'(\vec{k}) = \begin{bmatrix} I_{01}'\phi(\vec{k}) \\ I_{01}'\phi(\vec{k}) \end{bmatrix},$$

obtained by rotating the receive probe by 90° . Calling the new set of measurements $b_{02}(\vec{r}_1, \vec{r}_2)$, we can compute another coupling product $D_2(\vec{r}_1, \vec{k})$ as

$$\begin{aligned} D_2(\vec{r}_1, \vec{k}) &= \frac{e^{-idk_z}}{4\pi^2} \iint b_{02}(\vec{r}_1, \vec{r}_2) e^{-i\vec{k} \cdot \vec{R}_2} d\vec{R}_2 \\ &= I_{01}'\phi(\vec{k})F_{1\phi}(\vec{r}_1, \vec{k}) + I_{01}'\phi(\vec{k})F_{1\phi}(\vec{r}_1, \vec{k}) \end{aligned}$$

If the determinant

$$\Delta_1(\vec{k}) = I_{01\phi}(\vec{k})I_{01}'\phi(\vec{k}) - I_{01}'\phi(\vec{k})I_{01\phi}(\vec{k})$$

is non-zero, then

$$F_{1\phi}(\vec{r}_1, \vec{k}) = \frac{D_1(\vec{r}_1, \vec{k})I_{01\phi}(\vec{r}_1, \vec{k}) - D_2(\vec{r}_1, \vec{k})I_{01\phi}(\vec{r}_1, \vec{k})}{\Delta_1(\vec{r}_1, \vec{k})}$$

$$F_{1\phi}(\vec{r}_1, \vec{k}) = \frac{D_2(\vec{r}_1, \vec{k})I_{01\phi}(\vec{r}_1, \vec{k}) - D_1(\vec{r}_1, \vec{k})I_{01\phi}(\vec{r}_1, \vec{k})}{\Delta_1(\vec{r}_1, \vec{k})}$$

In summary, the transmit probe antenna is in an orientation that we define as "TX orientation #1." For each transmit probe location \vec{r}_1 , we measure an array of scalar values as the receive probe (in RX orientation #1) is moved through its scan pattern. A second array of scalar values is measured with the receive probe rotated by 90° (RX orientation #2). These two arrays of measured data, called $b_{01}(\vec{r}_1, \vec{r}_2)$ and $b_{02}(\vec{r}_1, \vec{r}_2)$, are used to calculate $\vec{F}_1(\vec{r}_1, \vec{k})$. $\vec{F}_1(\vec{r}_1, \vec{k})$ is a vector quantity that is defined for every transmit probe location and every possible \vec{k} .

F. COMPUTING $\vec{F}_2(\vec{r}_1, \vec{k})$

In order to calculate the scattering matrix, it is necessary to determine a second, independent scattered spectrum $\vec{F}_2(\vec{r}_1, \vec{k})$ that represents the scattered spectrum with the object illuminated by a different source spectrum. Since the transmit probe is linearly polarized, we can create a different source spectrum by rotating the transmit probe antenna.

With the transmit probe antenna rotated by 90° (TX orientation #2), we repeat the entire series of measurements and calculations described in the previous section. For each transmit probe location \vec{r}_1 , we measure an array of scalar values as the receive probe (in RX orientation #1) is moved through its scan pattern. A second array of scalar values is measured with the receive probe in RX orientation #2. These two arrays of measured data, called $b_{03}(\vec{r}_1, \vec{r}_2)$ and $b_{04}(\vec{r}_1, \vec{r}_2)$, are used to calculate $\vec{F}_2(\vec{r}_1, \vec{k})$.

The pertinent equations are summarized below:

$$b_{03}(\vec{r}_1, \vec{r}_2) = \iint \vec{r}_{01}^T(\vec{k}) \cdot \vec{F}_2(\vec{r}_1, \vec{k}) e^{+i\vec{k} \cdot \vec{r}_2} d\vec{k},$$

$$\begin{aligned}\vec{I}_{01}(\vec{k}) \cdot \vec{F}_2(\vec{r}_1, \vec{k}) &= \frac{1}{4\pi^2} \iint b_{03}(\vec{r}_1, \vec{r}_2) e^{-i\vec{k} \cdot \vec{r}_2} d\vec{r}_2, \\ &= \frac{e}{4\pi^2} \iint b_{03}(\vec{r}_1, \vec{r}_2) e^{-i\vec{k} \cdot \vec{R}_2} d\vec{R}_2, \\ &\equiv D_3(\vec{r}_1, \vec{k})\end{aligned}$$

or, explicitly,

$$\vec{I}_{01}(\vec{k}) \cdot \vec{F}_2(\vec{r}_1, \vec{k}) = I_{01\theta}(\vec{k}) F_{2\theta}(\vec{r}_1, \vec{k}) + I_{01\phi}(\vec{k}) F_{2\phi}(\vec{r}_1, \vec{k}).$$

Also

$$\begin{aligned}D_4(\vec{r}_1, \vec{k}) &= \frac{e}{4\pi^2} \iint b_{04}(\vec{r}_1, \vec{r}_2) e^{+i\vec{k} \cdot \vec{R}_2} d\vec{R}_2 \\ &= I_{01\theta}(\vec{k}) F_{2\theta}(\vec{r}_1, \vec{k}) + I_{01\phi}(\vec{k}) F_{2\phi}(\vec{r}_1, \vec{k}).\end{aligned}$$

If

$$\Delta_2(\vec{k}) \equiv I_{01\theta}(\vec{k}) I_{01\phi}(\vec{k}) - I_{01\phi}(\vec{k}) I_{01\theta}(\vec{k})$$

is non-zero, then

$$\begin{aligned}F_{2\theta}(\vec{r}_1, \vec{k}) &= \frac{D_3(\vec{r}_1, \vec{k}) I_{01\phi}(\vec{r}_1, \vec{k}) - D_4(\vec{r}_1, \vec{k}) I_{01\theta}(\vec{r}_1, \vec{k})}{\Delta_2(\vec{r}_1, \vec{k})} \\ F_{2\phi}(\vec{r}_1, \vec{k}) &= \frac{D_4(\vec{r}_1, \vec{k}) I_{01\theta}(\vec{r}_1, \vec{k}) - D_3(\vec{r}_1, \vec{k}) I_{01\phi}(\vec{r}_1, \vec{k})}{\Delta_2(\vec{r}_1, \vec{k})}\end{aligned}$$

G. VECTOR COUPLING PRODUCT

Referring to the general bistatic measurement equation

$$b_0(\vec{r}_1, \vec{r}_2) = \iint \vec{I}_{01}(\vec{k}) \cdot \left[\iint \underline{I}_{11}(\vec{k}, \vec{I}) \cdot \vec{I}_{10}(\vec{I}) e^{-i\vec{I} \cdot \vec{r}_1} d\vec{I} \right] e^{+i\vec{k} \cdot \vec{r}_2} d\vec{k} d\vec{I},$$

we have calculated $\vec{F}_1(\vec{r}_1, \vec{k})$ and $\vec{F}_2(\vec{r}_1, \vec{k})$, where

$$\vec{F}_1(\vec{r}_1, \vec{k}) = \iint \underline{I}_{11}(\vec{k}, \vec{I}) \cdot \vec{I}_{10}(\vec{I}) e^{-i\vec{I} \cdot \vec{r}_1} d\vec{I}$$

and

$$\vec{F}_2(\vec{r}_1, \vec{k}) = \iint \underline{I}_{11}(\vec{k}, \vec{I}) \cdot \vec{I}_{10}(\vec{I}) e^{-i\vec{I} \cdot \vec{r}_1} d\vec{I}.$$

are Fourier integrals that may be inverted to give

$$\underline{I}_{11}(\vec{k}, \vec{l}) \cdot \vec{I}_{10}(\vec{l}) = \frac{1}{4\pi^2} \iint \vec{F}_1(\vec{r}_1, \vec{l}) e^{+i\vec{l} \cdot \vec{r}_1} d\vec{r}_1$$

$$\underline{I}_{11}(\vec{k}, \vec{l}) \cdot \vec{I}'_{10}(\vec{l}) = \frac{1}{4\pi^2} \iint \vec{F}_2(\vec{r}_1, \vec{l}) e^{+i\vec{l} \cdot \vec{r}_1} d\vec{r}_1.$$

This time the integrals are over all positions of the transmit probe, holding the receive probe position fixed. Since the transmit probe moves in the plane $z = d$, let

$$\vec{R}_1 = r_{1x}\hat{e}_x + r_{1y}\hat{e}_y + d\hat{e}_z,$$

and the integrals become

$$\underline{I}_{11}(\vec{k}, \vec{l}) \cdot \vec{I}_{10}(\vec{l}) = \frac{e^{+idl_z}}{4\pi^2} \iint \vec{F}_1(\vec{r}_1, \vec{l}) e^{+i\vec{l} \cdot \vec{R}_1} d\vec{R}_1$$

$$\underline{I}_{11}(\vec{k}, \vec{l}) \cdot \vec{I}'_{10}(\vec{l}) = \frac{e^{+idl_z}}{4\pi^2} \iint \vec{F}_2(\vec{r}_1, \vec{l}) e^{+i\vec{l} \cdot \vec{R}_1} d\vec{R}_1.$$

We define a pair of vector coupling products $\vec{Q}(\vec{k}, \vec{l})$ and $\vec{Q}'(\vec{k}, \vec{l})$ as

$$\vec{Q}(\vec{k}, \vec{l}) = \frac{e^{+idl_z}}{4\pi^2} \iint \vec{F}_1(\vec{r}_1, \vec{l}) e^{+i\vec{l} \cdot \vec{R}_1} d\vec{R}_1$$

$$\vec{Q}'(\vec{k}, \vec{l}) = \frac{e^{+idl_z}}{4\pi^2} \iint \vec{F}_2(\vec{r}_1, \vec{l}) e^{+i\vec{l} \cdot \vec{R}_1} d\vec{R}_1,$$

so that we can write

$$\underline{I}_{11}(\vec{k}, \vec{l}) \cdot \vec{I}_{10}(\vec{l}) = \vec{Q}(\vec{k}, \vec{l})$$

$$\underline{I}_{11}(\vec{k}, \vec{l}) \cdot \vec{I}'_{10}(\vec{l}) = \vec{Q}'(\vec{k}, \vec{l}).$$

H. CALCULATING THE SCATTERING MATRIX

Expanding the above equation in components and dropping the explicit (\vec{k}, \vec{l}) dependence,

$$\begin{bmatrix} I_{1c\theta} & I_{10\phi} & 0 & 0 \\ 0 & 0 & I_{1c\theta} & I_{10\phi} \\ I_{12\theta} & I_{10\phi} & 0 & 0 \\ 0 & 0 & I_{12\theta} & I_{10\phi} \end{bmatrix} \cdot \begin{bmatrix} I_{11\theta\theta} \\ I_{11\theta\phi} \\ I_{11\phi\theta} \\ I_{11\phi\phi} \end{bmatrix} = \begin{bmatrix} Q_\theta \\ Q_\phi \\ Q'_\theta \\ Q'_\phi \end{bmatrix}$$

which has solutions:

$$\begin{aligned} I_{11\theta\theta} &= -\frac{Q_{\theta} I_{10\phi} - Q_{\phi} I_{10\theta}}{\Delta} \\ I_{11\theta\phi} &= \frac{Q_{\phi} I_{10\phi} - Q_{\theta} I_{10\phi}}{\Delta} \\ I_{11\phi\theta} &= \frac{Q_{\theta} I_{10\phi} - Q_{\phi} I_{10\theta}}{\Delta} \\ I_{11\phi\phi} &= \frac{Q_{\phi} I_{10\phi} - Q_{\theta} I_{10\phi}}{\Delta} \end{aligned}$$

provided the determinant

$$\Delta \equiv I_{10\theta} I_{10\phi} - I_{10\phi} I_{10\theta}$$

is nonzero for particular (\vec{k}, \vec{l}) . This completes the calculation of the scattering matrix $I_{11}(\vec{k}, \vec{l})$.

Note that all of the above calculations are in the coordinate system of the object under test. When making the actual measurements, one must immediately convert from the coordinates system of the measurement table to that of the object under test.

CHAPTER III

DEVELOPMENT OF SOFTWARE TO COMPUTE SCATTERING

A. INTRODUCTION

The software to perform the scattering calculations is a straightforward implementation of the algorithm presented in the previous chapter. The heart of the software is the two-dimensional fast-Fourier transform subroutine; a number of such subroutines are available in the open literature.

There are a number of software issues stemming from the discretization that is implicitly employed to calculate discrete equivalents to continuous integrals. These issues are discussed in the following sections.

B. DFT ORIGIN AND PHASE SHIFT

In this section we discuss sampled-data evaluation of Fourier integrals by the FFT algorithm. For rigorous discussions refer to the literature [12].

Numerical evaluation of integrals of the form

$$H(\omega) = \int_{-\infty}^{\infty} h(t) e^{i\omega t} dt$$

is feasible for bandlimited $h(t)$ using sampled data and discrete Fourier transform techniques. The continuous function $h(t)$ is sampled at intervals of δt chosen by Nyquist's criterion. The sampled $h(t)$ is a finite sequence

$$\{h'(n) = h(t) \mid t = t_0 + (n-1) \cdot \delta t, n=1, \dots, N\} \\ \equiv h'(1), h'(2), \dots, h'(N)$$

which is implicitly periodic in n with period N . The DFT of $h'(n)$ is

$$H'(k) = \sum_{n=1}^N h'(n) e^{\frac{-2\pi i(n-1)(k-1)}{N}}, k = 1, \dots, N$$

where (for even N)

$$\delta\omega \equiv \frac{2\pi}{N\delta t}$$

$$\omega = \left\{ \begin{array}{ll} (k-1) \delta\omega & k = 1, 2, \dots, \frac{N}{2}+1 \\ [k-(N+1)]\delta\omega & k = \frac{N}{2}+2, \frac{N}{2}+3, \dots, N \end{array} \right\}$$

$$H(\omega) = \delta t \cdot H'(k).$$

For example, with $N=8$,

$$\begin{aligned} H'(1) &= H(+0\delta\omega) \\ H'(2) &= H(+1\delta\omega) \\ H'(3) &= H(+2\delta\omega) \\ H'(4) &= H(+3\delta\omega) \\ H'(5) &= H(+4\delta\omega) = H(-4\delta\omega) \\ H'(6) &= H(-3\delta\omega) \\ H'(7) &= H(-2\delta\omega) \\ H'(8) &= H(-1\delta\omega) \end{aligned}$$

In a sampled-data implementation, Fourier integrals are conveniently calculated using the discrete Fourier transform (DFT) in the form of the Fast Fourier Transform (FFT) algorithm. However, there is a phase shift implicit in the DFT that arises because the origin of the transform is at the first point processed.

We compute the above integral by a summation:

$$\iint f(\vec{R}) e^{i\vec{K} \cdot \vec{R}} d\vec{R} = \delta_x \delta_y \sum_{I_x=1}^{N_x} \sum_{I_y=1}^{N_y} f_s(I_x, I_y) \cdot \exp \left[\pm 2\pi i \frac{(K_x-1)(I_x-1)}{N_x} \right] \cdot \exp \left[\pm 2\pi i \frac{(K_y-1)(I_y-1)}{N_y} \right]$$

where I_x, I_y are indices of a measurement data array, and K_x, K_y are (in this instance only) indices of the transformed data array. I_x and K_x range from 1 to N_x , and I_y and K_y range from 1 to N_y .

Idealizing the sampling process somewhat, the sampled function $f_s(I_x, I_y)$ at given (I_x, I_y) corresponds to the continuous function $f(x, y)$ at the point

$$x = r_{x0} + (I_x-1) \cdot \delta_x,$$

$$y = r_{y0} + (I_y-1) \cdot \delta_y,$$

so

$$f_s(I_x, I_y) = f(r_{x0} + [I_x-1]\delta_x, r_{y0} + [I_y-1]\delta_y).$$

The measurement data array $f_s(\cdot)$ is defined over some set of (I_x, I_y) that does not necessarily include the coordinate system origin. In order that the computed phase be referenced to that origin, a phase factor must be included to specify the phase of the (1,1) point relative to that origin:

$$\sum_{I_x=1}^{N_x} \sum_{I_y=1}^{N_y} f_s(I_x, I_y) \cdot \exp \left[\pm 2\pi i \frac{(K_x - 1)(I_x - 1)}{N_x} \right] \cdot \exp \left[\pm 2\pi i \frac{(K_y - 1)(I_y - 1)}{N_y} \right] \cdot \psi(K_x, K_y)$$

where

$$\psi(K_x, K_y) = \exp \left[\pm 2\pi i \frac{(K_x - 1)\alpha_x}{N_x} \right] \cdot \exp \left[\pm 2\pi i \frac{(K_y - 1)\alpha_y}{N_y} \right],$$

and

$$\alpha_x \equiv r_{ox} / \delta_x,$$

$$\alpha_y \equiv r_{oy} / \delta_y.$$

No modification to the FFT algorithm is required, since the phase factor $\psi(K_x, K_y)$ can be calculated and multiplied into the transformed data array generated by the FFT algorithm.

C. DISCUSSION OF CALCULATED SCATTERING MATRIX

For a given test object, our laboratory measurements and data analysis produce a set of scattering matrices of the form

$$\underline{I}_{11}(\tilde{K}_i, \tilde{L}_i) = \begin{bmatrix} I_{11xx}(\tilde{K}_i, \tilde{L}_i) & I_{11xy}(\tilde{K}_i, \tilde{L}_i) \\ I_{11yx}(\tilde{K}_i, \tilde{L}_i) & I_{11yy}(\tilde{K}_i, \tilde{L}_i) \end{bmatrix},$$

where each matrix consists of four complex scalars (I_{11xx} , I_{11xy} , I_{11yx} , I_{11yy}) that define the scattering matrix for given values of \tilde{K} and \tilde{L} . As before, \tilde{L} is the projection of the incident (illuminating) plane wave propagation vector \tilde{L} onto the x-y plane, and \tilde{K} is the projection of the scattered plane wave propagation vector \tilde{k} onto the x-y plane.

Since the discrete Fourier transform (DFT) is used in the sampled-data implementation of the integrals, \tilde{K} and \tilde{L} can take on only a discrete set of values that are

determined by the measurement grid size, the spatial sampling interval δx , and the "rules" of the DFT. Fourier interpolation can be used to increase the resolution of the grid of values of \tilde{K} and \tilde{L} .

D. GRIDDED VALUES OF \tilde{K} AND \tilde{L}

Suppose the transmit probe scan pattern is a square consisting of N_{tx} points on a side, with spatial sample interval δx . The propagation vector of the transmitted wave (i.e., the plane wave that is incident upon the test object) is denoted by

$$\tilde{\mathbf{I}} = l_x \hat{\mathbf{e}}_x + l_y \hat{\mathbf{e}}_y + l_z \hat{\mathbf{e}}_z,$$

and its projection onto the x-y plane is

$$\tilde{\mathbf{L}} = l_x \hat{\mathbf{e}}_x + l_y \hat{\mathbf{e}}_y.$$

Then the x- and the y-components of $\tilde{\mathbf{I}}$ take on the discrete values

$$l_{x_i} = \left[i - \frac{N_{tx}}{2} \right] \delta k_{tx}, \quad i = 0, 2, \dots, N_{tx}$$

$$l_{y_j} = \left[j - \frac{N_{tx}}{2} \right] \delta k_{tx}, \quad j = 0, 2, \dots, N_{tx}$$

where

$$\delta k_{tx} = \frac{2\pi}{N_{tx} \delta x}$$

is the spacing between adjacent samples in "k-space". The maximum magnitude that l_x or l_y can have is

$$|l_x|_{\max} = |l_y|_{\max} = \frac{\pi}{\delta x}.$$

However, l_x and l_y are constrained by the additional requirement that l_z be real, since

$$l_x^2 + l_y^2 + l_z^2 = \left[\frac{2\pi}{\lambda} \right]^2,$$

and propagating waves correspond to those $\tilde{\mathbf{I}}$ for which l_z is real. If l_x or l_y gets too large, l_z becomes imaginary, so we require

$$l_x^2 + l_y^2 \leq \left[\frac{2\pi}{\lambda} \right]^2.$$

Since λ^{-1} is the highest spatial frequency that can be present due to propagating waves, it is the Nyquist frequency [13] of the signal to be sampled, and the required sampling interval is $\lambda/2$. If the sample interval is indeed $\delta_x = \lambda/2$, the domain of valid (l_{x_i}, l_{y_j}) is a circle in the (i, j) plane that is exactly inscribed in the square defined by

$$\left\{ i = \left[-\frac{N_{tx}}{2}, \frac{N_{tx}}{2} \right], j = \left[-\frac{N_{tx}}{2}, \frac{N_{tx}}{2} \right] \right\},$$

so a fraction $\frac{4-\pi}{\pi} \cong 21\%$ of the computed l_{x_i}, l_{y_j} is not useful to us.

A similar situation exists with regard to the range of values of the propagation vector of the scattered plane wave. Suppose the receive probe pattern is a square with N_{rx} points on a side and spatial sample interval δx . The propagation vector of the scattered wave is denoted by

$$\vec{k} = k_x \hat{e}_x + k_y \hat{e}_y + k_z \hat{e}_z,$$

and its projection onto the x - y plane is

$$\vec{K} = k_x \hat{e}_x + k_y \hat{e}_y.$$

The x - and the y -components of \vec{k} take on the discrete values

$$k_{x_i} = \left[i - \frac{N_{rx}}{2} \right] \delta k_{rx}, \quad i = 0, 2, \dots, N_{rx}$$

$$k_{y_j} = \left[j - \frac{N_{rx}}{2} \right] \delta k_{rx}, \quad j = 0, 2, \dots, N_{rx}$$

where

$$\delta k_{rx} = -\frac{2\pi}{N_{rx} \delta x}$$

$$|k_x|_{\max} = |k_y|_{\max} = \frac{\pi}{\delta x}, \text{ and}$$

$$k_x^2 + k_y^2 \leq \left[\frac{2\pi}{\lambda} \right]^2.$$

E. SIGNAL PROCESSING

Conservative signal processing technique calls for using a sampling interval smaller than the $\lambda/2$ dictated by the Nyquist limit. In the present instance, the physics of the wave propagation very effectively bandlimits the signal by imposing a very sharp cutoff for

spatial frequencies beyond $1/\lambda$. This is in contrast to typical signal acquisition scenarios in which a signal generally has components above f_{Nyquist} ; there one must use a sharp cutoff filter and in addition sample at a somewhat higher rate than the Nyquist theorem requires. We conclude that one should probably use $\delta x < \lambda/2$ by perhaps 5% or so.

Given the good A/D resolution (12 bits), adequate floating-point precision and dynamic range (I.E.E.E. standard floating-point format), and a relatively quiet measurement location, we ignore some of the common reasons for sampling at above the Nyquist frequency, namely quantization and numeric dynamic range.

Since the experimentally-determined scattering matrices are defined at discrete values of \hat{K} and \hat{L} , it is convenient to construct one's theoretical models of scattering such that the precise values of \hat{K} and \hat{L} calculated by the analysis software can be automatically plugged in to yield the theoretical scattering values. From an algorithmic standpoint this corresponds to implementing the theoretical or numerical model of scattering as a subroutine that has as input the values of \hat{K} and \hat{L} for which a theoretical prediction is needed.

F. OVER-SAMPLING

Under ideal conditions the gain and phase signals from the network analyzer need to be sampled only at $\lambda/2$ intervals (or slightly more often if one is near the reactive near-field of the test object). In this application we oversample by a factor of ten. Reasons for this are: (1) noise generated in the electronics for gain and phase detection smears out the spectral content of the signal being measured; (2) a general rule of thumb in digitizing and processing noisy signals is that one should digitize at five to ten times the Nyquist rate; (3) filtering techniques can be used to reduce the (uncorrelated) noise on the signal; and (4) non-linear filtering techniques can be used to detect and correct invalid phase measurements.

The invalid phase measurements occur because the phase detection circuit in the network analyzer updates its output asynchronously with respect to the A/D converter, so

it is possible for the A/D to sample the phase when the circuit is "wrapping" around from +180 to -180 degrees (or vice versa). Measuring extra points allows us to detect and correct the invalid phase values. Spatial filtering to improve signal-to-noise ratio (SNR) is also practical when oversampling is performed.

The figures in this section were constructed using measured data from two x-axis scans (made on 6/4/87) of 10 Ghz bistatic RCS from the 6-inch aluminum sphere. The TX probe was held stationary, and the RX probe was scanned in the +x direction using a 200 hz digitizing clock and the usual probe velocity of 29.8 cm/sec. Sample interval is calculated as 0.149 cm, corresponding to oversampling by a factor of ten at 10 Ghz.

The probes were open-end X-band waveguide with absorber collars to limit low-angle radiation and an absorber barrier between the RX and TX probes to limit direct probe-to-probe coupling. The TX probe was driven with a 20-watt (nominal) traveling-wave tube (TWT) amplifier, and a preamplifier was used on the RX probe.

A high SNR scan was obtained using maximum drive to the TWT amplifier. A low SNR scan was obtained immediately after the high SNR scan but with the TWT drive level reduced by 15 db. Additional measurement noise was introduced by the lowered reference channel signal at the network analyzer.

G. DIGITIZATION RATE

Since the quantity of data required by the near-field technique is already formidable, it is preferable to store the minimum number of values necessary for the reconstruction of the scattering matrix. The signal being measured contains no components above spatial frequency

$$f_{\text{signal,max}} = \frac{1}{\lambda} \text{ cycles/meter,}$$

so digitizing the signal at a sampling frequency of $2/\lambda$ samples/meter would theoretically capture all of the spectral content of the signal. For reasons mentioned above, digitizing at ten times this rate is more appropriate, so we choose:

$$f_s = \frac{20}{\lambda} \text{ samples/meter.}$$

Then

$$\begin{aligned}\delta x &= \delta y = \frac{1}{f_s} \text{ meter/sample} \\ &= \frac{\lambda}{20}\end{aligned}$$

and

$$f_{\text{Nyquist}} = \frac{1}{10\lambda} \text{ cycles/meter}$$

is the highest spatial frequency that can be detected without aliasing.

The bandwidth of the network analyzer's gain and phase detection circuits is 10 kHz, so samples should be taken at intervals

$$\begin{aligned}\delta t &>> \frac{1}{10 \text{ kHz}} \\ &>> 0.1 \text{ ms}\end{aligned}$$

to ensure that the noise in the samples is uncorrelated. Allowing an order of magnitude leeway, we set a lower bound of one millisecond, which corresponds to a spatial interval

$$\delta x = v \delta t,$$

where v is the speed of the probe antenna. Typically $v = 0.30 \text{ m/s}$, so $\delta x = .0003 \text{ meter}$.

At 10 GHz, $\lambda/2 = .015 \text{ meter}$, so this δx represents oversampling the data by a factor of

$$\frac{\lambda/2}{\delta x} = \frac{.015 \text{ m}}{.0003 \text{ m}} = 50,$$

which more than meets the oversampling goal mentioned above. The bandwidth of the receiver is large enough to allow much oversampling without compromising the noise characteristics of the sampled data.

Conclusions to be drawn are: (1) oversampling can be performed without reducing the RX probe scan speed, and (2) the measured noise will be uncorrelated from sample to sample. Note that the computer system is idle during the time required to return the RX platform for the next scan, so the filtering adds no time penalty.

H. PHASE WRAP DETECTION

The phase wrap problem is difficult to observe in standard gain and phase plots (Figures III-1 and III-2). The incorrect measurement occurs when the phase is changing

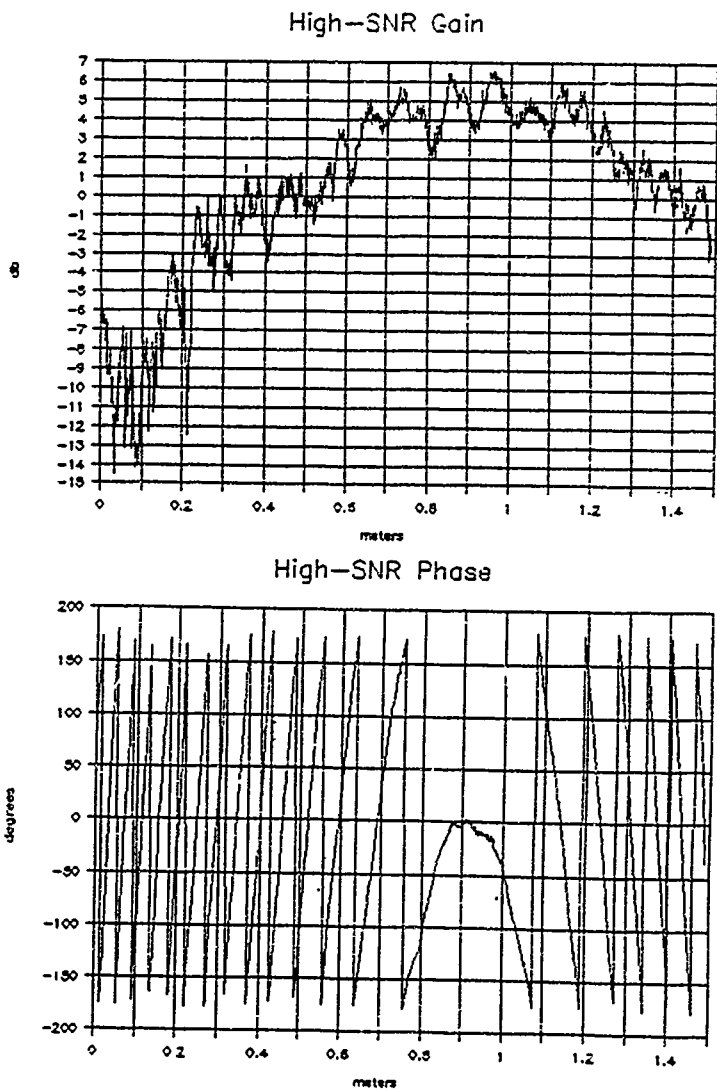
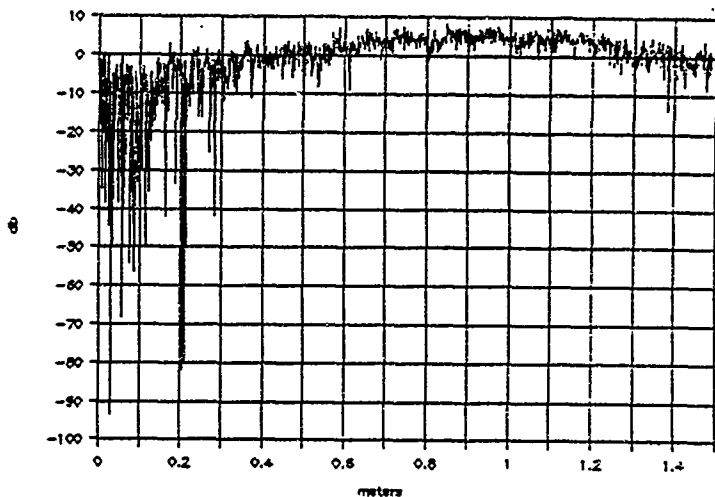


Figure III-1. Gain and Phase (High SNR)

Low-SNR Gain



Low-SNR Phase

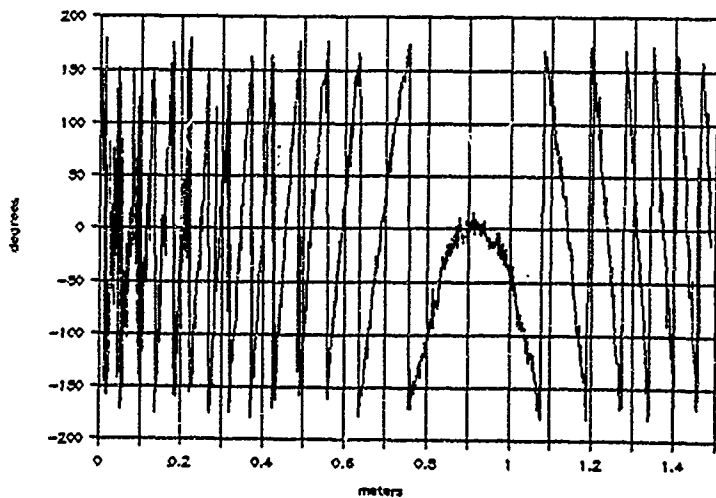


Figure III-2. Gain and Phase (Low SNR)

from +180 to -180 degrees (or vice versa), and the value measured is somewhere between 180 and -180, so that it appears approximately in the proper place on the plot and is easily overlooked.

The invalid sample often shows up clearly as a "spike" in plots of the real and imaginary components (Figures III-3 and III-4). The real and imaginary signal components are computed as

$$R(A, \varphi) = A \cos \varphi$$

$$I(A, \varphi) = A \sin \varphi$$

so

$$R(A, \pm 180) = -A$$

$$I(A, \pm 180) = 0.$$

On plots of real and imaginary components, one looks for phase errors when both (1) R is far from zero and "spikes" towards zero, and (2) I is about zero. Visual inspection of the figures illustrates this. If the gain A is small, the spike is hard to detect but will have minor effect upon the analysis of the raw data, since the first step in the analysis is a Fourier transform, which is basically a gain-weighted and phase-weighted averaging process.

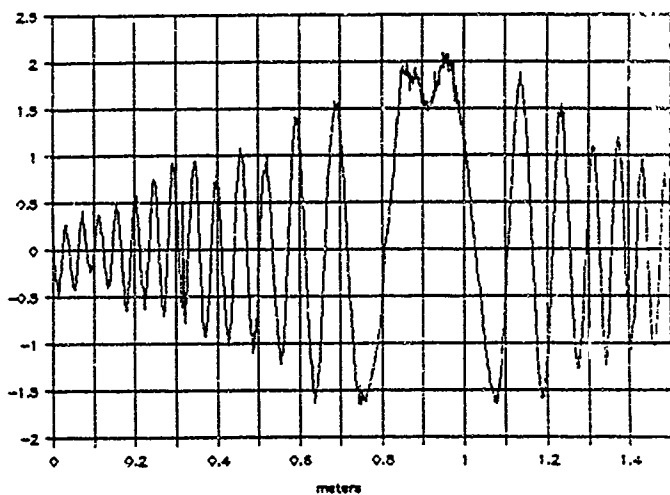
The difference between the high-SNR real component and the low-SNR real component is shown in Figure III-5. The phase error spikes are clearly visible.

One of several possible methods for locating phase errors of this type is by inspecting the derivative of the real (or imaginary) component with respect to the spatial coordinate. If $s(i)$ represents either the real or the imaginary component, then define the derivative process

$$s'(i) = s(i+1) - s(i)$$

which is a one-sided estimator of the derivative of $s(i)$. A spike in the process $s(i)$ appears as a double-sided spike in $s'(i)$ [cf. the engineering "derivative" of the continuous-time Dirac delta function].

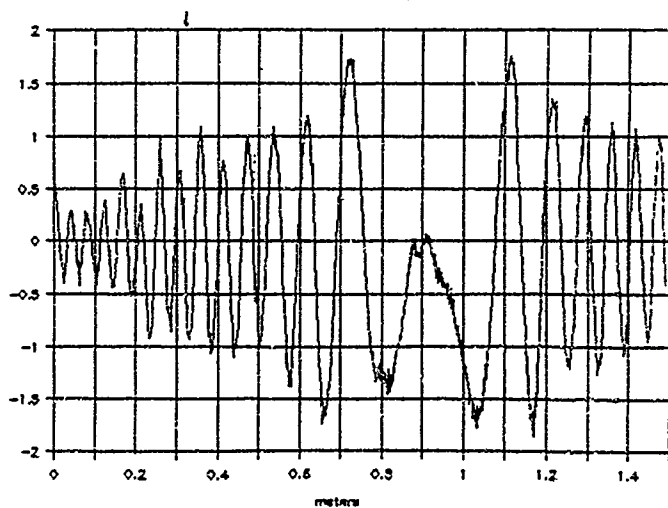
File: HIGHSNRR.DAT



Real

(High S/N)

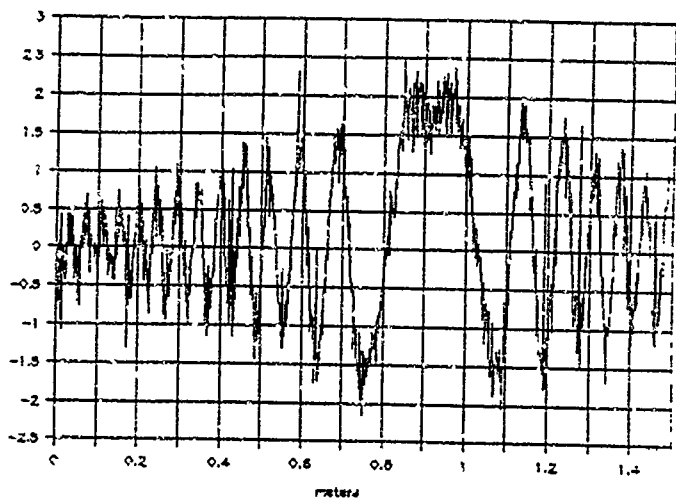
File: HIGHSNRI.DAT



Imaginary

Figure III-3. Real and Imaginary Parts (High SNR)

File: LOWSNRR.DAT



(Low S/N)

File: LOWSNRI.DAT

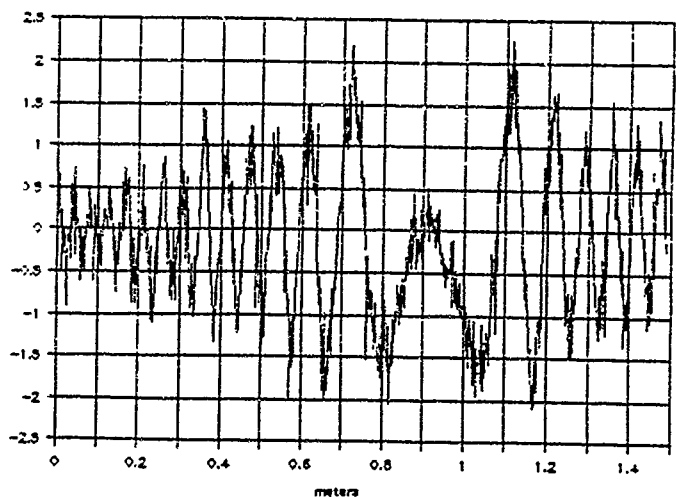


Figure III-4. Real and Imaginary Parts (Low SNR)

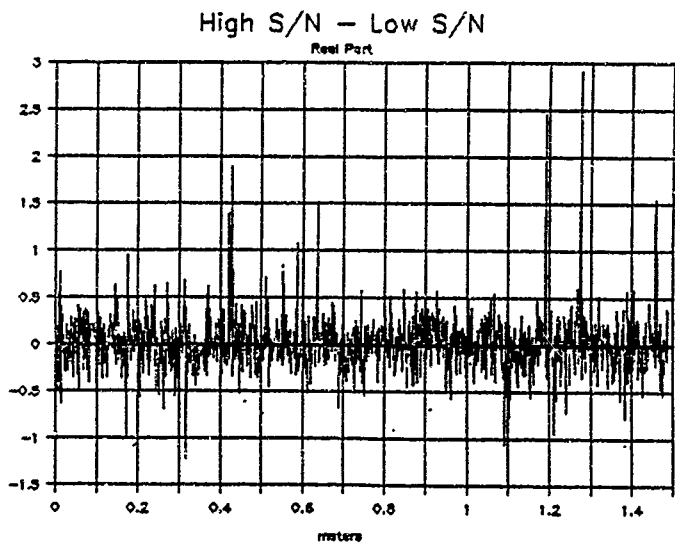


Figure III-5. Difference Between Real Parts
(High SNR versus Low SNR)

A threshold value for the minimum double-spike amplitude that should be classified as a phase error can be derived from Tchebysheff's Inequality [14] which relates the deviation $|X-\mu|$ of a process X to the variance σ of the process by the inequality

$$P\{|X-\mu| \geq n\sigma\} \leq \frac{1}{n^2}$$

irrespective of the form of the probability density function of X .

Identify X with the derivative process $s'(i)$, so

$$\begin{aligned}\mu &= E\{s'\} \\ &\approx \frac{1}{N} \sum_{n=1}^N s'(i),\end{aligned}$$

and

$$\begin{aligned}\sigma &= E\{(s' - \mu)^2\} \\ &= \left[\frac{1}{N} \sum_{n=1}^N (s'(i) - \mu)^2 \right]^{\frac{1}{2}}.\end{aligned}$$

For $n=3$, say, the inequality predicts that the probability that $|s'(i)-\mu|$ will exceed 3σ is less than $3^{-2}=0.11\bar{1}$.

The spike detection algorithm is constructed as follows. Compute the derivative sequence $s'(i)$. Compute the mean and variance of $s'(i)$ and normalize $s'(i)$ to zero mean and unit variance by the transformation

$$\hat{s}'(i) = \frac{s'(i) - \mu}{\sigma}.$$

Choose " n " to ensure a reasonably low rate of false detections, and perform the test $|\hat{s}'(i)| > n$ to locate invalid phase values in $s(i)$. The test is performed independently on the real and imaginary components of $s(i)$, and the combined results are used to select the suspect values of $s(i)$ for which interpolation is needed.

I. SPATIAL FILTERING

Since the noisy signal is oversampled by a factor of ten above the Nyquist rate, a low-pass digital filter can be applied to the measurements to improve SNR. Averaging

groups of ten adjacent samples is a simple approach to the filtering but distorts the higher spatial frequency components of the desired signal and has suboptimal noise suppression characteristics.

A linear-phase filter is required to avoid spatial phase distortion of the measured signal. A finite impulse response filter in the spatial domain with cutoff at normalized frequency $\nu_{\text{cutoff}} = \frac{f_{\text{cutoff}}}{f_{\text{Nyquist}}}$ can be constructed as follows [15].

We want a FIR filter of the form

$$H(z) = \sum_{i=0}^{m-1} a_i z^{-i}, \text{ where}$$

$m \equiv$ number of coefficients (odd integer), and

$a_i \equiv$ filter coefficients (real).

To ensure linear phase, we define the filter coefficients symmetrically as

$$c_i, i=0, 1, 2, \dots, q,$$

where

$$q \equiv (m-1)/2,$$

$$c_{-i} \equiv c_i.$$

The ideal low-pass filter has transfer function of the form

$$H_d(\nu) = \begin{cases} 1 & \text{if } \nu < \nu_{\text{cutoff}} \\ 0 & \text{if } \nu \geq \nu_{\text{cutoff}} \end{cases}.$$

Taking a discrete Fourier transform to the spatial domain, the filter coefficients are

$$c_i = \frac{\sin(i \pi \nu_{\text{cutoff}})}{i \pi}, i=0, 1, \dots, q.$$

Gain and phase response plots (not shown) verify that this is a linear phase low-pass filter with cutoff near $\nu=0.2$, but sidelobe levels are unacceptably high. Sidelobes are greatly reduced by using the smoothing window

$$w_H(i) = \begin{cases} 0.54 + 0.46 \cos(i\pi/q) \\ 0 \text{ otherwise} \end{cases},$$

so that

$$c_1 \equiv c_1' \cdot w_H(i).$$

Sidelobe levels of the filter composed of the c_1 (Figure III-6) are about 50 db down. At $f=1/\lambda$, the highest spatial frequency that the plane wave spectrum can contain outside the reactive near-field region, the corresponding normalized frequency is $\nu=0.1$, and the filter's gain is down by a factor of 0.92 (about -0.7 db). This level of attenuation will have negligible effect upon the near-field data analysis.

J. POWER SPECTRUM ANALYSIS

Autocorrelation (ACF) and power spectral density (PSD) of the real and imaginary components of the two scans are shown in Figures III-7 through III-10. The smoothing window bandwidth is $0.013f_{\text{Nyquist}}$. No differencing of the signals was performed, although slightly better PSDs might be obtained. Note that the PSDs are down by 20 to 30 db at the $1/\lambda$ frequency. The noise floor is down 35 db (high-SNR signal) and 20 db (low-SNR signal). One may conclude that the measured signals are indeed bandlimited to $1/\lambda$.

The composite plots in Figures III-11 through III-14 illustrate the effect of the spike detection, interpolation, and spatial filtering algorithms. The data traces in the figures, from top to bottom, are

- (1) raw data (real or imaginary),
- (2) normalized derivative $\hat{s}'(n)$,
- (3) combined "phase error" flags from real and imaginary components
using Tchebycheff's Inequality with $n=3$,
- (4) signal after phase errors are replaced by interpolated values,
- (5) final, filtered signal.

The scales of traces 1, 4, and 5 are identical, while 2 is shown at 0.25 sensitivity. Each scan (comprising about 1.5 meters) contains 1000 gain-phase sample pairs. For the

high S/N scan, 0.3 % of the phase samples were found invalid; 2.2 % of the low S/N scan values were invalid.

PSDs of the filtered signals are shown in Figures III-15 and III-16. Note that the phase error correction and filtering have lowered the noise floor by ten to fifteen db.

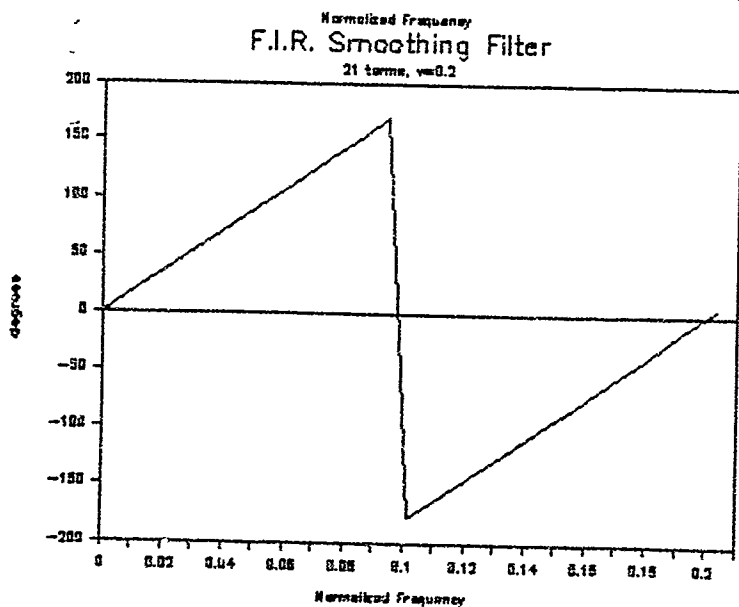
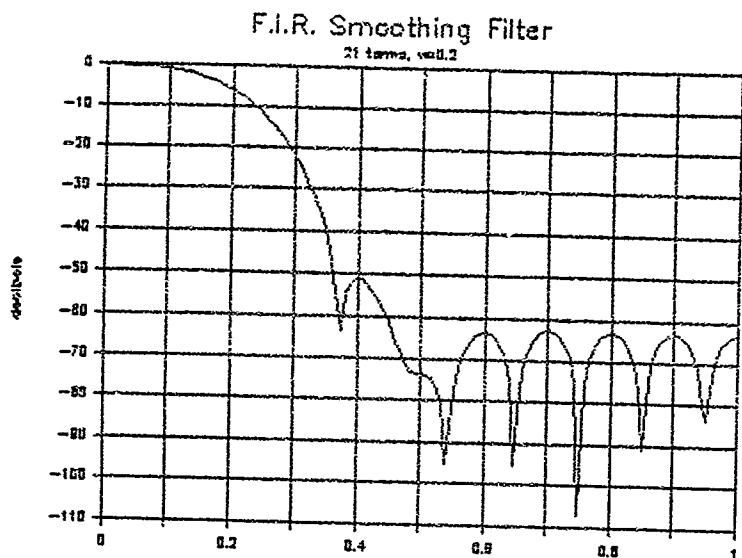
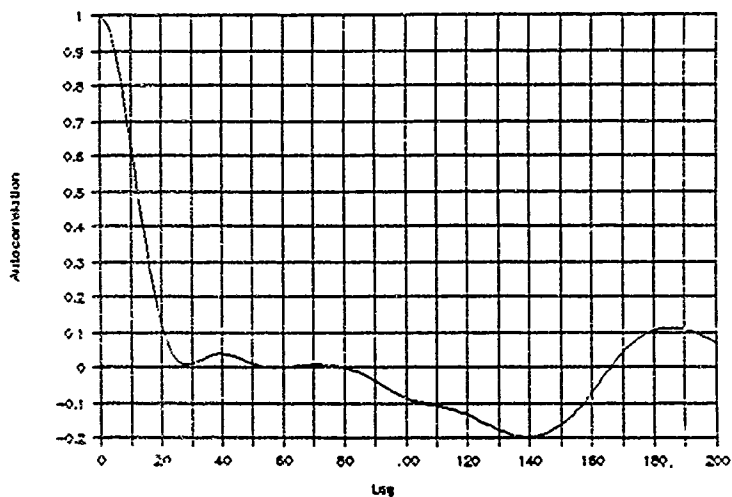


Figure III-6. Smoothing Filter Characteristics

Input file: HIGHSNRR.DAT



Input file: HIGHSNRR.DAT

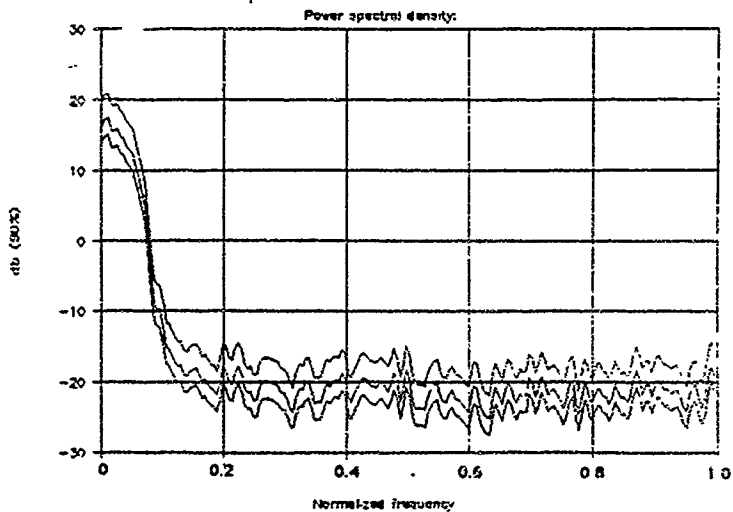
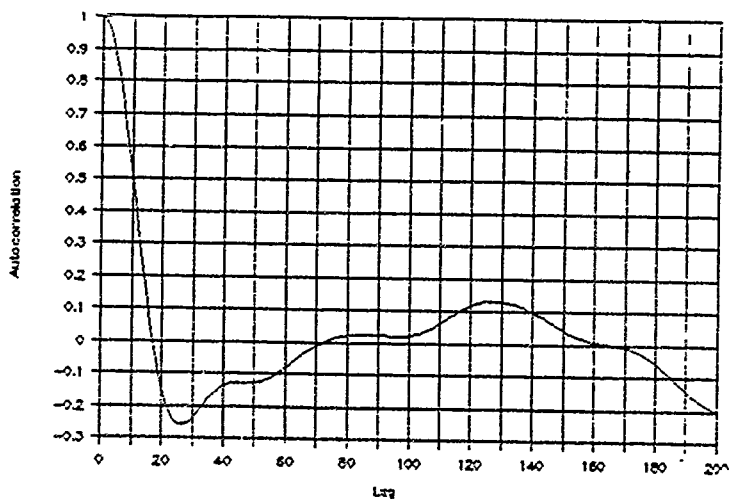


Figure III-7. Autocorrelation and PSD of Real Part (High SNR)

Input file: HIGHSNRI.DAT



Input file: HIGHSNRI.DAT

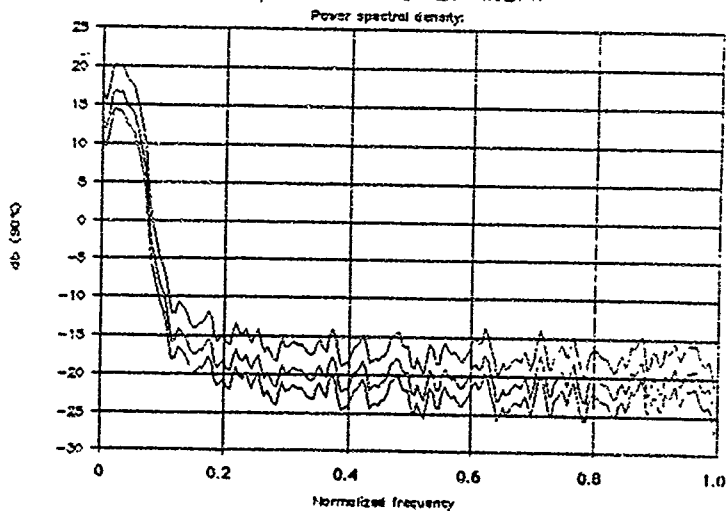
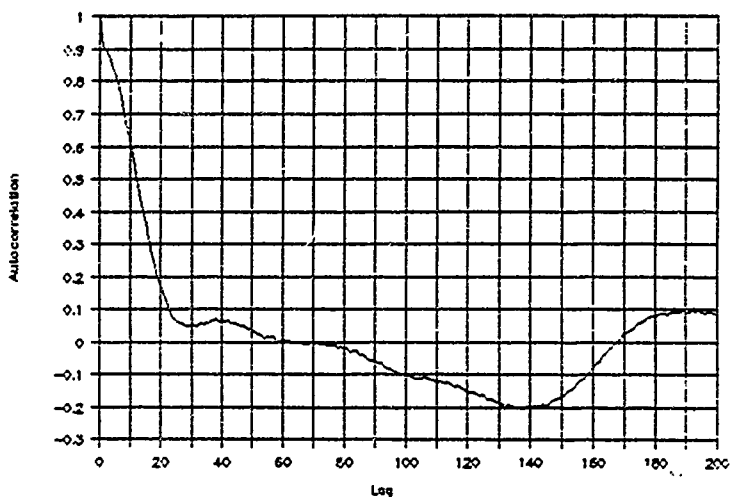


Figure III-8. Autocorrelation and PSD of Imaginary Part (High SNR)

Input file: LOWSNRR.DAT



Input file: LOWSNRR.DAT

Power spectral density

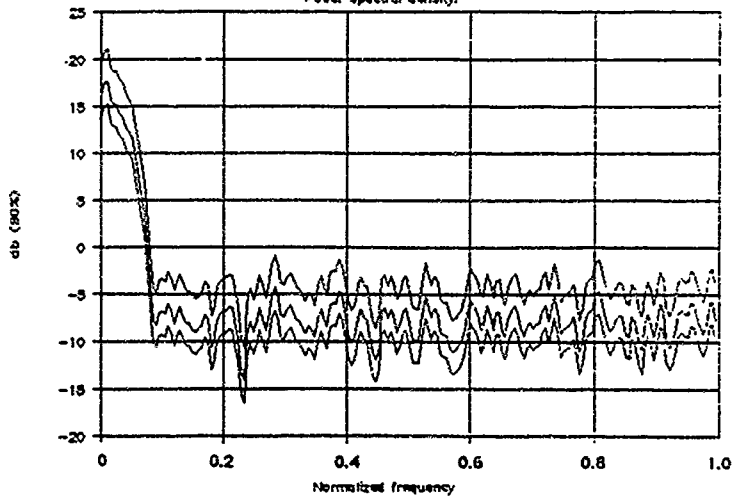
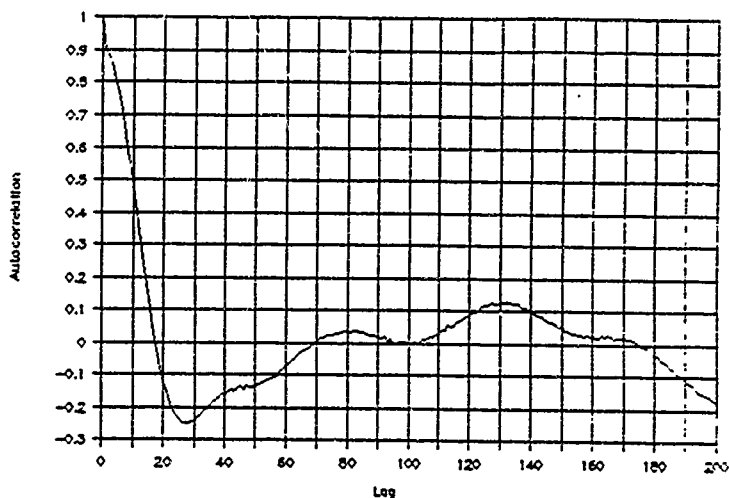


Figure III-9. Autocorrelation and PSD
of Real Part (Low SNR)

Input file: LOWSNRI.DAT



Input file: LOWSNRI.DAT

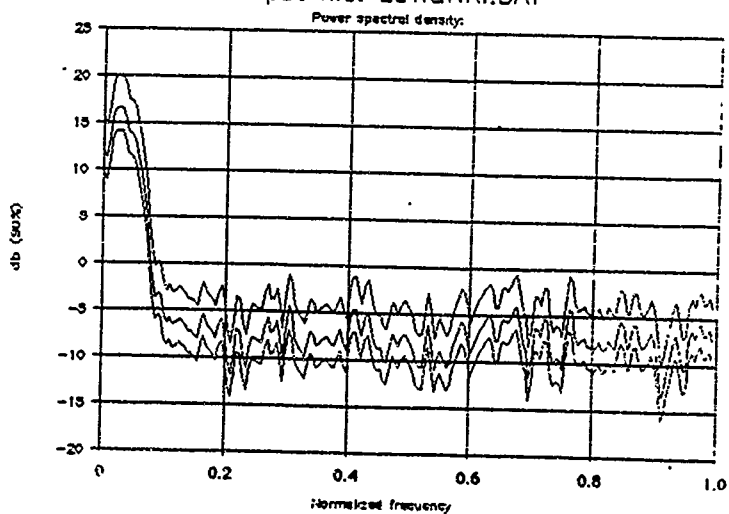
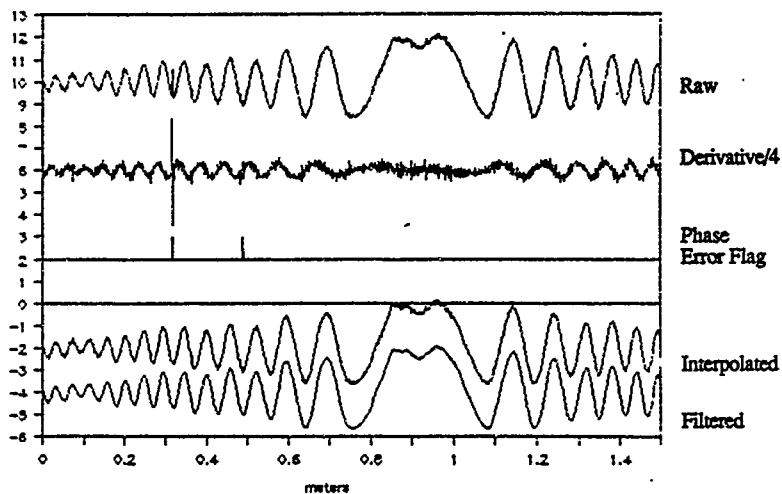


Figure III-10. Autocorrelation and PSD
of Imaginary Part (Low SNR)

High S/N Real



High S/N Real

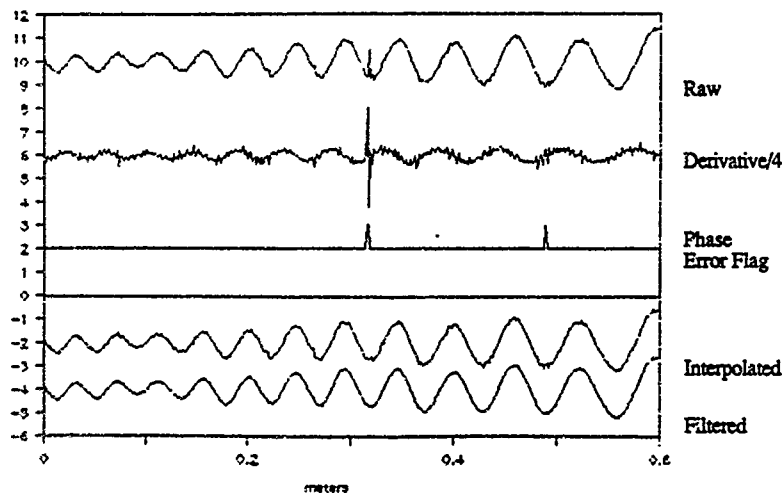


Figure III-11. Signal Cleanup of Real Part (High SNR)

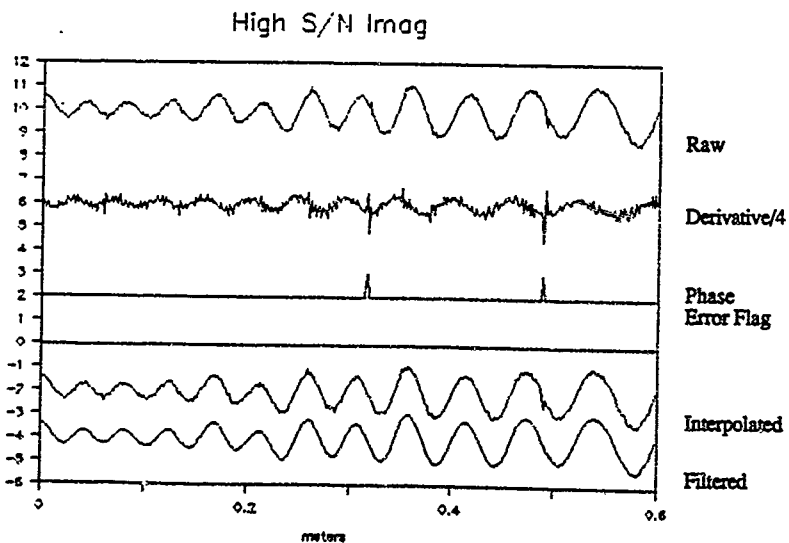
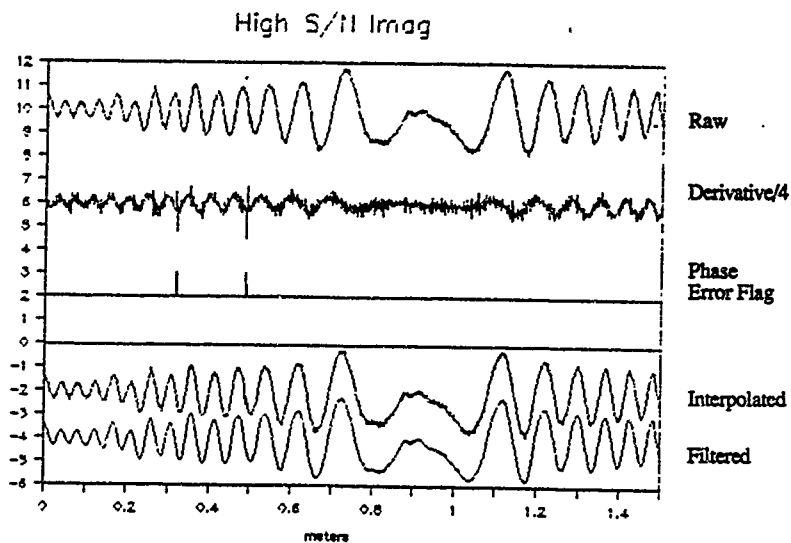


Figure III-12. Signal Cleanup of Imaginary Part (High SNR)

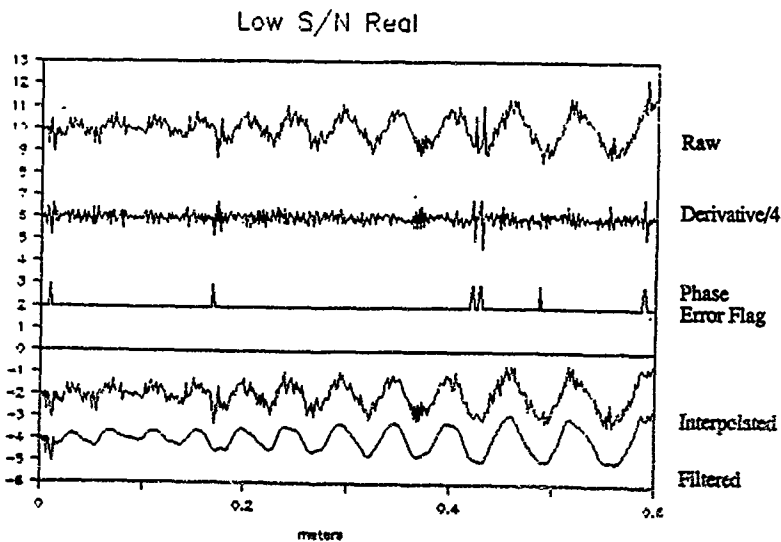
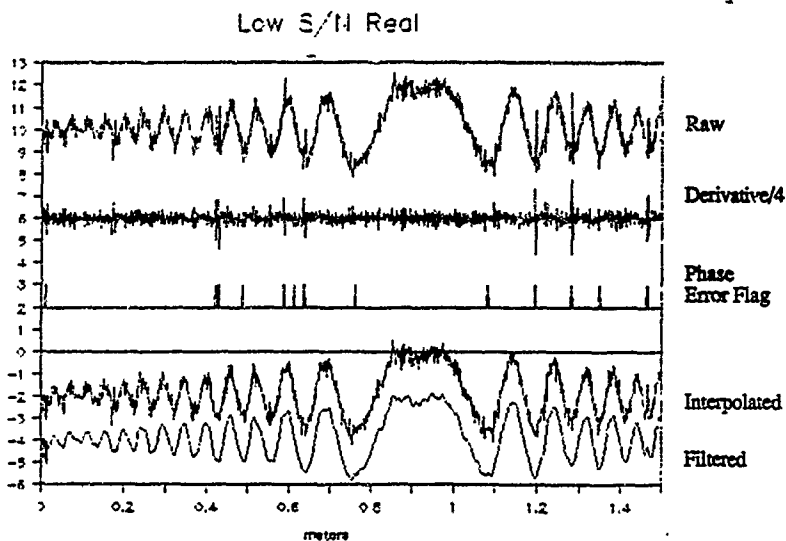


Figure III-13. Signal Cleanup of Real Part (Low SNR)

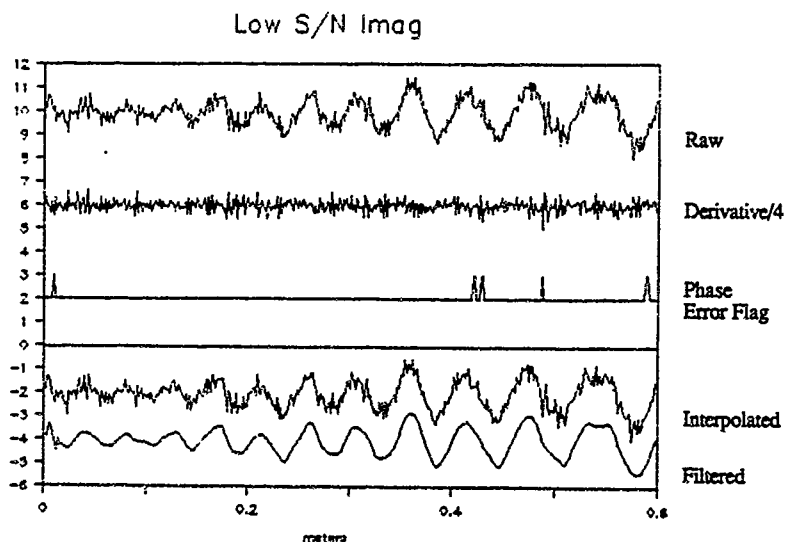
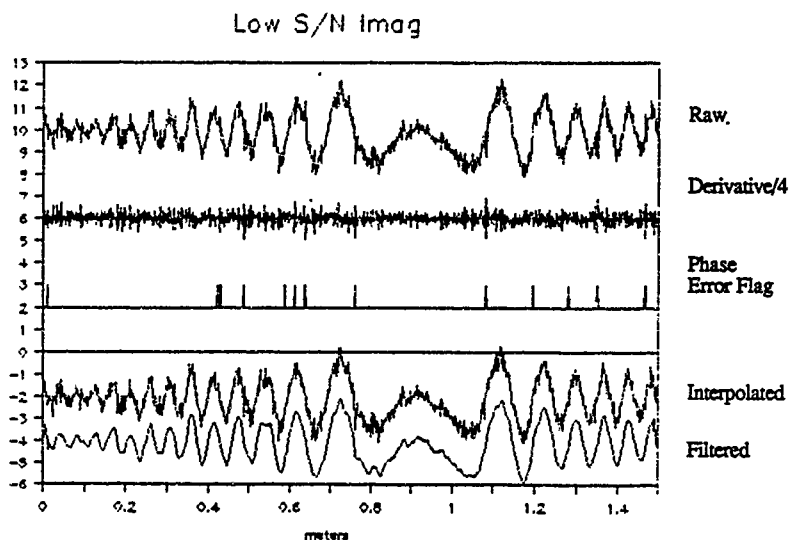


Figure III-14. Signal Cleanup of Imaginary Part (Low SNR)

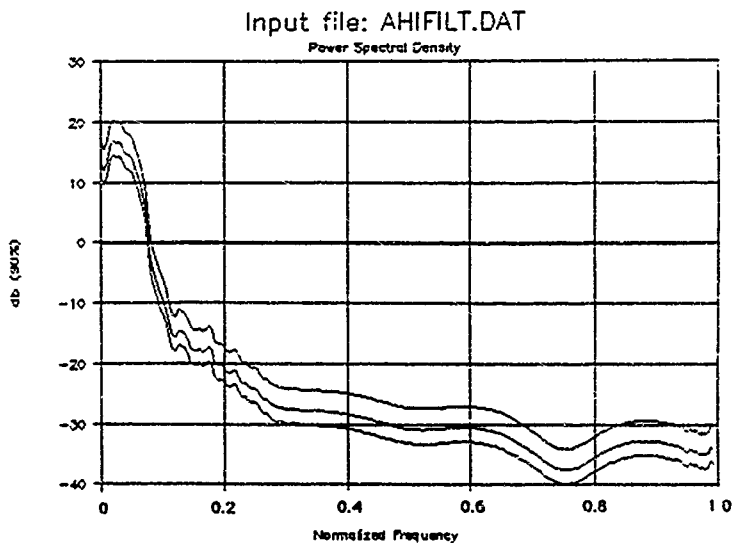
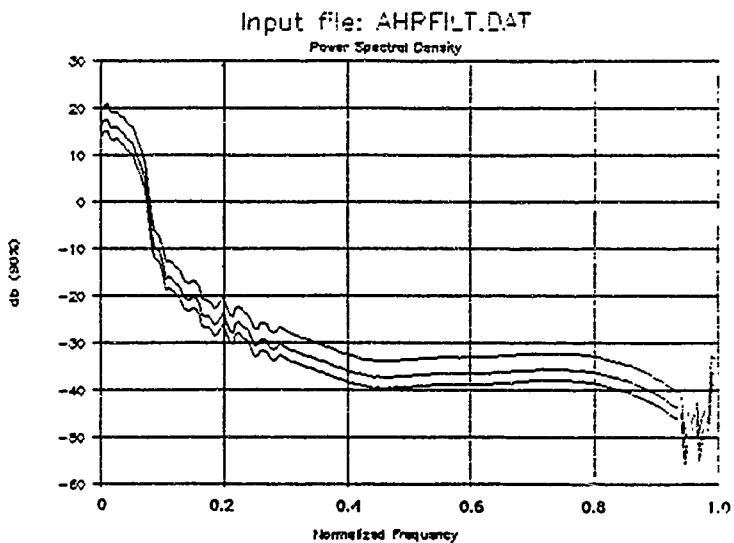


Figure III-15. PSD of Real and Imaginary Parts
After Cleanup (High SNR)

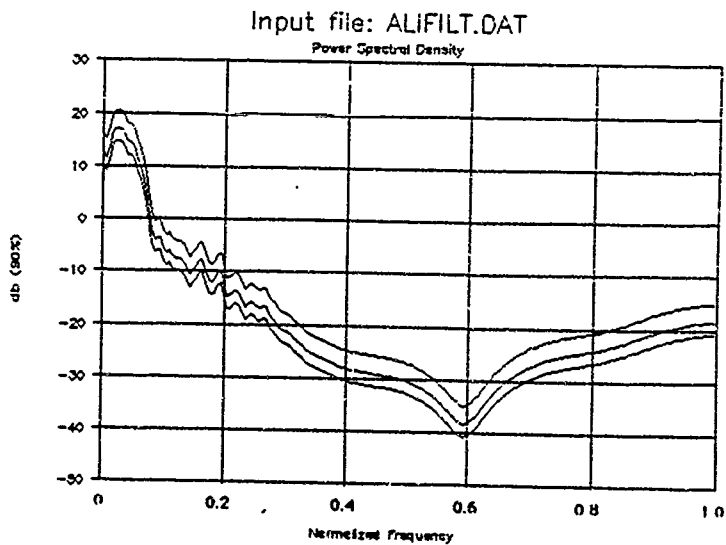
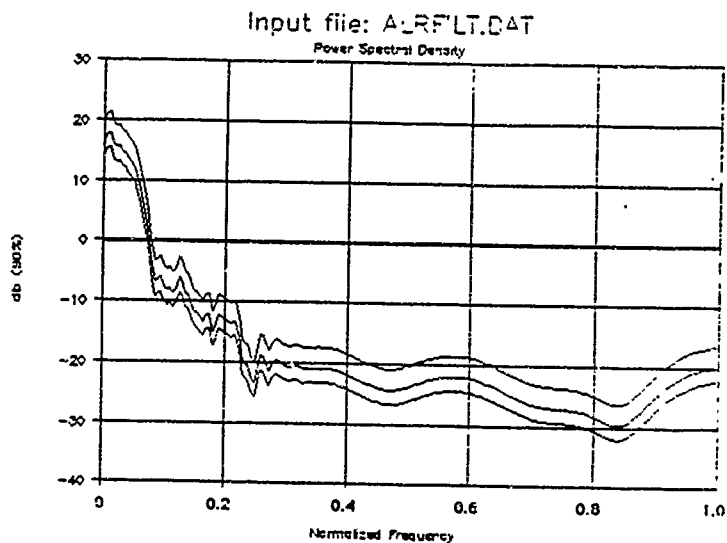


Figure III-16. PSD of Real and Imaginary Parts
After Cleanup (Low SNR)

CHAPTER IV

DESIGN AND CONSTRUCTION OF SCANNER

A. SCAN TABLE

The scan table (Figure IV-1) has two movable carriages, each with one movable platform. The two platforms are referred to as the TX and RX platforms. Prior to scanning, the TX and RX platforms start from known initial positions defined by reference marks on the scan table. The initial positions for the TX and RX platforms are near the lower-left and upper-left corners of the available scan area, respectively, as viewed from the operator's position. The stepper motor control software compensates for the offset between the initial TX and RX positions, so that coordinates for TX probe, RX probe, and test object are expressed in terms of the same coordinate system.

Optoelectronic sensors are located at the home positions of the platforms. When the scan table is initialized, and at intervals during scanning, the software moves the platforms to the home positions and verifies that the stepper motors are still calibrated (i.e., no steps have been lost). If the software finds that steps were lost, the previous segment of data is automatically reacquired.

When near-field antenna measurements are performed, the antenna under test (AUT) is mounted above the table pointing down, and the receiving probe antenna is mounted on the RX platform. The TX platform is not used in this mode.

When near-field bistatic RCS measurements are performed, the object under test (OUT) is mounted above the scanning table, and the transmit and receive probe antennas are mounted on the TX and RX platforms, respectively.

B. PROBE ANTENNAS

The probe antennas are identical equal-length open-ended sections of X-band waveguide or pyramidal horn antennas. Each probe is held in a mounting bracket that is bolted to a single mounting hole on its platform. The TX and RX probes are always on the platforms, as indicated in Figure IV-1.

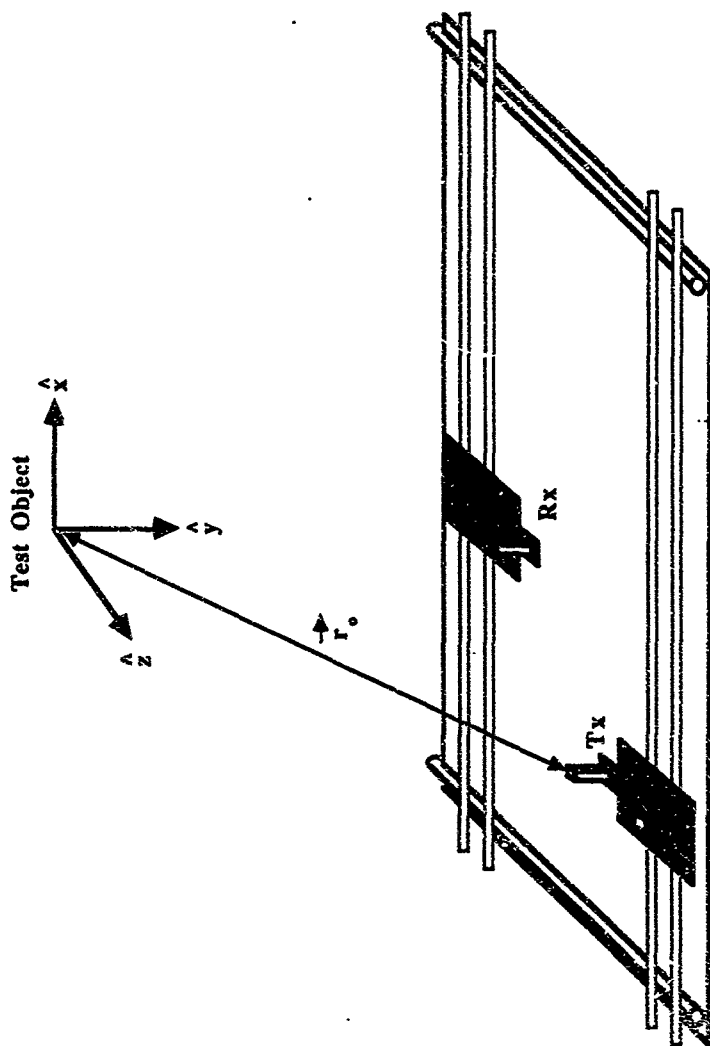


Figure IV-1. Scan Table Platforms

Both platforms are used when performing bistatic RCS measurements; only the RX platform is used when performing antenna measurements.

C. SCAN PATTERNS

The TX and RX probe antennas move through predetermined scan patterns when measurements are being made. The scan patterns are shown pictorially in Figure IV-2 and algorithmically in Figures IV-3 and IV-4. During scanning the probe antennas move along the x-axis while holding y constant.

The data analysis computer programs impose some limitations on the scan patterns. If near-field antenna measurements are to be performed, the TX scan pattern is (effectively) a 1-by-1 scan, and the RX scan pattern must be square with an even number of points on each side. If near-field bistatic RCS measurements are to be performed, the TX and RX scan patterns must be square and have an even number of points on each side. The x- and y-sampling intervals for both the RX and TX patterns must be identical.

D. MEASUREMENT CONFIGURATION

The equipment configuration for performing near-field measurements is shown in Figure IV-5. The synthesized RF signal is taken from the output port of the Hewlett-Packard 8408B Microwave Network Analyzer to a 20-watt TWT amplifier, and then to either the antenna under test or the TX probe antenna via a length L_1 of semi-rigid RG .402/U coaxial cable. A length L_2 of RG .402/U cable carries the received signal from the RX probe to a preamplifier and then to the input port of the 8408B. There is additional amplification/attenuation in the test channel gain G_{tc} setting in the 8408B, which may be adjusted differently on different measurement runs. L_1 and L_2 are typically both 25 feet long.

Gain and phase are calculated continuously by the 8408B and are captured by the dual-channel A/D converter for the IBM PC. The analog processing circuits in the 8408B can operate at either 100 hz or 10 khz bandwidth. The 10 khz bandwidth is used to avoid smearing the measured data during fast scanning.

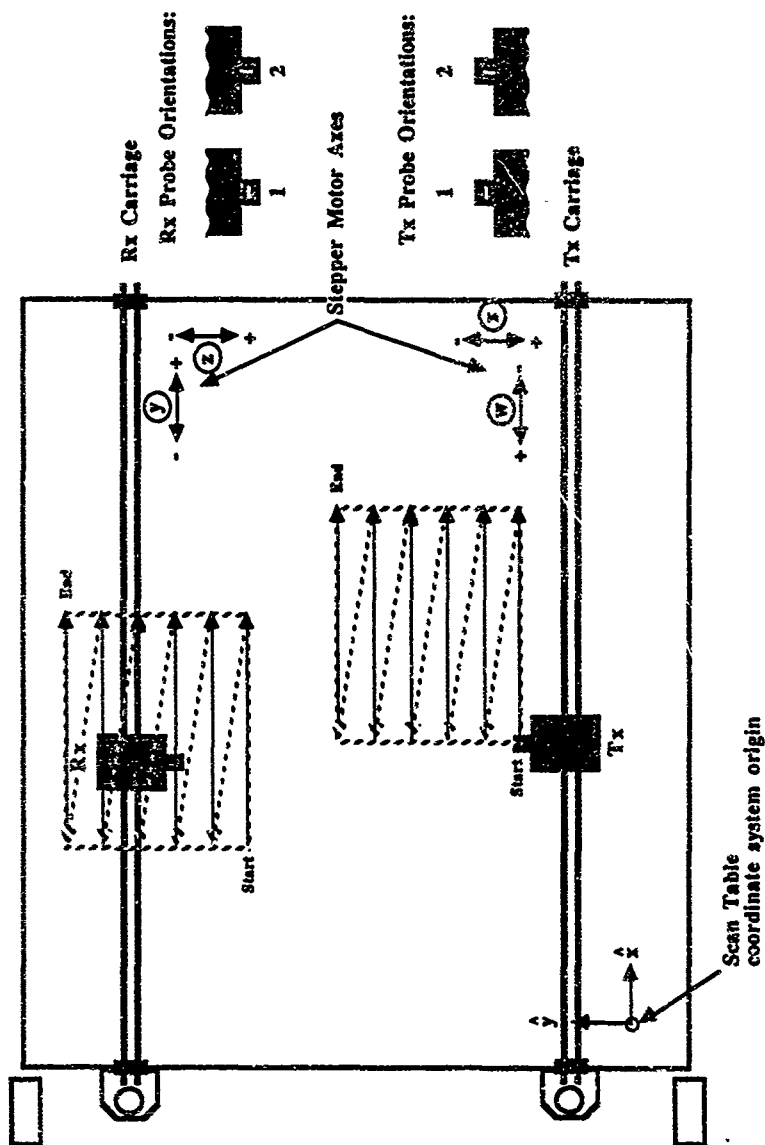


Figure IV-2. Scan Patterns and Probe Orientations

```

C      Pseudo-code for Antenna Measurement Scanning
C
C      NXRX,NYRX = number of points along x,y for RX probe
C      IXX,IYRX = loop indices for RX scanning
C      XRXORG,YRXORG = lower left corner of RX scan pattern
C      XRX,YRX = current coordinates of RX probe
C      IRXO = RX probe orientation
C      DELTXY = sample interval (meters)
C
      DO 20 IRXO=1,2
      DO 10 IYRX=1,NYRX
      DO 10 IXX=1,NXRX
      XRX=XRXORG+(IXX-1)*DELTXY
      YRX=YRXORG+(IYRX-1)*DELTXY
      CALL MOVE(XRX,YRX)
      CALL MEASURE(GAIN,PHASE)
      CALL WRITE(GAIN,PHASE)
10     CONTINUE
      PAUSE 'Change probe orientation now.'
20     CONTINUE
      STOP 'Done.'
      END

```

Figure IV-3. FORTRAN Code for Antenna Measurement Scan Pattern

```

C      Pseudo-code for Bistatic Measurement Scanning
C
C      NXTX, NYTX = number of points along x,y for TX probe
C      IXTX, IYTX = loop indices for TX scanning
C      XTXORG, YTXORG = lower left corner of TX scan pattern
C      XYX, YTX = current coordinates of TX probe
C      ITXO = TX probe orientation
C      NXRX, NYRX = number of points along x,y for RX probe
C      IXX, IYRX = loop indices for RX scanning
C      XRXORG, YRXORG = lower left corner of RX scan pattern
C      XRX, YRX = current coordinates of RX probe
C      IRXO = RX probe orientation
C      DELTXY = sample interval (meters)
C
      DO 30 ITXO=1,2
      DO 30 IRXO=1,2
      DO 20 IYTX=1, NYTX
      DO 20 IXTX=1, NXTX
      XTX=XTXORG+(IXTX-1)*DELTXY
      YTX=YTXORG+(IYTX-1)*DELTXY
      CALL TXMOVE(XTX, YTX)
      DO 10 IYRX=1, NYRX
      DO 10 IXX=1, NXRX
      XRX=XRXORG+(IXRX-1)*DELTXY
      YRX=YRXORG+(IYTX-1)*DELTXY
      CALL MOVE(XRX, YRX)
      CALL MEASURE(GAIN, PHASE)
      CALL WRITE(GAIN, PHASE)
10    CONTINUE
20    CONTINUE
      PAUSE 'Change probe orientations now.'
30    CONTINUE
      STOP 'Done.'
      END

```

Figure IV-4. FORTRAN Code for Bistatic Scan Pattern

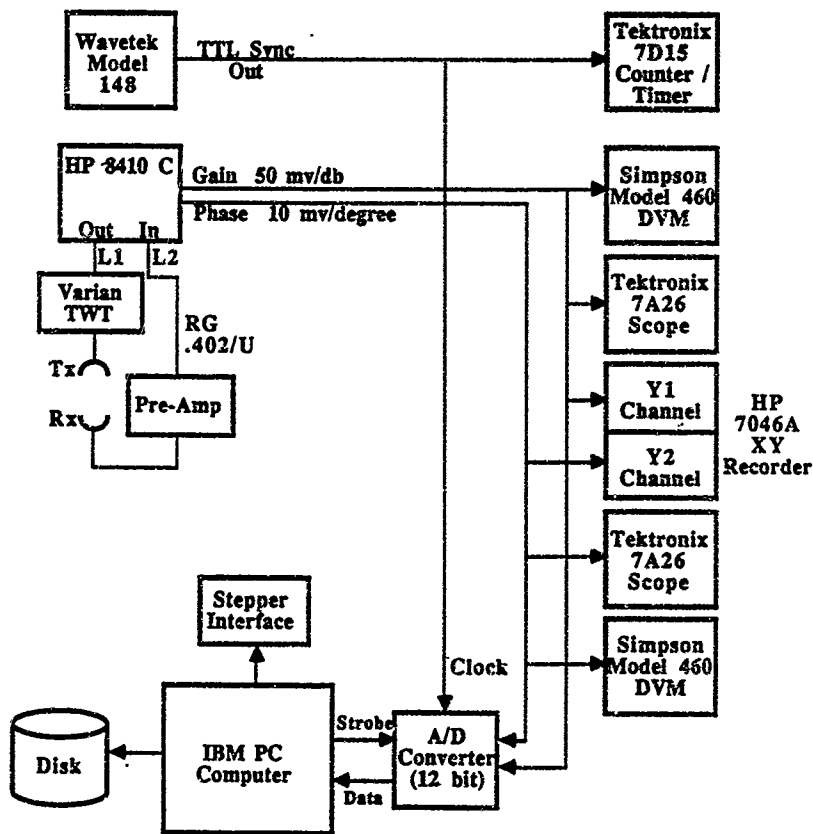


Figure IV-5. Equipment Configuration

E. DATA ACQUISITION SYSTEM

Data acquisition is controlled by a computer program that runs on the IBM PC. The program controls the scanning table motors and A/D converter and stores the measured data to disk.

The conversion time of the 12-bit A/D converter is typically 25 μ s. Gain and phase are sampled simultaneously by dual sample/hold amplifiers and then digitized in succession by the A/D converter. The measurements are the gain (V_g) and phase (V_ϕ) voltages from the network analyzer. The actual gain and phase are computed as $G = V_g \cdot f_{\text{gain}}$ and $\phi = V_\phi \cdot f_\phi$, where f_{gain} is a gain calibration factor (20.0 db/volt) and f_ϕ is a phase calibration factor (100.0 degrees/volt) for the 8408B analyzer. The gain and phase are combined into a complex number and stored in a disk file.

CHAPTER V

COMPARISON OF MEASUREMENTS WITH SOLUTIONS

A. INTRODUCTION

The far-field RCS that is calculated via near-field RCS measurements may be checked by comparing it to the far-field RCS predicted by electromagnetic theory. The conducting sphere and disk are convenient objects for this comparison, since an analytic solution exists for the sphere and a physical optics solution may be applied to the disk. Equations for scattering from sphere and disk may be found in Appendices C and D, respectively. In this chapter we present a quantitative comparison of the far-field RCS obtained via near-field measurements with the calculated far-field RCS of the conducting sphere.

Although full bistatic scattering measurements were made on the sphere and the disk, funding and time limitations precluded our performing the data reduction and analysis of that data. The results presented here represent scattering from the sphere only.

These near-field measurements were made at 10 Ghz using the experimental setup described in Chapter III. The target is a precision 6 inch diameter aluminum sphere mounted above the scanning table. The measurements were made on a 64 by 64 grid of points with the transmit antenna stationary and directly under the target, so that the target illumination was essentially

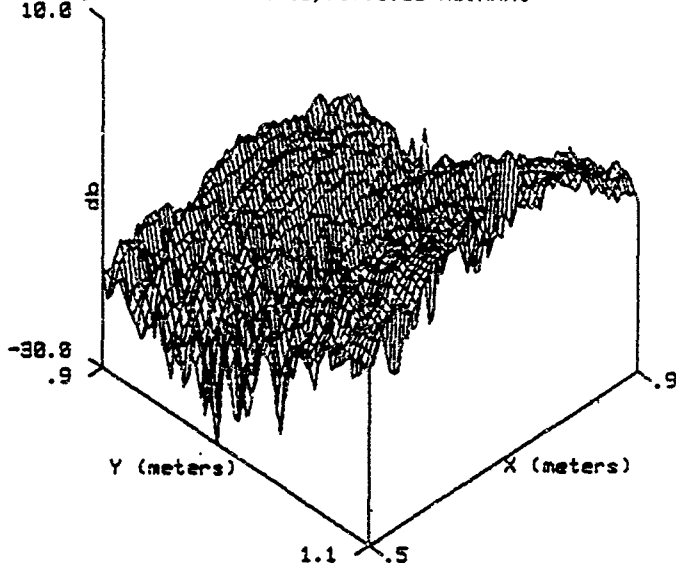
$$\hat{E} = |E| \hat{e}_y$$

B. COHERENT BACKGROUND SUBTRACTION

In Figure V-1 may be seen the magnitude of the co-polarization component of the raw data measured by the receiving antenna. The target sphere, located at (x,y) coordinate (1.02,1.02) meters, is above the lower right edge of the plot, corresponding to the peak amplitude of the raw signal.

Figure V-2 shows a background plot with all parameters identical to the previous plot with the exception of the target sphere, which was removed from the test volume.

Data set #1 (db)
 [5/02/88,19:50:08/ 5/02/88,16:51:30/M3.RAW]
 10.8

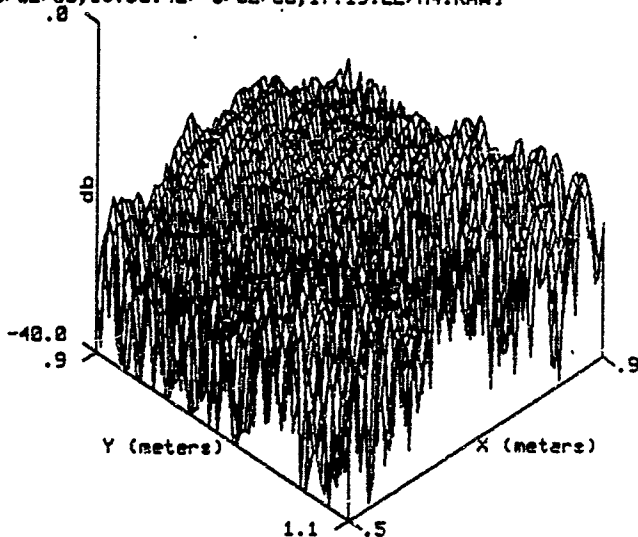


Data set #1 (db)
 [5/02/88,19:50:08/ 5/02/88,16:51:30/M3.RAW]

[5/02/88,19:50:08/ 5/02/88,16:51:30/M3.RAW]
 INFILE = M3.RAW
 OUTFILE = M3.RAW 5/02/88 16:51:30
 OBJECT = sphere, horns, 90 barrier
 RX pattern starts @ 102.300, 102.600 cm.
 RX pattern starts @ 55.030, 119.000 cm.
 Object is at 102.300, 102.600, 110.500 cm.
 Delta-x,y = 1.50 cm.
 Waveguide a,b = 2.28 cm.
 Frequency = 10.000 GHz; 1.016 cm.
 RX pattern size: 1 by 1
 RX pattern size: 64 by 64
 RX orientations: 1,1 1,2 0,0 0,0
 For (1,1): -12.6 db @ 1x,1y= 37, 1, or 1.030, 1.150 m:
 For (1,2): -12.6 db @ 1x,1y= 37, 1, or 1.090, 1.220 m:

Figure V-1. Co-polarization Magnitude

Data set #1 (db)
[5/02/88,19:56:42/ 5/02/88,17:19:22/M4.RAW]



Data set #1 (db)
[5/02/88,19:56:42/ 5/02/88,17:19:22/M4.RAW]

[5/02/88,19:56:42/ 5/02/88,17:19:22/M4.RAW]s

```
INFILE = M4.RAW
OBJFILE = M4.RAW 5/02/88 17:19:22
OBJECT = no sphere, horns, no barrier
rx pattern starts at 102.300, 102.600 ca.
tx pattern starts at 135.030, 119.000 ca.
Object is at 102.300, 102.600, 110.300 ca.
Delta-x,y = 1.50 58z, 1.016 ca.
Waveguide a,b = 2.58z, 1.016 ca.
Frequency = 10.000 GHz
rx pattern size: 41 by 41
tx pattern size: 41 by 41
rx,tx orientations: 1 1 2 0.0 0.0
for (1,1): -1.1 db @ 10,1v= 0.0 0.0
for (1,2): -22.2 db @ 1x,1v= 42, 3; or 1:030, 1:190 a:
```

Figure V-2. Co-polarization Background Magnitude

Although there is no coherent background signature visible in the figure, the raw data are noticeably cleaner after this background scan is subtracted coherently from it (Figure V-3). The improvement in signal/noise ratio is even more apparent in Figures V-4 and V-5, which are contour plots of the imaginary component of the co-polarization before and after coherent background subtraction, respectively. Similar improvement occurs in the cross-polarization components.

Coherent background subtraction is performed for all data shown in the figures in the remainder of this section.

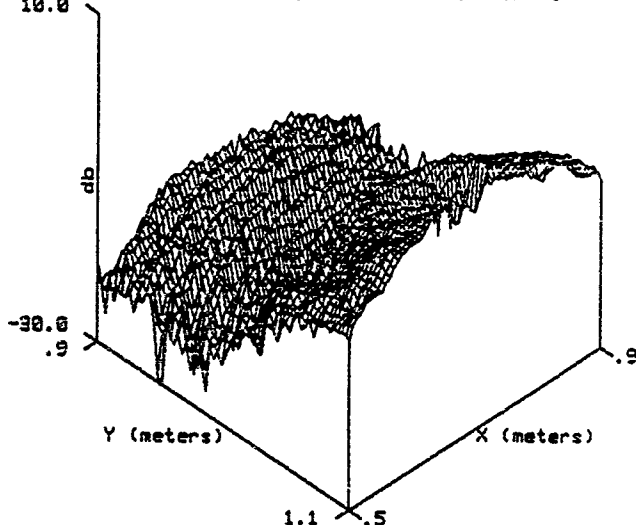
C. DATA TAPERING

The first step in the analysis of the raw data is a two-dimensional discrete Fourier transform (DFT). The signal processing aspects of the data analysis are illustrated by the effects of several tapering methods that were tried. Figure V-6 shows the magnitude of the DFT of the co-polarization signal with no tapering; this is equivalent to a rectangular ("boxcar") taper in the continuous domain. The direct scattering from the target shows up as the large peak in the figure, and probe-to-probe coupling appears at the upper left and lower right edges of the figure. The side-lobe level due to leakage from the main peak is about 30 db below the peak.

In Figure V-7 is shown the magnitude of the DFT of the co-polarization signal after a separable cosine taper of the form $\frac{1 + \cos(\xi)}{2}$ was applied to both the x-axis and the y-axis. Note that the sidelobe level is better than 40 db down and the probe-to-probe coupling peak is much more localized, although there is little fine structure discernible on the peaks.

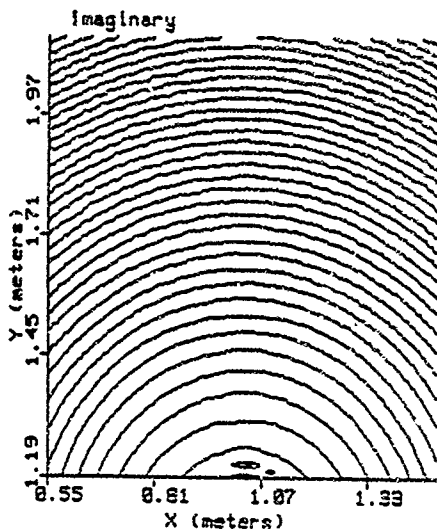
Figure V-8 shows the magnitude of the DFT of the co-polarization signal after a separable, partial-cosine taper was applied to both axes. This taper consists of a cosine taper spliced onto a boxcar-type taper, so that the middle half of the data are unaffected while the first and last quarters of the data set are tapered. The sidelobe suppression of this taper is generally poorer than that of the cosine, but for this data set is

Data set #1 (db)
 [5/03/88,15:20:25/ 5/02/88,16:51:30/MSREFM4.RAW]
 10.0



Data set #1 (db)
 [5/03/88,15:20:25/ 5/02/88,16:51:30/MSREFM4.RAW]
 [5/03/88,15:20:25/ 5/02/88,16:51:30/MSREFM4.RAW]
 INFIL = MSREFM4.RAW
 OLDFIL = MSREFM4.RAW
 QBJEC = sphere, horns, 90 barrier REF.
 RX pattern starts @ 102.300, 102.600 cm.
 TX pattern starts @ 33.050, 119.000 cm.
 Object is at 102.300, 102.600, 119.300 cm.
 Delta-x,y = 1.30 cm,
 Waveguide a,b = 2.528, 1.016 cm.
 Frequency = 10.000 GHz
 RX pattern size: 1 by 1
 TX pattern size: 4 by 4
 RX orientations: TX, 1.2 0.0 0.0
 For (1,1): -18.6 db @ TX, TY = 33, 1: or 1.030, 1.190 m.
 For (1,2): -18.6 db @ TX, TY = 33, 1: or 1.030, 1.190 m.

Figure V-3. Co-polarization After Background Subtraction

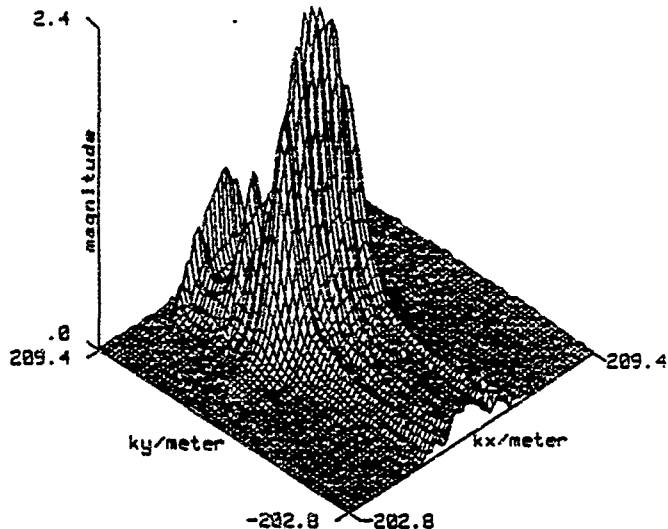


Measured Set #1 (imaginary part)
 [5/03/88,15:20:25/ 5/02/88,16:51:30/M3REFM4.RAW]

```
[ 5/03/88,15:20:25/ 5/02/88,16:51:30/M3REFM4.RAW ]
IN-FILE = M3REFM4.RAW
OBJ-FILE = M3.RAW 5/02/88 16:51:30
OBJECT = sphere, horns, 50 barrierREF.
RX pattern starts @ 10.000, 10.000 cm.
TX pattern starts @ 55.250, 119.000 cm.
Object is at 102.000, 102.600, 110.500 cm.
Delta-x,y = 1.50 cm.
Waveguide a,b = 2.00, 1.016 cm.
Frequency = 10.000 GHz.
TX pattern size: 1 by 1
RX pattern size: 64 by 64
TX, RX orientations: 0.0, 0.0, 0.0, 0.0
PR, RX orientations: 0.0, 0.0, 0.0, 0.0
PR (1:1) -18.6 dB @ RX, IV = TX; 1, or 1.030; 1:120 m.
```

Figure V-5. Co-polarization Imaginary Part After Background Subtraction

Magnitude of FFT of "b"
[5/03/88,13:20:35/ 5/02/88,16:51:30/M3REFM4.TXA]



Magnitude of FFT of "b"
[5/03/88,13:20:39/ 5/02/88,16:51:30/MOREFM4.TXA]

[illegible]

Figure V-6. Co-polarization DFT Without Taper

A 3D surface plot showing the magnitude of a function as a function of k_x and k_y . The vertical axis is labeled 'magnitude' and ranges from 0 to 0.7. The horizontal axes are labeled k_x/meter and k_y/meter . The k_x axis ranges from -202.8 to 202.8, and the k_y axis ranges from -209.4 to 209.4. The surface features a prominent, sharp peak at the center, reaching a magnitude of approximately 0.7. There are also smaller, broader peaks on the left and right sides of the central peak.

[illegible]

V-9

A 3D surface plot showing the magnitude of a function as a function of spatial frequencies k_x and k_y . The vertical axis is labeled 'magnitude' and ranges from 0 to 1.8. The horizontal axes are labeled ' k_x /meter' and ' k_y /meter'. The k_x axis ranges from -202.8 to 202.8, and the k_y axis ranges from -209.4 to 209.4. The surface features a prominent, sharp peak at the center, reaching a magnitude of approximately 1.8. The surface is rendered with a wireframe mesh.

[illegible]

Y-10

comparable to that produced by the cosine taper. Much more structure is visible on the peaks (a common characteristic of this type of taper).

A similar judgment may be made based on the calculated scattering matrix. Figures V-9 through V-11 show the magnitude of S_{θ} calculated using no taper, a cosine taper, and a partial cosine taper, respectively. The cosine taper has the lowest sidelobe levels, while the partial cosine taper has higher sidelobes but more detail in the transformed data. In general, the additional detail makes the partial cosine taper preferable to the cosine taper.

D. PROBE-PROBE COUPLING

Figures V-3 and V-8 illustrate the manner in which the measured data are transformed from a Cartesian coordinate system with units of meters (Figure V-3) to an angular spectrum with units of reciprocal meters (Figure V-8) in k -space. The directly coupled signal from the transmit probe to the receive probe appears in the angular spectrum as a broad peak with incident wavenumbers near the horizon (i.e., $|k_z| \approx 0$) in angular space.

This direct signal can be separated from the desired signal if the desired signal is not too close to the direct signal in k -space. Note that (Figure V-8) the probe-probe coupling appears as a broad peak at the top left edge of the plot and spills over (due to wraparound in the DFT) to the lower right edge. This broad peak is distinct from, and does not corrupt, the desired signal in these plots.

Under these conditions, the only detrimental effect of probe-probe coupling is that it increases the required dynamic range of the receiver.

E. REGION OF DEFINITION

The region of definition of the reconstructed RCS is limited by the size of the scan area relative to the apparent angular extent of the object as viewed from the center of the measurement scan. In general, the actual area of definition is relatively small when viewed in k -space. The reconstructed phase of S_{θ} shown in Figure V-12 is valid only over a small

A 3D surface plot showing the magnitude of a seismic event as a function of spatial coordinates k_x and k_y . The vertical axis is labeled 'magnitude' and ranges from 1276.5 to 1276.6. The horizontal axes are labeled ' k_x /degree' and ' k_y /degree', both ranging from -202.8 to 209.4. The surface is highly irregular and jagged, with a prominent peak reaching a magnitude of approximately 1276.6 near the center of the plot.

```

03/01/88 13:20:37 5/02/88 11:51:30/NTEPM4.TXA]
Original file = K3.RAW 5/02/88 11:51:30
Object = sphere, horns, no barriers
IX scan starts: 1.02300 1.02400 SI RX scan starts .35050, 1.19000 m.
Object at 1.02300 1.02400 1.10500 m.
Delta-k = .0100
Waveguide a,b = .0229 .0102 a., frequency = 10.000 GHz
IX pattern size: 1 by 14 RX pattern size: 64 by 64
IX RX orientation: 161 1.94500 0.0
IX scan = 0.00000 by 1.94500
Wavevector = 2.07430 2.02845 0 /m, delta-k = 6.54498 /m
Kx,Ky (haz) = -0.7230 -1.600 1.1030 m
Kz = .450
Probe angles:
az = 7.00 0.00 deg
az,az1 = 7.00 0.00 deg
az,az2 = 7.00 0.00 deg
az,az3 = 7.00 0.00 deg
az,az4 = 7.00 0.00 deg
az,az5 = 7.00 0.00 deg
az,az6 = 7.00 0.00 deg
az,az7 = 7.00 0.00 deg
az,az8 = 7.00 0.00 deg
az,az9 = 7.00 0.00 deg
az,az10 = 7.00 0.00 deg
az,az11 = 7.00 0.00 deg
az,az12 = 7.00 0.00 deg
az,az13 = 7.00 0.00 deg
az,az14 = 7.00 0.00 deg
az,az15 = 7.00 0.00 deg
az,az16 = 7.00 0.00 deg
az,az17 = 7.00 0.00 deg
az,az18 = 7.00 0.00 deg
az,az19 = 7.00 0.00 deg
az,az20 = 7.00 0.00 deg
az,az21 = 7.00 0.00 deg
az,az22 = 7.00 0.00 deg
az,az23 = 7.00 0.00 deg
az,az24 = 7.00 0.00 deg
az,az25 = 7.00 0.00 deg
az,az26 = 7.00 0.00 deg
az,az27 = 7.00 0.00 deg
az,az28 = 7.00 0.00 deg
az,az29 = 7.00 0.00 deg
az,az30 = 7.00 0.00 deg
az,az31 = 7.00 0.00 deg
az,az32 = 7.00 0.00 deg
az,az33 = 7.00 0.00 deg
az,az34 = 7.00 0.00 deg
az,az35 = 7.00 0.00 deg
az,az36 = 7.00 0.00 deg
az,az37 = 7.00 0.00 deg
az,az38 = 7.00 0.00 deg
az,az39 = 7.00 0.00 deg
az,az40 = 7.00 0.00 deg
az,az41 = 7.00 0.00 deg
az,az42 = 7.00 0.00 deg
az,az43 = 7.00 0.00 deg
az,az44 = 7.00 0.00 deg
az,az45 = 7.00 0.00 deg
az,az46 = 7.00 0.00 deg
az,az47 = 7.00 0.00 deg
az,az48 = 7.00 0.00 deg
az,az49 = 7.00 0.00 deg
az,az50 = 7.00 0.00 deg
az,az51 = 7.00 0.00 deg
az,az52 = 7.00 0.00 deg
az,az53 = 7.00 0.00 deg
az,az54 = 7.00 0.00 deg
az,az55 = 7.00 0.00 deg
az,az56 = 7.00 0.00 deg
az,az57 = 7.00 0.00 deg
az,az58 = 7.00 0.00 deg
az,az59 = 7.00 0.00 deg
az,az60 = 7.00 0.00 deg
az,az61 = 7.00 0.00 deg
az,az62 = 7.00 0.00 deg
az,az63 = 7.00 0.00 deg
az,az64 = 7.00 0.00 deg
az,az65 = 7.00 0.00 deg
az,az66 = 7.00 0.00 deg
az,az67 = 7.00 0.00 deg
az,az68 = 7.00 0.00 deg
az,az69 = 7.00 0.00 deg
az,az70 = 7.00 0.00 deg
az,az71 = 7.00 0.00 deg
az,az72 = 7.00 0.00 deg
az,az73 = 7.00 0.00 deg
az,az74 = 7.00 0.00 deg
az,az75 = 7.00 0.00 deg
az,az76 = 7.00 0.00 deg
az,az77 = 7.00 0.00 deg
az,az78 = 7.00 0.00 deg
az,az79 = 7.00 0.00 deg
az,az80 = 7.00 0.00 deg
az,az81 = 7.00 0.00 deg
az,az82 = 7.00 0.00 deg
az,az83 = 7.00 0.00 deg
az,az84 = 7.00 0.00 deg
az,az85 = 7.00 0.00 deg
az,az86 = 7.00 0.00 deg
az,az87 = 7.00 0.00 deg
az,az88 = 7.00 0.00 deg
az,az89 = 7.00 0.00 deg
az,az90 = 7.00 0.00 deg
az,az91 = 7.00 0.00 deg
az,az92 = 7.00 0.00 deg
az,az93 = 7.00 0.00 deg
az,az94 = 7.00 0.00 deg
az,az95 = 7.00 0.00 deg
az,az96 = 7.00 0.00 deg
az,az97 = 7.00 0.00 deg
az,az98 = 7.00 0.00 deg
az,az99 = 7.00 0.00 deg
az,az100 = 7.00 0.00 deg
az,az101 = 7.00 0.00 deg
az,az102 = 7.00 0.00 deg
az,az103 = 7.00 0.00 deg
az,az104 = 7.00 0.00 deg
az,az105 = 7.00 0.00 deg
az,az106 = 7.00 0.00 deg
az,az107 = 7.00 0.00 deg
az,az108 = 7.00 0.00 deg
az,az109 = 7.00 0.00 deg
az,az110 = 7.00 0.00 deg
az,az111 = 7.00 0.00 deg
az,az112 = 7.00 0.00 deg
az,az113 = 7.00 0.00 deg
az,az114 = 7.00 0.00 deg
az,az115 = 7.00 0.00 deg
az,az116 = 7.00 0.00 deg
az,az117 = 7.00 0.00 deg
az,az118 = 7.00 0.00 deg
az,az119 = 7.00 0.00 deg
az,az120 = 7.00 0.00 deg
az,az121 = 7.00 0.00 deg
az,az122 = 7.00 0.00 deg
az,az123 = 7.00 0.00 deg
az,az124 = 7.00 0.00 deg
az,az125 = 7.00 0.00 deg
az,az126 = 7.00 0.00 deg
az,az127 = 7.00 0.00 deg
az,az128 = 7.00 0.00 deg
az,az129 = 7.00 0.00 deg
az,az130 = 7.00 0.00 deg
az,az131 = 7.00 0.00 deg
az,az132 = 7.00 0.00 deg
az,az133 = 7.00 0.00 deg
az,az134 = 7.00 0.00 deg
az,az135 = 7.00 0.00 deg
az,az136 = 7.00 0.00 deg
az,az137 = 7.00 0.00 deg
az,az138 = 7.00 0.00 deg
az,az139 = 7.00 0.00 deg
az,az140 = 7.00 0.00 deg
az,az141 = 7.00 0.00 deg
az,az142 = 7.00 0.00 deg
az,az143 = 7.00 0.00 deg
az,az144 = 7.00 0.00 deg
az,az145 = 7.00 0.00 deg
az,az146 = 7.00 0.00 deg
az,az147 = 7.00 0.00 deg
az,az148 = 7.00 0.00 deg
az,az149 = 7.00 0.00 deg
az,az150 = 7.00 0.00 deg
az,az151 = 7.00 0.00 deg
az,az152 = 7.00 0.00 deg
az,az153 = 7.00 0.00 deg
az,az154 = 7.00 0.00 deg
az,az155 = 7.00 0.00 deg
az,az156 = 7.00 0.00 deg
az,az157 = 7.00 0.00 deg
az,az158 = 7.00 0.00 deg
az,az159 = 7.00 0.00 deg
az,az160 = 7.00 0.00 deg
az,az161 = 7.00 0.00 deg
az,az162 = 7.00 0.00 deg
az,az163 = 7.00 0.00 deg
az,az164 = 7.00 0.00 deg
az,az165 = 7.00 0.00 deg
az,az166 = 7.00 0.00 deg
az,az167 = 7.00 0.00 deg
az,az168 = 7.00 0.00 deg
az,az169 = 7.00 0.00 deg
az,az170 = 7.00 0.00 deg
az,az171 = 7.00 0.00 deg
az,az172 = 7.00 0.00 deg
az,az173 = 7.00 0.00 deg
az,az174 = 7.00 0.00 deg
az,az175 = 7.00 0.00 deg
az,az176 = 7.00 0.00 deg
az,az177 = 7.00 0.00 deg
az,az178 = 7.00 0.00 deg
az,az179 = 7.00 0.00 deg
az,az180 = 7.00 0.00 deg
az,az181 = 7.00 0.00 deg
az,az182 = 7.00 0.00 deg
az,az183 = 7.00 0.00 deg
az,az184 = 7.00 0.00 deg
az,az185 = 7.00 0.00 deg
az,az186 = 7.00 0.00 deg
az,az187 = 7.00 0.00 deg
az,az188 = 7.00 0.00 deg
az,az189 = 7.00 0.00 deg
az,az190 = 7.00 0.00 deg
az,az191 = 7.00 0.00 deg
az,az192 = 7.00 0.00 deg
az,az193 = 7.00 0.00 deg
az,az194 = 7.00 0.00 deg
az,az195 = 7.00 0.00 deg
az,az196 = 7.00 0.00 deg
az,az197 = 7.00 0.00 deg
az,az198 = 7.00 0.00 deg
az,az199 = 7.00 0.00 deg
az,az200 = 7.00 0.00 deg
az,az201 = 7.00 0.00 deg
az,az202 = 7.00 0.00 deg
az,az203 = 7.00 0.00 deg
az
```

Y-12

[illegible]

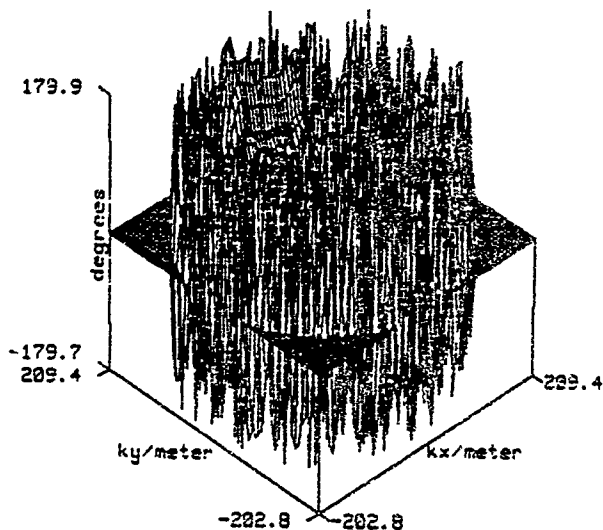
V-13

A 3D surface plot showing the magnitude of the 2D Fourier transform. The vertical axis is labeled 'magnitude' and ranges from 0 to 251.5. The horizontal axes are labeled 'kx/meter' and 'ky/meter'. The 'kx/meter' axis ranges from -202.8 to 229.4, and the 'ky/meter' axis ranges from -209.4 to 209.4. The plot shows a complex, multi-peaked surface with a prominent central peak and several smaller peaks, indicating a non-uniform distribution of the original function.

[illegible]

V-14

Phase of S-theta (degrees)
S-theta



Phase of S-theta (degrees)
S-theta

```

C:/5/02/98,16:21:39/MC4.TXA)
Original file = MC4RAW 5/02/98 16:21:39
Q0:0:0:0 sphere, 0.000, 0.000, 0.000 m, Rx scan starts .33050, 1.19000 m.
Rx scan starts .33050, 1.19000 m, Rx scan starts .33050, 1.19000 m.
Object at 1.00000, 1.00000, 1.00000 m.
Delta-x,y,z = 0.000, 0.000, 0.000 m.
Wavequick a,b = 0.000, 0.0102 m., frequency = 10.000 GHz
Rx pattern size: 1 by 1, Rx pattern size: 64 by 64
Rx,Ry orientation: 1.1 1.3 0.0 0.0
Wavelength = 0.02998 m
Rx,Ry (mm) = 24.999, 24.999 mm, delta-x = 6.34400 m
Rx,Ry (mm) = 24.999, 24.999 mm
Probe angles: .00, 90.00 deg.

```

Figure V-12. S_θ Phase

semicircular region that is approximately

$$-50 \text{ meter}^{-1} < k_x < 50 \text{ meter}^{-1}$$

$$60 \text{ meter}^{-1} < k_y < 140 \text{ meter}^{-1}.$$

The actual region of validity is blurred due to the sampling geometry and signal "leakage" between adjacent DFT values. The leakage has been reduced in these plots by applying a smoothing taper before performing the Fourier transforms. The region of validity appears in the figure as an area of smoothly-varying phase that is distinct from the phase noise that covers the remainder of the k_x - k_y plane.

F. CUT PLOTS

The region of definition appears also in cut plots through the k_x - k_y plane. A cut through Figure V-12 along the line $k_x=0$ yields the plot shown in Figure V-13. The phase function is well-behaved for $60 \text{ meter}^{-1} < k_y < 140 \text{ meter}^{-1}$, while it oscillates rapidly and randomly outside that region.

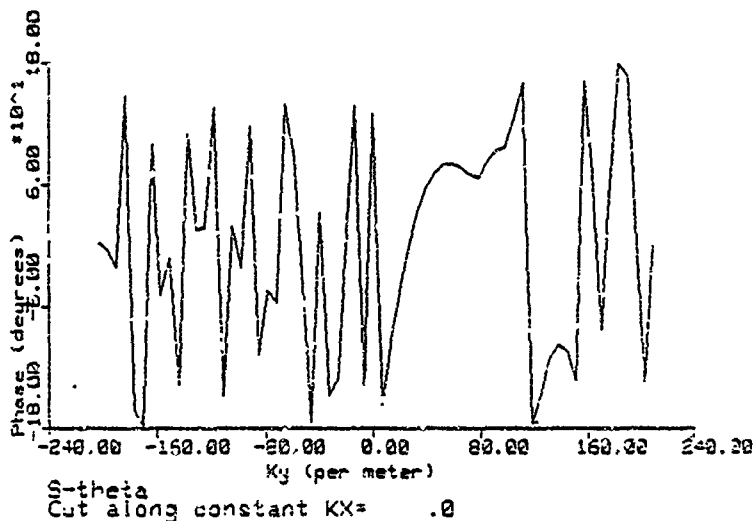
Figures V-14 through V-26 show overlay plots of the predicted and measured S_θ , S_φ , S_x , and S_y in cuts along the k_x and k_y axes. A fixed offset of 6 db has been added to the measured scattering magnitude to facilitate comparison of predictions and measured data in these plots. This offset, occurring consistently in all of the measured scattering data, is attributed to a calibration inconsistency that time limitations prevent our resolving. Recall that the region of definition in these plots is approximately

$$-50 \text{ meter}^{-1} < k_x < 50 \text{ meter}^{-1}$$

$$60 \text{ meter}^{-1} < k_y < 140 \text{ meter}^{-1}.$$

Figure V-14 shows the predicted and measured magnitude of the function S_θ along a cut $k_x = 0 \text{ meter}^{-1}$. The deep notch in the predicted magnitude is a point of phase ambiguity in this coordinate system representation. Over the region of definition, the reconstructed magnitude is essentially flat with about ± 2 db of residual ripple.

Figure V-15 shows the predicted and measured magnitude of the function S_φ along a cut $k_x = 0 \text{ meter}^{-1}$. Along this cut, the predicted S_φ is zero except for an impulse at the

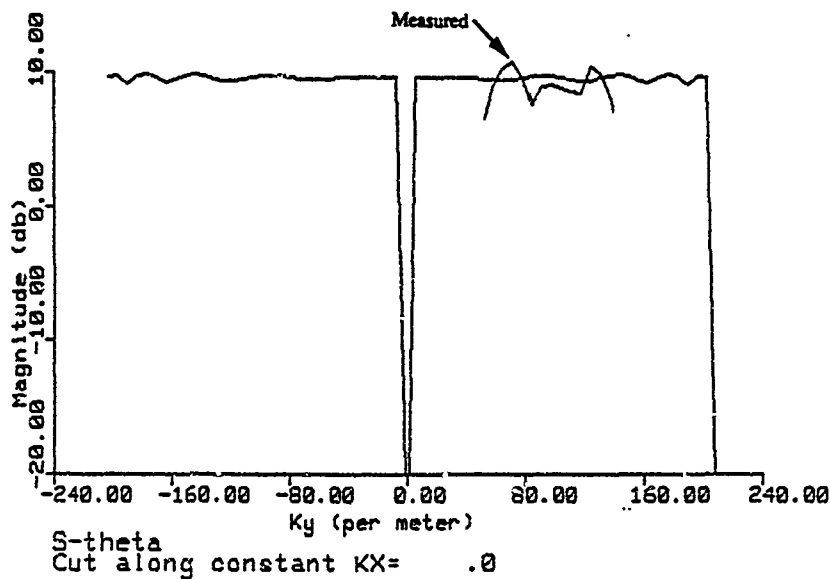


```

1/ 3/27/80, 16:51:30/M34 TYA1
Original file = M3.RAW 3/27/80 16:51:30
Object = sphere, 32000, no barrier
Scan starts at 1.21600, 1.02400, 1.02400
Object at 1.21600, 1.02400, 1.02400
Delta x-y = .0120 m
Waveguide x-h = .0120 m, frequency = 12.000 GHz
Pattern size: 101 x 101
Pattern size: 63 by 31
Scan size: 101 x 101
Scan size: 63 by 31
Wavelength = .0248 m, delta-y = 5.24408 m
Kx (1/m) = 40.317, Ky (1/m) = 40.317
Cbe angles: 30, 30.70 deg.

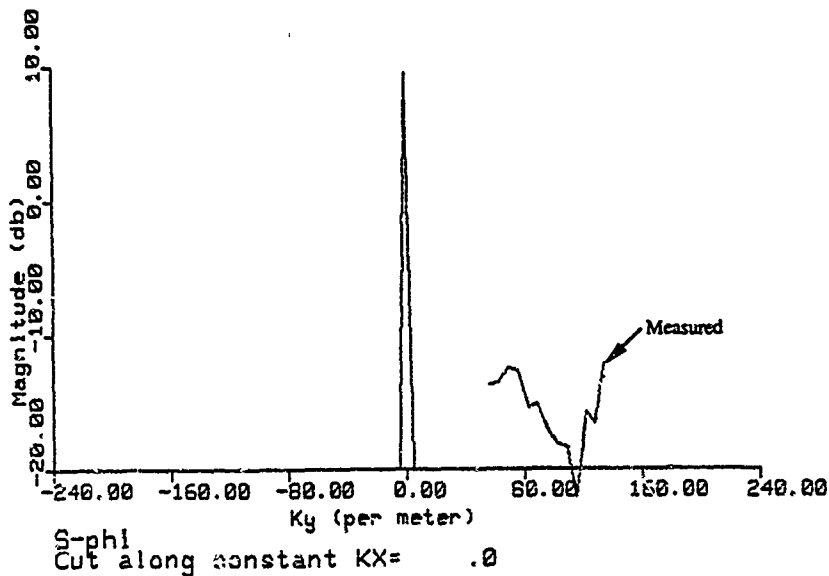
```

Figure V-13. S_θ Phase Cut Along $k_x = 0$



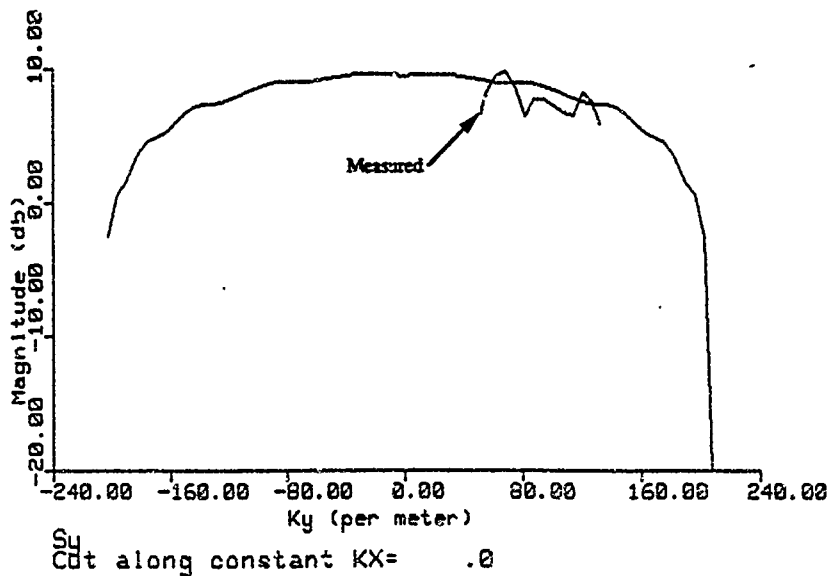
Predicted S11 of SPHERE with E-theta illumination
 TX location = 1.02300 1.02700 0.00000
 X location = 1.02300 1.02700 0.00000
 dlatky = .01300 lambda = 1.02600
 radius = .078200 m lambda = .03000 k = 209.43952

Figure V-14. Predicted and Measured S_{θ} Magnitude Cut: $k_x = 0$



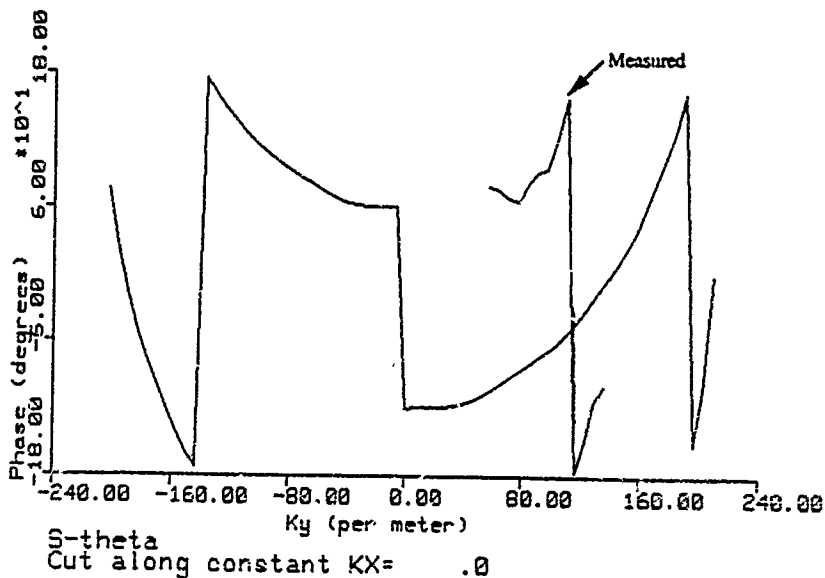
Predicted S11 of SPHERE with E-theta illumination
 Tx location = 1.02500 -1.02700 0.00000
 x y z var object = 1.02500 1.02600 1.10500
 deltax = .01500 lambda = .03000 k = 209.43952
 radius = .076200 a

Figure V-15. Predicted and Measured S_{ϕ} Magnitude Cut: $k_x = 0$



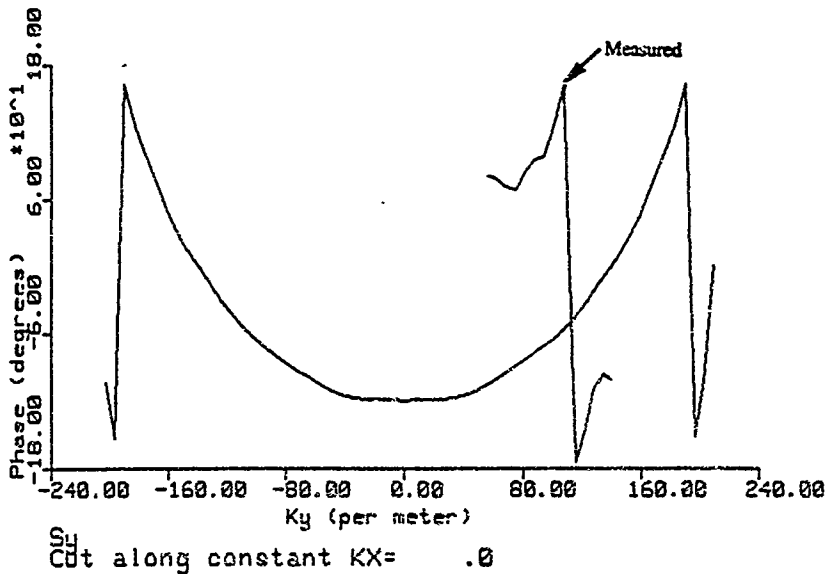
Predicted S_{11} of SPHEFF with E-theta Illumination
 Tx location = 1.02300 1.02700 0.0000
 X location for object = 1.02300 1.02600 1.10500
 daltxy = .01300 lambda = .03000 k = 209.43952
 radius = .076200 m

Figure V-16. Predicted and Measured S_y Magnitude Cut: $k_x = 0$



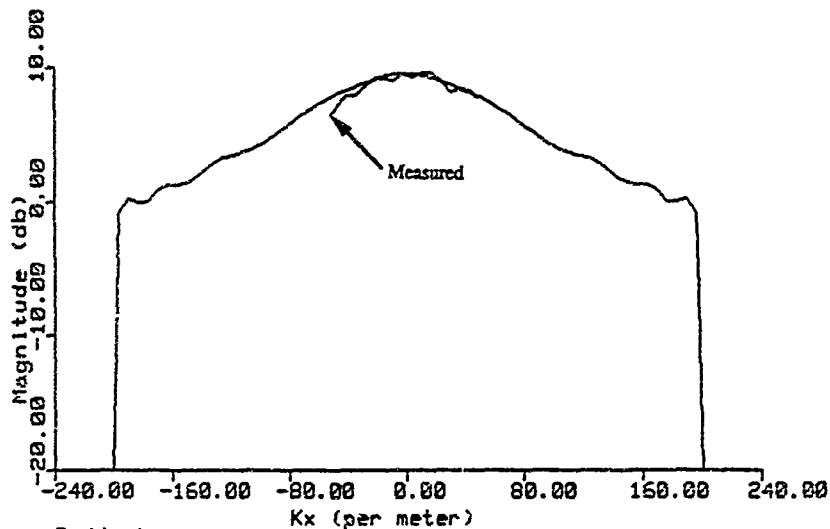
Predicted S11 of SPHERE with E-theta illumination
 Tx location = 1.02300 1.022700 1.020000
 x: for object = 1.02300 1.02600 1.10500
 def: y: = .01500 lambda = .03000 k = 209.43952
 radius = .076200 m

Figure V-17. Predicted and Measured S_{θ} Phase Cut: $k_x = 0$



Predicted S₁₁ of SPHERE with E-theta illumination
 x location = 1.02300 1.02700 1.02800 1.03000
 x location for object = 1.02300 1.02500 1.02600 1.02800
 deltax = .01300 lambda = .03000 k = 209.43752
 radius = .076200

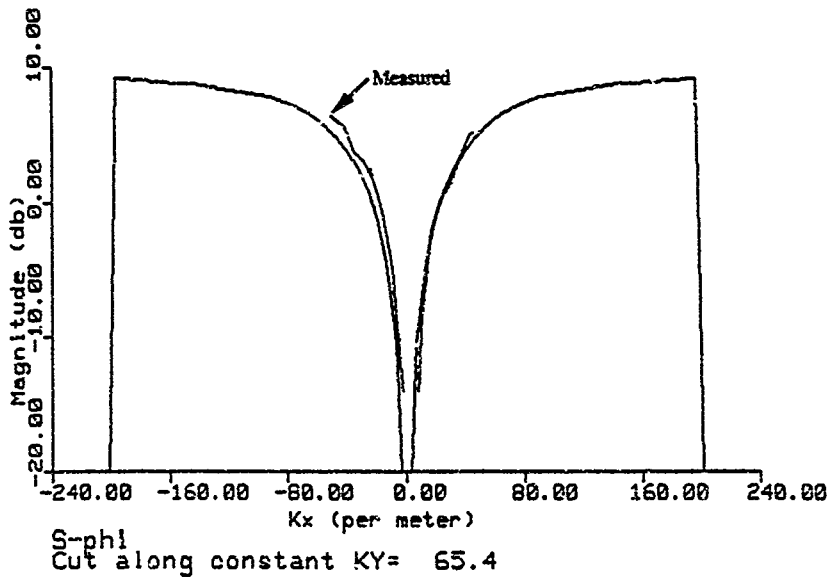
Figure V-18. Predicted and Measured S_y Phase Cut: k_x = 0



S-theta
Cut along constant KY= 65.4

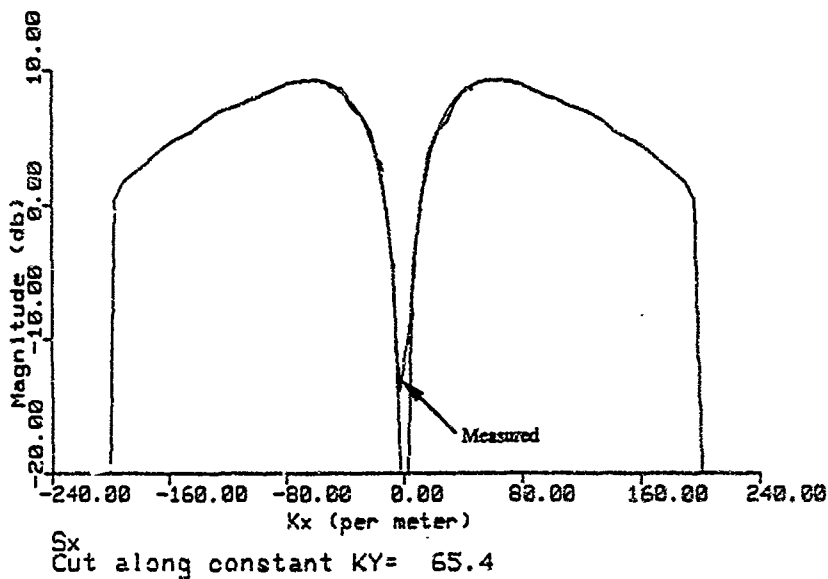
Predicted S11 of SPHERE with E-theta illumination
 TX location = 1.02300 1.02700 0.0000
 X-Y-Z for object = 1.02300 1.02600 1.10500
 deltax = .01500 lambda = .03000 k = 209.43952
 radius = .076200 m

Figure V-19. Predicted and Measured S_{θ} Magnitude Cut: $k_y = 65.4$



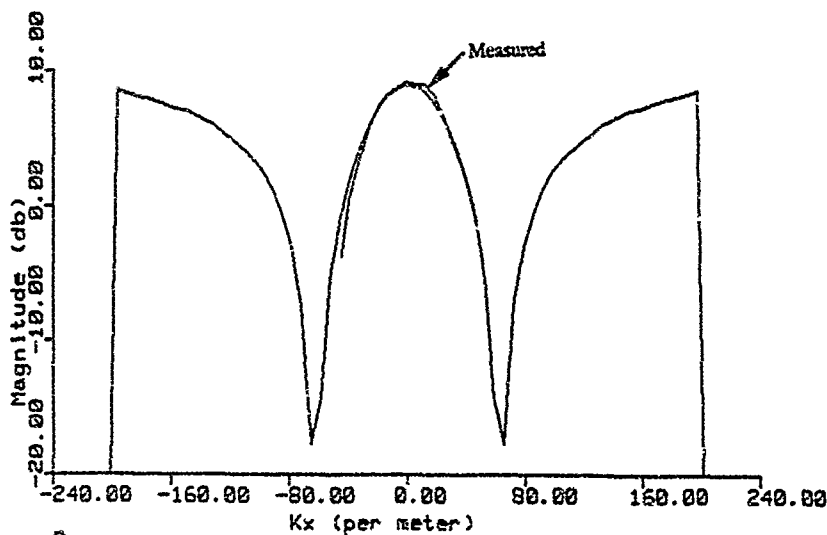
Predicted S11 of SPHERE with E-theta illumination
 tx location = 1.02300 1.02700 0.00000
 x location for object = 1.02300 1.02600 1.10300
 deltax = 0.01500 lambda = .03000 k = 209.43952
 radius = .076200 m

Figure V-20. Predicted and Measured S_{ϕ} Magnitude Cut: $k_y = 65.4$



Predicted S₁₁ of SPHERE with E-theta illumination
 K location = 1.02300 1.02700 1.0280000
 Y for object = 1.02300 1.02600 1.02800
 Delta Y = .01300 lambda = .03000 k = 209.43952
 radius = .076200 m

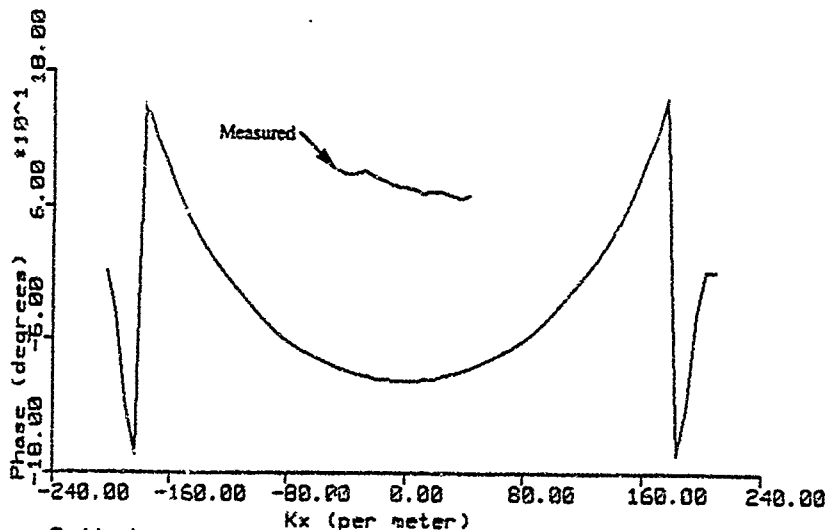
Figure V-21. Predicted and Measured S_x Magnitude Cut: k_y = 65.4



S_{y}
Cut along constant $KY = 65.4$

Predicted S_{y} of SPHERE with E-theta illumination
 Tx location = 1.02300 1.02700 1.00000
 Rx location = 1.02300 1.02700 1.00000
 radius = .076200 m
 lambda = .03000 m
 k = 209.43952

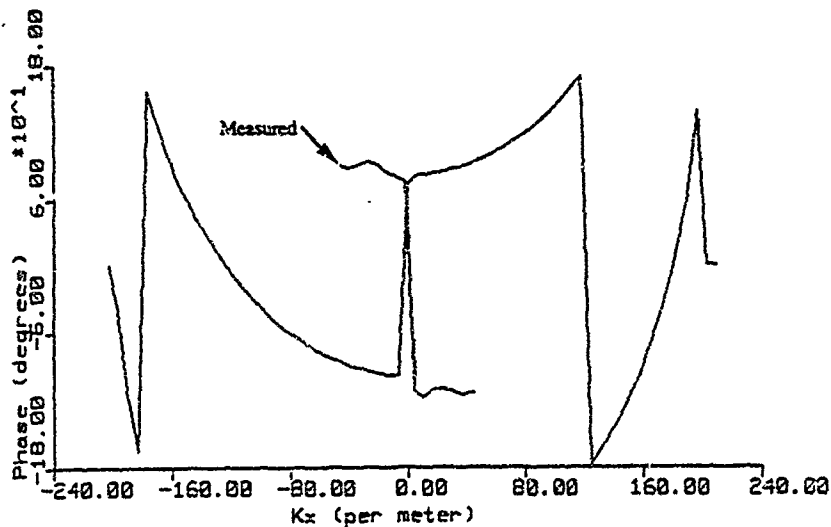
Figure V-22. Predicted and Measured S_{y} Magnitude Cut: $k_y = 65.4$



S-theta
Cut along constant KY= 65.4

Predicted S11 of SPHERE with E-theta illumination
 X location = 1.02300 1.02700 1.00000
 X location for object = 1.02300 1.02600 1.10500
 deltax = .01500 lambda = .03000 k = 209.43952
 radius = .076200

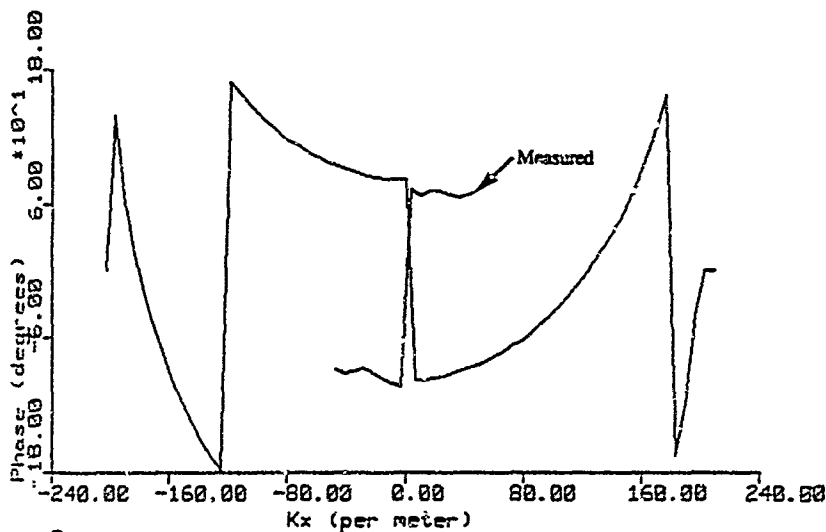
Figure V-23. Predicted and Measured S_{θ} Phase Cut: $k_y = 65.4$



S-phi
Cut along constant KY= 65.4

Predicted S11 of SPHERE with E-theta illumination
 x location = 1.02300 k = 0.02700
 x location for object = 1.02300 k = 0.02600
 radius = .01500 lambda = .03000 k = 209.43952

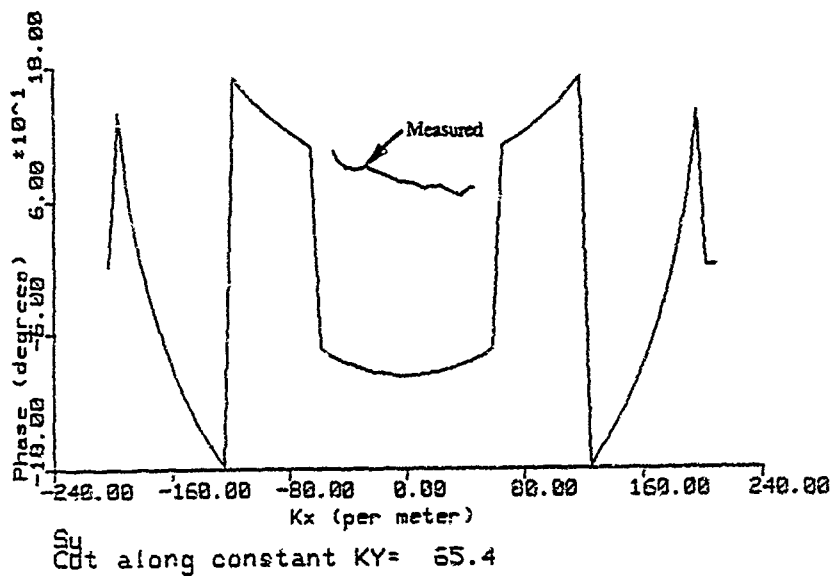
Figure V-24. Predicted and Measured S_{ϕ} Phase Cut: $k_y = 65.4$



Sx
Cut along constant KY= 65.4

Predicted S11 of SPHERE with E-theta illumination
 Tx location = 1.02300 1.02700 0.00000
 object = 1.02300 1.02500 1.10500
 delta = .01500 lambda = .03000 k = 209.43952
 radius = .076200 m

Figure V-25. Predicted and Measured S_x Phase Cut: $k_y = 65.4$



Predicted S11 of SPHERE with E-theta illumination
 Kx location = 1.02500 1.02700 1.03000
 object = 1.02300 1.02600 1.03000
 radius = .01500 lambda = .03600 k = 209.43952

Figure V-26. Predicted and Measured S_y Phase Cut: $k_y = 65.4$

origin. The reconstructed function is about -20 db from S_θ indicating that cross-polarization leakage occurred due to antenna misalignment.

Figure V-16 shows the predicted and measured magnitude of the function S_y along a cut $k_x = 0 \text{ meter}^{-1}$. The predicted S_y is accurately reconstructed with about ± 2 db of ripple.

Figure V-17 shows the predicted and measured phase of the function S_θ along a cut $k_x = 0 \text{ meter}^{-1}$. In these phase cut plots, it is important to view only the actual region of definition given above. Over that region, the phase agreement is reasonably good; the upward parabolic slope to the right is discernible.

Figure V-18 shows the predicted and measured magnitude of the function S_y along a cut $k_x = 0 \text{ meter}^{-1}$. Again, over the region of definition, the reconstructed phase agrees reasonably well with the predicted phase, provided that one takes into account the phase wrap that occurs at about 1.5 meter^{-1} .

Figure V-19 shows the predicted and measured magnitude of the function S_θ along a cut $k_x = 65.4 \text{ meter}^{-1}$. Along this cut, where the region of definition is approximately $|k_y| \leq 50 \text{ meter}^{-1}$, the agreement between the two plots is excellent, with about 2 db maximum error.

Figure V-20 shows the predicted and measured magnitude of the function S_ϕ along a cut $k_x = 65.4 \text{ meter}^{-1}$. Agreement is again quite good, with the same offset of 6 db. The same may be said of Figures V-21 and V-22 which show the predicted and measured magnitude of the functions S_x and S_y along the same cut.

Figures V-23 through V-28 show the predicted and measured phases of the functions S_θ , S_ϕ , S_x , and S_y along a cut $k_x = 65.4 \text{ meter}^{-1}$. The measured phase plots show a linear additive phase term with slope of about 0.3 degree/meter; this term is probably due to target misalignment. There is in addition a phase inversion of S_ϕ and S_x which affects the manner in which those two functions change as the origin ($k_x = 0$) is crossed.

G. SUMMARY

In this section we presented both predictions and near-field measurements of far-field bistatic scattering of the conducting sphere. The key points of the presentation may be summarized as follows:

- (1) The magnitude of the measured scattering agrees well with the predicted scattering within the region of definition of the k-space reconstruction. The discrepancy between measurement and prediction consists of a ± 2 db peak ripple superimposed upon a constant calibration offset of 6 db.
- (2) Agreement of the scattering phase is not as good. This is due primarily to two effects:
 - (a) Phase measurements are particularly sensitive to antenna axial alignment perpendicular to the plane of scanning.
 - (b) "Wrap-around" occurs in the phase of the measured data due to (fixed) phase offsets in the network analyzer.
- (3) Coherent background subtraction is an effective technique for improving signal-to-noise ratio.
- (4) Spatial filtering to remove unwanted scattering from the environment may be performed in the k-space Fourier transform representation of the measured data.
- (5) Sidelobes in the Fourier-transformed measurements are greatly reduced by smoothing the measurements with a smoothing window prior to performing the Fourier transforms.
- (6) Probe-to-probe coupling is readily separated from the desired target scattering information in the k-space representation of the measured data.

CHAPTER VI

DATA REDUCTION INVESTIGATION

A. INTRODUCTION

The existing algorithms for computing near-field antenna patterns and radar cross sections of objects impose significant computational burdens. In this section we describe modifications and/or alternatives to the existing algorithms which offer the potential for reducing the number of computational steps needed to obtain useful near-field measurement data. The investigations concentrate on three primary computational alternatives described in the following sections. The following other computational alternatives are not considered here: (1) adaptive nonuniform sampling, (2) non-rectangular lattice (or grid) sample spacing, (3) statistically reduced number of near-field data used in the far-field transform, and (4) derivative data measured in the near-field.

Two approaches for reducing the burden of the near-field computations are considered here. The first approach is based on writing the equations for computing the scattering matrix directly in vector and matrix notation. The current equations compute the scattering matrix in several steps. Each step requires computations and transfers to data storage which impose computational burdens. These burdens can be reduced by using a direct matrix formulation of the scattering equation. In addition, the other alternatives for reducing either the amount of measured near-field data or the computations necessary to determine the scattering matrix are more convenient to work with in terms of the direct matrix formulations.

The second approach is based on expansions of the near-field functional components which allow us to impose constraints on the near-field functions. The constraints can be based on (1) the desired or expected analytical behavior of the functions, (2) the physics of the measurement environment, or (3) the information content of the data process.

B. MATRIX OPERATIONS

In investigating the computations from a matrix perspective, we first rewrite the equations for the scattering matrix in vector matrix notation. Expressed in this form, the scattering equation is more easily interpreted and adapted to improve the efficiency of computing the relationships between the scattering components. Next we relate the scattering matrix formulation with the vector formulation of the first subsection and compare the results.

The explicit solution for the scattering matrix $\underline{T}_{11}(\vec{k}, \vec{l})$ in terms of the measured data array parallels the solution given in Chapter II except that this derivation solves for the scattering matrix in terms of the measured data vector and matrix representations. The equation development is described in terms of the continuous Fourier transform for exposition convenience. Equivalent results can be obtained for the point measurement computation of the Discrete Fourier transform using the Fast Fourier transform.

The bistatic measurement equation is

$$b_0(\vec{r}_1, \vec{r}_2) = \iint \vec{f}_{01}^t(\vec{k}) \cdot \vec{T}_{11}(\vec{k}, \vec{l}) \cdot \vec{f}_{10}(\vec{l}) e^{i\vec{k} \cdot \vec{r}_2 - i\vec{l} \cdot \vec{r}_1} d\vec{k} d\vec{l}$$

where

$\vec{f}_{01}^t(\vec{k})$ = the vector transpose of $\vec{f}_{01}(\vec{k})$

\vec{k} = scattering (emerging) direction,

\vec{l} = incident (illumination) direction,

$\vec{r}_1 = P_{xr}\hat{e}_x + P_{yr}\hat{e}_y + P_{zr}\hat{e}_z$ = receiver probe coordinates,

$\vec{r}_2 = P_{xt}\hat{e}_x + P_{yt}\hat{e}_y + P_{zt}\hat{e}_z$ = transmit probe coordinates.

In the laboratory we measure a multidimensional scalar complex array $M(P_{xr}, P_{yr}, P_{xt}, P_{yt}, \xi_r, \xi_t)$ at discrete points whose components elements are the measured values of $b_0(\vec{r}_1, \vec{r}_2)$

$$(P_{xr}, P_{yr}, P_{zt}) \in \{(P_{xr_i}, P_{yr_i}, P_{zt_i})\}, P_{zt} = \text{constant},$$

$$(P_{xt}, P_{yt}, P_{zt}) \in \{(P_{xt_i}, P_{yt_i}, P_{zt_i})\}, P_{zt} = \text{constant},$$

$\xi_r = \{1, 2\} \equiv$ an index denoting receive probe orientation, and

$\xi_t = \{1, 2\} \equiv$ an index denoting transmit probe orientation.

In the first step of the solution, we take the inverse Fourier transform with respect to the respective transmitter and receiver locations $\mathbf{r}_1, \mathbf{r}_2$ of both sides of the equation.

$$\begin{aligned} \iint b_0(\mathbf{r}_1, \mathbf{r}_2) e^{-i\tilde{\mathbf{m}} \cdot \mathbf{r}_1 - i\tilde{\mathbf{n}} \cdot \mathbf{r}_2} d\mathbf{r}_1 d\mathbf{r}_2 &= \iiint \tilde{\mathbf{I}}_{01}^t(\tilde{\mathbf{k}}) \cdot \bar{\mathbf{T}}_{11}(\tilde{\mathbf{k}}, \tilde{\mathbf{l}}) \cdot \tilde{\mathbf{I}}_{10}(\tilde{\mathbf{l}}) \cdot \\ &\quad e^{i\tilde{\mathbf{k}} \cdot \mathbf{r}_2 - i\tilde{\mathbf{l}} \cdot \mathbf{r}_1} d\tilde{\mathbf{k}} d\tilde{\mathbf{l}} e^{-i\tilde{\mathbf{m}} \cdot \mathbf{r}_1 - i\tilde{\mathbf{n}} \cdot \mathbf{r}_2} d\mathbf{r}_1 d\mathbf{r}_2 \\ &= (2\pi)^6 \iint \tilde{\mathbf{I}}_{01}^t(\tilde{\mathbf{k}}) \cdot \bar{\mathbf{T}}_{11}(\tilde{\mathbf{k}}, \tilde{\mathbf{l}}) \cdot \tilde{\mathbf{I}}_{10}(\tilde{\mathbf{l}}) \cdot \delta(\tilde{\mathbf{m}} + \tilde{\mathbf{l}}) \cdot \delta(\tilde{\mathbf{n}} - \tilde{\mathbf{k}}) d\tilde{\mathbf{k}} d\tilde{\mathbf{l}} \\ &= (2\pi)^6 \tilde{\mathbf{I}}_{01}^t(\tilde{\mathbf{n}}) \cdot \bar{\mathbf{T}}_{11}(\tilde{\mathbf{n}}, -\tilde{\mathbf{m}}) \cdot \tilde{\mathbf{I}}_{10}(-\tilde{\mathbf{m}}) \end{aligned}$$

where $\tilde{\mathbf{k}}$ is defined in terms of its wavenumber k_{xr}, k_{yr}, k_{zr} components in the coordinate system of $\bar{\mathbf{T}}_{11}(\tilde{\mathbf{k}}, \tilde{\mathbf{l}})$. Note that ξ_r and ξ_t are constants in the above equation. We now write the equation in terms of the $\tilde{\mathbf{k}}, \tilde{\mathbf{l}}$ arguments

$$B(\tilde{\mathbf{k}}, -\tilde{\mathbf{l}}) = (2\pi)^6 \tilde{\mathbf{I}}_{01}^t(\tilde{\mathbf{k}}) \cdot \bar{\mathbf{T}}_{11}(\tilde{\mathbf{k}}, \tilde{\mathbf{l}}) \cdot \tilde{\mathbf{I}}_{10}(\tilde{\mathbf{l}})$$

where

$$B(\tilde{\mathbf{k}}, -\tilde{\mathbf{l}}) = \iint b_0(\mathbf{r}_1, \mathbf{r}_2) \cdot e^{-i\tilde{\mathbf{k}} \cdot \mathbf{r}_2 + i\tilde{\mathbf{l}} \cdot \mathbf{r}_1} d\mathbf{r}_1 d\mathbf{r}_2.$$

The minus sign of the vector $\tilde{\mathbf{l}}$ indicates the direction of the incident radiation relative to the scattering object. In our laboratory measurements the elements of $M(\cdot)$ are built up by a concatenation of scans by the receive probe; during each scan we vary P_{xr} and P_{yr} and hold $P_{zr}, P_{xt}, P_{yt}, \xi_r$, and ξ_t constant. If

N_{xr} = number of discrete values of P_{xr} ,

N_{yr} = number of discrete values of P_{yr} ,

N_{xt} = number of discrete values of P_{xt} ,

N_{yt} = number of discrete values of P_{yt} ,

then $M(\cdot)$ consists of $4N_{xt}N_{yt}$ matrices, each of which contains $N_{xt}N_{yt}$ complex scalars. The factor of 4 comes from $\xi_r = \{1, 2\}$ and $\xi_t = \{1, 2\}$.

The vectors $\bar{I}_{01}(\vec{k})$ and $\bar{I}_{10}(\vec{l})$ have specific components reflecting their dependence on the probe orientations ($\xi_r = \{1, 2\}$, $\xi_t = \{1, 2\}$) polarization components (θ, ϕ) of the transmitted and received signals. Next we define two 2×2 matrices $\bar{I}\bar{K}$ and $\bar{I}\bar{L}$ composed of the respective $\bar{I}_{01}^t(\vec{k})$ and $\bar{I}_{10}(\vec{l})$ vectors in terms of their specific function arguments ξ, ϕ and θ , thus

$$\bar{I}\bar{K} = \begin{bmatrix} \bar{I}_{01}^t(\vec{k}, \xi_{r1}) \\ \bar{I}_{01}^t(\vec{k}, \xi_{r2}) \end{bmatrix} = \begin{bmatrix} I_{01\theta}(\vec{k}, \xi_{r1}) & I_{01\phi}(\vec{k}, \xi_{r1}) \\ I_{01\theta}(\vec{k}, \xi_{r2}) & I_{01\phi}(\vec{k}, \xi_{r2}) \end{bmatrix}$$

$$\bar{I}\bar{L} = \begin{bmatrix} \bar{I}_{10}(\vec{l}, \xi_{t1}) \\ \bar{I}_{10}(\vec{l}, \xi_{t2}) \end{bmatrix} = \begin{bmatrix} I_{10\theta}(\vec{l}, \xi_{t1}) & I_{10\phi}(\vec{l}, \xi_{t1}) \\ I_{10\theta}(\vec{l}, \xi_{t2}) & I_{10\phi}(\vec{l}, \xi_{t2}) \end{bmatrix}$$

The quantity $B(\vec{k}, -\vec{l})$ is also a function of the probe and polarization arguments so we define \bar{B} , a 2×2 matrix with the diagonal terms specified by the respective values of $B(\cdot)$ for each of the four vector combinations of the $\bar{I}\bar{K}$ ($\bar{I}\bar{L}$) matrices. Using the above definitions we can write the scattering matrix equation as

$$\bar{B}(\vec{k}, \vec{l}) = (2\pi)^6 \bar{I}\bar{K}(\vec{k}) \cdot \bar{T}_{11}(\vec{k}, \vec{l}) \cdot \bar{I}\bar{L}(\vec{l})^t.$$

If the matrices $\bar{I}\bar{K}$ and $\bar{I}\bar{L}$ have rank two, their inverses exist and we can write the scattering matrix as

$$\bar{T}_{11}(\vec{k}, \vec{l}) = (\bar{I}\bar{K})^{-1} \cdot \bar{B} \cdot (\bar{I}\bar{L}^t)^{-1} / (2\pi)^6.$$

The matrix inverses for the $\bar{I}\bar{K}$ and $\bar{I}\bar{L}^t$ matrices are

$$(\bar{I}\bar{K})^{-1} = \begin{bmatrix} I_{01\phi}(\vec{k}, \xi_{r2}) & -I_{01\phi}(\vec{k}, \xi_{r1}) \\ -I_{01\theta}(\vec{k}, \xi_{r2}) & I_{01\theta}(\vec{k}, \xi_{r1}) \end{bmatrix} / \Delta(r)$$

$$(\bar{I}\bar{L}^t)^{-1} = \begin{bmatrix} I_{10\phi}(\vec{l}, \xi_{t2}) & -I_{10\phi}(\vec{l}, \xi_{t1}) \\ -I_{10\theta}(\vec{l}, \xi_{t2}) & I_{10\theta}(\vec{l}, \xi_{t1}) \end{bmatrix} / \Delta(t)$$

where $\Delta(r)$ and $\Delta(t)$ are respectively

$$\Delta(r) = I_{01\theta}(\vec{k}, \xi_{r1}) I_{01\phi}(\vec{k}, \xi_{r2}) - I_{01\phi}(\vec{k}, \xi_{r1}) I_{01\theta}(\vec{k}, \xi_{r2})$$

$$\Delta(t) = I_{10\theta}(\vec{l}, \xi_{t1}) I_{10\phi}(\vec{l}, \xi_{t2}) - I_{10\phi}(\vec{l}, \xi_{t1}) I_{10\theta}(\vec{l}, \xi_{t2}).$$

The B matrix is given by

$$B = \begin{bmatrix} B_{r1 \ t1} & B_{r1 \ t2} \\ B_{r2 \ t1} & B_{r2 \ t2} \end{bmatrix}$$

The subscripts ri and tj ($i,j=1,2$) in the $B_{ri \ tj}$ terms identify the orientation of the ξ_{ri} , ξ_{tj} probe components. We can then write the scattering matrix, $T_{11}(\vec{k}, \vec{l})$, explicitly in terms of the vector elements and scaling components, $\Delta(r)\Delta(t)(2\pi)^6$, as

$$\begin{bmatrix} I_{01}\phi(\vec{k}, \xi_{r2})B_{r1 \ t1} - I_{01}\phi(\vec{k}, \xi_{r1})B_{r2 \ t1} & I_{01}\phi(\vec{k}, \xi_{r2})B_{r1 \ t2} - I_{01}\phi(\vec{k}, \xi_{r1})B_{r2 \ t2} \\ -I_{01}\phi(\vec{k}, \xi_{r2})B_{r1 \ t1} + I_{01}\phi(\vec{k}, \xi_{r1})B_{r2 \ t1} & -I_{01}\phi(\vec{k}, \xi_{r2})B_{r1 \ t2} + I_{01}\phi(\vec{k}, \xi_{r1})B_{r2 \ t2} \end{bmatrix} \\ \times \begin{bmatrix} I_{01}\phi(\vec{l}, \xi_{t2}) & -I_{01}\phi(\vec{l}, \xi_{t1}) \\ -I_{01}\phi(\vec{l}, \xi_{t1}) & I_{01}\phi(\vec{l}, \xi_{t2}) \end{bmatrix} (\Delta(r)\Delta(t)(2\pi)^6)^{-1}$$

We can now write the elements, T_{ij} ($i,j=1,2$) of the $T_{11}(\vec{k}, \vec{l})$ matrix as

$$\begin{aligned} T_{11} &= (I_{01}\phi(\vec{k}, \xi_{r2})B_{r1 \ t1} - I_{01}\phi(\vec{k}, \xi_{r1})B_{r2 \ t1})I_{01}\phi(\vec{l}, \xi_{t2}) - \\ &\quad I_{01}\phi(\vec{k}, \xi_{r2})B_{r1 \ t2} - I_{01}\phi(\vec{k}, \xi_{r1})B_{r2 \ t2})I_{01}\phi(\vec{l}, \xi_{t1}) (\Delta(r)\Delta(t)(2\pi)^6)^{-1} \\ T_{12} &= (-I_{01}\phi(\vec{k}, \xi_{r2})B_{r1 \ t1} - I_{01}\phi(\vec{k}, \xi_{r1})B_{r2 \ t1})I_{01}\phi(\vec{l}, \xi_{t2}) + \\ &\quad (I_{01}\phi(\vec{k}, \xi_{r2})B_{r1 \ t2} - I_{01}\phi(\vec{k}, \xi_{r1})B_{r2 \ t2})I_{01}\phi(\vec{l}, \xi_{t1}) (\Delta(r)\Delta(t)(2\pi)^6)^{-1} \\ T_{21} &= (-I_{01}\phi(\vec{k}, \xi_{r2})B_{r1 \ t1} + I_{01}\phi(\vec{k}, \xi_{r1})B_{r2 \ t1})I_{01}\phi(\vec{l}, \xi_{t2}) - \\ &\quad (-I_{01}\phi(\vec{k}, \xi_{r2})B_{r1 \ t2} + I_{01}\phi(\vec{k}, \xi_{r1})B_{r2 \ t2})I_{01}\phi(\vec{l}, \xi_{t1}) (\Delta(r)\Delta(t)(2\pi)^6)^{-1} \\ T_{22} &= (-I_{01}\phi(\vec{k}, \xi_{r2})B_{r1 \ t1} + I_{01}\phi(\vec{k}, \xi_{r1})B_{r2 \ t1})I_{01}\phi(\vec{l}, \xi_{t2}) + \\ &\quad (-I_{01}\phi(\vec{k}, \xi_{r2})B_{r1 \ t2} + I_{01}\phi(\vec{k}, \xi_{r1})B_{r2 \ t2})I_{01}\phi(\vec{l}, \xi_{t1}) (\Delta(r)\Delta(t)(2\pi)^6)^{-1} \end{aligned}$$

The T_{ij} components of $T_{11}(\vec{k}, \vec{l})$, for particular values of $(K_{xt}, K_{yt}, L_{xt}, L_{yt})$, are the transfer function that maps incident θ, ϕ polarizations into scattered (emerging) θ, ϕ polarizations.

We now show the equivalence of the scattering matrix as derived above and the matrix representation derived in Chapter II. We first derive the explicit solution for the scattering matrix $T_{11}(\vec{K}, \vec{L})$ in terms of the measured data array. The bistatic measurement equation is

$$b_0(\vec{r}_1, \vec{r}_2) = \underbrace{\iint \vec{I}_{01}^t(\vec{k}) \cdot \left[\iint \vec{T}_{11}(\vec{k}, \vec{l}) \cdot \vec{I}_{10}(\vec{l}) e^{-i\vec{l} \cdot \vec{r}_1} d\vec{l} \right] e^{+i\vec{k} \cdot \vec{r}_2} d\vec{k}}_{D(\vec{k}, \vec{r}_1)}$$

where the equation elements are as defined in the preceding sections and $D(\vec{k}, \vec{r}_1)$ is a scalar coupling product.

In the laboratory we measure a multidimensional scalar complex array $b_0(P_{xr}, P_{yr}, P_{zr}, P_{xt}, P_{yt}, P_{zt}, \xi_r, \xi_t)$ at discrete points

$$(P_{xr}, P_{yr}, P_{zr}) \in \{(P_{xr_i}, P_{yr_i}, P_{zr})\}, P_{zr} = \text{constant},$$

$$(P_{xt}, P_{yt}, P_{zt}) \in \{(P_{xt_i}, P_{yt_i}, P_{zt})\}, P_{zt} = \text{constant},$$

$\xi_r = \{1, 2\} \equiv$ an index denoting receive probe orientation, and

$\xi_t = \{1, 2\} \equiv$ an index denoting transmit probe orientation.

In the first step of the solution, the scalar coupling product $D(\cdot)$ is computed as a phase-shifted two-dimensional Fourier transform of $B(\cdot)$ with respect to the transmitter coordinate \vec{r}_2 :

$$\int b_0(\vec{r}_1, \vec{r}_2) e^{-i\vec{m} \cdot \vec{r}_2} d\vec{r}_2 = \iint \vec{I}_{01}^t(\vec{k}) \cdot \left[\vec{T}_{11}(\vec{k}, \vec{l}) \cdot \vec{I}_{10}(\vec{l}) e^{-i\vec{l} \cdot \vec{r}_1} d\vec{l} \right] e^{i(\vec{k} - \vec{m}) \cdot \vec{r}_2} d\vec{k}$$

which we write as

$$D(\vec{m}, \vec{r}_1) = \int \vec{I}_{01}^t(\vec{k}) \cdot \left[\vec{T}_{11}(\vec{k}, \vec{l}) \cdot \vec{I}_{10}(\vec{l}) e^{-i\vec{l} \cdot \vec{r}_1} d\vec{l} \right] (2\pi)^2 \delta(\vec{k} - \vec{m}) d\vec{k}$$

$$D(\vec{k}, \vec{r}_1) = (2\pi)^2 \vec{I}_{01}^t(\vec{k}) \cdot \left[\vec{T}_{11}(\vec{k}, \vec{l}) \cdot \vec{I}_{10}(\vec{l}) e^{-i\vec{l} \cdot \vec{r}_1} d\vec{l} \right]$$

$D(\vec{k}, \vec{r}_1)$ is now written as a matrix to reflect its multi-component structure.

In our laboratory measurements the data components $b_0(\vec{r}_1, \vec{r}_2)$ are built up as a concatenation of scans by the receive probe; during each scan we vary P_{xr} and P_{yr} and hold P_{zr} , P_{xt} , P_{yt} , ξ_r , and ξ_t constant. Each $D(\vec{k}, \vec{r}_1)$ component consists of four complex scalar corresponding to the combinations of $\xi_r = \{1, 2\}$ and $\xi_t = \{1, 2\}$.

In the second step of the solution, the scattered spectrum

$$F(\vec{k}, \vec{r}_1) = \int \bar{T}_{11}(\vec{k}, \vec{l}) \cdot \vec{l}_{10}(\vec{l}) e^{-i\vec{l} \cdot \vec{r}_1} d\vec{l}.$$

is computed from $D(\vec{k}, \vec{r}_1)$ and the receive probe response function $I_{01}(\cdot)$ by means of a simultaneous linear equation solution. From a prior equation $D(\vec{k}, \vec{r}_2)$ is

$$D(\vec{k}, \vec{r}_1) = (2\pi)^2 I_{01}^t(\vec{k}) \cdot \bar{F}(\vec{k}, \vec{r}_1).$$

Expanding explicitly,

$$D(\vec{k}, \vec{r}_1, \xi_r, \xi_t) = I_{01\theta}(\vec{k}, \xi_r) F_{\theta}(\vec{k}, \vec{r}_1, \xi_t) + I_{01\phi}(\vec{k}, \xi_r) F_{\phi}(\vec{k}, \vec{r}_1, \xi_t).$$

To solve for $F(\cdot)$ we need two equations obtained by measuring $D(\cdot)$ at two different ξ_r :

$$D(\vec{k}, \vec{r}_1, \xi_{r1}, \xi_t) = I_{01\theta}(\vec{k}, \xi_{r1}) F_{\theta}(\vec{k}, \vec{r}_1, \xi_t) + I_{01\phi}(\vec{k}, \xi_{r1}) F_{\phi}(\vec{k}, \vec{r}_1, \xi_t)$$

$$D(\vec{k}, \vec{r}_1, \xi_{r2}, \xi_t) = I_{01\theta}(\vec{k}, \xi_{r2}) F_{\theta}(\vec{k}, \vec{r}_1, \xi_t) + I_{01\phi}(\vec{k}, \xi_{r2}) F_{\phi}(\vec{k}, \vec{r}_1, \xi_t).$$

Then

$$F_{\theta}(\vec{k}, \vec{r}_1, \xi_t) = [D(\vec{k}, \vec{r}_1, \xi_{r1}, \xi_t) I_{01\phi}(\vec{k}, \xi_{r2}) - D(\vec{k}, \vec{r}_1, \xi_{r2}, \xi_t) I_{01\theta}(\vec{k}, \xi_{r1})] \Delta(r)^{-1}$$

$$F_{\phi}(\vec{k}, \vec{r}_1, \xi_t) = [D(\vec{k}, \vec{r}_1, \xi_{r1}, \xi_t) I_{01\theta}(\vec{k}, \xi_{r2}) - D(\vec{k}, \vec{r}_1, \xi_{r2}, \xi_t) I_{01\phi}(\vec{k}, \xi_{r1})] \Delta(r)^{-1}$$

with non-zero determinant

$$\Delta(r) \equiv I_{01\theta}(\vec{k}, \xi_{r1}) I_{01\phi}(\vec{k}, \xi_{r2}) - I_{01\theta}(\vec{k}, \xi_{r2}) I_{01\phi}(\vec{k}, \xi_{r1}).$$

For each transmit probe position (P_{xt}, P_{yt}, P_{zt}) and orientation ξ_t , $F(\cdot)$ is defined over all valid \vec{k} . Note that $F(\cdot)$ is not a function of ξ_r . A particular realization $F(\cdot)$ is the scattered spectrum from the object, given a particular position \vec{r}_1 and orientation ξ_t of the transmit probe.

In the third step the vector coupling product is calculated as a two-dimensional phase-shifted Fourier transform with respect to the transmit probe coordinates. From a prior equation

$$F(\vec{k}, \vec{r}_1) = \int \bar{T}_{11}(\vec{k}, \vec{l}) \cdot \vec{l}_{10}(\vec{l}) e^{-i\vec{l} \cdot \vec{r}_1} d\vec{l}$$

we define

$$Q(\vec{k}, \vec{l}) = \bar{T}_{11}(\vec{k}, \vec{l}) \cdot \vec{l}_{10}(\vec{l}).$$

and write

$$F(\vec{k}, \vec{r}_1) = \int Q(\vec{k}, \vec{l}) \cdot e^{-i\vec{l} \cdot \vec{r}_1} d\vec{l}.$$

The equation is now Fourier transformed with respect to \vec{r}_1

$$\int F(\vec{k}, \vec{r}_1) \cdot e^{-i\vec{n} \cdot \vec{r}_1} d\vec{r}_1 = \iint Q(\vec{k}, \vec{l}) \cdot e^{-i(\vec{l} + \vec{n}) \cdot \vec{r}_1} d\vec{l} d\vec{r}_1.$$

$$F(\vec{k}, \vec{n}) = (2\pi)^2 \int Q(\vec{k}, \vec{l}) \cdot d\vec{l} \delta(\vec{l} + \vec{n})$$

$$F(\vec{k}, \vec{l}) = (2\pi)^2 Q(\vec{k}, -\vec{l})$$

This vector coupling product represents the θ, ϕ components of the scattered spectrum as a function of incident \vec{l} , emerging \vec{k} , and transmit probe orientation ξ_t .

The fourth and final step is to calculate the scattering matrix $\bar{T}_{11}(\vec{k}, \vec{l})$. The equation

$$Q(\vec{k}, \vec{r}_1) = \bar{T}_{11}(\vec{k}, \vec{l}) \cdot \vec{l}_{10}(\vec{l})$$

can be written explicitly in terms of the respective ξ_t terms as

$$\begin{bmatrix} Q_\theta(\vec{k}, \vec{r}_1, \xi_{t1}) & Q_\theta(\vec{k}, \vec{r}_1, \xi_{t2}) \\ Q_\phi(\vec{k}, \vec{r}_1, \xi_{t1}) & Q_\phi(\vec{k}, \vec{r}_1, \xi_{t2}) \end{bmatrix} = \begin{bmatrix} T_{11\theta\theta}(\vec{l}, \xi_{t1}) & T_{11\theta\phi}(\vec{l}, \xi_{t2}) \\ T_{11\phi\theta}(\vec{l}, \xi_{t1}) & T_{11\phi\phi}(\vec{l}, \xi_{t2}) \end{bmatrix} \cdot \begin{bmatrix} I_{10\theta}(\vec{k}, \vec{l}, \xi_{t1}) & I_{10\theta}(\vec{k}, \vec{l}, \xi_{t2}) \\ I_{10\phi}(\vec{k}, \vec{l}, \xi_{t1}) & I_{10\phi}(\vec{k}, \vec{l}, \xi_{t2}) \end{bmatrix}$$

Solving for $\bar{T}_{11}(\vec{k}, \vec{l})$ we write

$$\bar{T}_{11}(\vec{k}, \vec{l}) = Q(\vec{k}, \vec{r}_1, \xi_t) \cdot I_{10}(\vec{l}, \xi_t)^{-1}$$

where

$$I_{10}(\vec{l}, \xi_t)^{-1} = \begin{bmatrix} I_{10\phi}(\vec{k}, \vec{l}, \xi_{t2}) & -I_{10\theta}(\vec{k}, \vec{l}, \xi_{t2}) \\ -I_{10\phi}(\vec{k}, \vec{l}, \xi_{t1}) & I_{10\theta}(\vec{k}, \vec{l}, \xi_{t1}) \end{bmatrix} \Delta(t)^{-1}$$

with non-zero determinant

$$\Delta(t) \equiv I_{10\theta}(\vec{k}, \vec{l}, \xi_{t1}) I_{10\phi}(\vec{l}, \xi_{t2}) - I_{10\theta}(\vec{l}, \xi_{t2}) I_{10\phi}(\vec{l}, \xi_{t1})$$

which results in

$$\begin{bmatrix} Q_{\theta}(\vec{k}, \vec{r}_1, \epsilon_{t1}) & Q_{\theta}(\vec{k}, \vec{r}_1, \epsilon_{t2}) \\ Q_{\phi}(\vec{k}, \vec{r}_1, \epsilon_{t1}) & Q_{\phi}(\vec{k}, \vec{r}_1, \epsilon_{t2}) \end{bmatrix} \begin{bmatrix} I_{10\phi}(\vec{k}, \vec{l}, \epsilon_{t2}) & -I_{10\theta}(\vec{k}, \vec{l}, \epsilon_{t2}) \\ -I_{10\phi}(\vec{k}, \vec{l}, \epsilon_{t1}) & I_{10\theta}(\vec{k}, \vec{l}, \epsilon_{t1}) \end{bmatrix} \Delta(t)^{-1}.$$

We can now write the components of $\bar{T}_{11}(\vec{k}, \vec{l})$ as

$$T_{11\theta\theta}(\vec{k}, \vec{l}) = \frac{Q_{\theta}(\vec{k}, \vec{l}, \epsilon_{t1}) I_{10\phi}(\vec{l}, \epsilon_{t2}) - Q_{\theta}(\vec{k}, \vec{l}, \epsilon_{t2}) I_{10\phi}(\vec{l}, \epsilon_{t1})}{\Delta(t)}$$

$$T_{11\theta\phi}(\vec{k}, \vec{l}) = \frac{Q_{\phi}(\vec{k}, \vec{l}, \epsilon_{t1}) I_{10\phi}(\vec{l}, \epsilon_{t2}) - Q_{\phi}(\vec{k}, \vec{l}, \epsilon_{t2}) I_{10\phi}(\vec{l}, \epsilon_{t1})}{\Delta(t)}$$

$$T_{11\phi\theta}(\vec{k}, \vec{l}) = \frac{-Q_{\theta}(\vec{k}, \vec{l}, \epsilon_{t1}) I_{10\theta}(\vec{l}, \epsilon_{t2}) + Q_{\theta}(\vec{k}, \vec{l}, \epsilon_{t2}) I_{10\theta}(\vec{l}, \epsilon_{t1})}{\Delta(t)}$$

$$T_{11\phi\phi}(\vec{k}, \vec{l}) = \frac{-Q_{\phi}(\vec{k}, \vec{l}, \epsilon_{t1}) I_{10\theta}(\vec{l}, \epsilon_{t2}) + Q_{\phi}(\vec{k}, \vec{l}, \epsilon_{t2}) I_{10\theta}(\vec{l}, \epsilon_{t1})}{\Delta(t)}.$$

The four components of $\bar{T}_{11}(\vec{k}, \vec{l})$, for particular values of (\vec{k}, \vec{l}) , are the transfer function that maps incident θ, ϕ polarizations into scattered (emerging) θ, ϕ polarizations.

To compare the vector and above formulations of the scattering equations, it is necessary to substitute for the respective \bar{Q} , \bar{F} and \bar{D} matrices to show the equation in terms of the measured \bar{B} data set.

We have, from a preceding section,

$$\bar{F}(\vec{k}, \vec{l}) = (2\pi)^2 \bar{Q}(\vec{k}, -\vec{l}).$$

We use a previously defined equation relating \bar{D} and \bar{F} to write the \bar{T} components in terms of the \bar{D} and \bar{I} matrices, i.e.,

$$\bar{D}(\vec{k}, \vec{r}_1) = (2\pi)^2 \bar{I}_{01}^t(\vec{k}) \cdot \bar{F}(\vec{k}, \vec{r}_1).$$

The Fourier transform with respect to \vec{r}_1 and the wavenumber argument \vec{l} is

$$\bar{D}(\vec{k}, \vec{l}) = (2\pi)^2 \bar{I}_{01}^t(\vec{k}) \cdot \bar{F}(\vec{k}, \vec{l}).$$

Thus, we obtain

$$\bar{D}(\vec{k}, \vec{l}) = ((2\pi)^4 \bar{I}_{01}^t(\vec{k})) \cdot \bar{Q}(\vec{k}, -\vec{l}).$$

Recall that $\bar{B}_0(\vec{r}_1, \vec{r}_2)$ is defined in terms of $\bar{D}(\vec{k}, \vec{r}_1)$ as

$$\bar{B}_0(\vec{r}_1, \vec{r}_2) = \int \bar{D}(\vec{k}, \vec{r}_1) e^{-i\vec{k} \cdot \vec{r}_2} d\vec{k}.$$

Taking the Fourier transform of both sides with respect to \vec{r}_1 and \vec{r}_2 we have

$$\iint \bar{v}_0(\vec{r}_1, \vec{r}_2) e^{-i\vec{m} \cdot \vec{r}_1 - i\vec{n} \cdot \vec{r}_2} d\vec{r}_1 d\vec{r}_2 = \\ \iiint \bar{v}(\vec{k}, \vec{r}_1) e^{-i\vec{k} \cdot \vec{r}_2 - i\vec{m} \cdot \vec{r}_1 - i\vec{n} \cdot \vec{r}_2} d\vec{k} d\vec{r}_1 d\vec{r}_2.$$

The results of the transform operations yield

$$\bar{B}(\vec{m}, \vec{n}) = \iint \bar{v}(\vec{k}, \vec{r}_1) \cdot e^{-i\vec{m} \cdot \vec{r}_1} d\vec{k} d\vec{r}_1 \cdot (2\pi)^2 \cdot \delta(\vec{k} + \vec{n})$$

or

$$\bar{B}_0(\vec{k}, \vec{l}) = (2\pi)^2 \cdot \bar{v}(\vec{k}, -\vec{l}).$$

Using the equation for \bar{v} determined earlier, we now have

$$\bar{B}(\vec{k}, \vec{l}) = (2\pi)^6 \cdot \bar{I}_{01}^t(\vec{k}) \cdot \bar{Q}(\vec{k}, \vec{l}).$$

We can now write the components of $\bar{I}_{11}^t(\vec{k}, \vec{l})$ in terms of the \bar{B} components as

$$\bar{Q}(\vec{k}, \vec{l}) = \bar{I}_{01}^t(\vec{k})^{-1} \cdot \bar{B}(\vec{k}, \vec{l}) / (2\pi)^6.$$

The \bar{I} and \bar{B} elements of \bar{Q} are

$$\bar{I}_{01}^t(\vec{k})^{-1} = \begin{bmatrix} I_{01\phi}(k, \xi_{r2}) & -I_{01\phi}(k, \xi_{r1}) \\ -I_{01\phi}(k, \xi_{r2}) & I_{01\phi}(k, \xi_{r1}) \end{bmatrix} \Delta(r)^{-1}$$

where $\Delta(r)$ is

$$\Delta(r) = I_{01\phi}(k, \xi_{r1}) \cdot I_{01\phi}(k, \xi_{r2}) - I_{01\phi}(k, \xi_{r1}) \cdot I_{01\phi}(k, \xi_{r2})$$

and

$$\bar{B}(\vec{k}, \vec{l}) = \begin{bmatrix} B_{11} t_1 & B_{r1} t_2 \\ B_{r2} t_1 & B_{r2} t_2 \end{bmatrix}.$$

We can now write $\bar{Q}(\vec{k}, \vec{l})$ as

$$\bar{Q}(\vec{k}, \vec{l}) = \begin{bmatrix} Q_{\theta}(\vec{k}, \vec{r}_1, \xi_{t1}) & Q_{\theta}(\vec{k}, \vec{r}_1, \xi_{t2}) \\ Q_{\phi}(\vec{k}, \vec{r}_1, \xi_{t1}) & Q_{\phi}(\vec{k}, \vec{r}_1, \xi_{t2}) \end{bmatrix} \approx$$

$$\begin{bmatrix} (I_{01\phi}(k, \xi_{r2})B_{r1 t1} - I_{01\phi}(k, \xi_{r1})B_{r2 t1}) & (I_{01\phi}(k, \xi_{r2})B_{r1 t2} - I_{01\phi}(k, \xi_{r1})B_{r2 t2}) \\ (-I_{01\phi}(\tilde{k}, \xi_{r2})B_{r1 t1} + I_{01\phi}(\tilde{k}, \xi_{r1})B_{r2 t1}) & (-I_{01\phi}(\tilde{k}, \xi_{r2})B_{r1 t2} + I_{01\phi}(\tilde{k}, \xi_{r1})B_{r2 t2}) \end{bmatrix}$$

$$\times ((2\pi)^6 \Delta(r))^{-1}.$$

We can now write the components of $\bar{T}_{11}(\tilde{k}, \tilde{I})$ as

$$\begin{aligned} T_{11\theta\theta}(\tilde{k}, \tilde{I}) &= \frac{Q_{\theta}(\tilde{k}, \tilde{I}, \xi_{t1})I_{10\phi}(\tilde{I}, \xi_{t2}) - Q_{\theta}(\tilde{k}, \tilde{I}, \xi_{t2})I_{10\phi}(\tilde{I}, \xi_{t1})}{\Delta(t)} \\ T_{11\theta\phi}(\tilde{k}, \tilde{I}) &= \frac{Q_{\phi}(\tilde{k}, \tilde{I}, \xi_{t1})I_{10\phi}(\tilde{I}, \xi_{t2}) - Q_{\phi}(\tilde{k}, \tilde{I}, \xi_{t2})I_{10\phi}(\tilde{I}, \xi_{t1})}{\Delta(t)} \\ T_{11\phi\theta}(\tilde{k}, \tilde{I}) &= \frac{-Q_{\theta}(\tilde{k}, \tilde{I}, \xi_{t1})I_{10\phi}(\tilde{I}, \xi_{t2}) + Q_{\theta}(\tilde{k}, \tilde{I}, \xi_{t2})I_{10\phi}(\tilde{I}, \xi_{t1})}{\Delta(t)} \\ T_{11\phi\phi}(\tilde{k}, \tilde{I}) &= \frac{-Q_{\phi}(\tilde{k}, \tilde{I}, \xi_{t1})I_{10\phi}(\tilde{I}, \xi_{t2}) + Q_{\phi}(\tilde{k}, \tilde{I}, \xi_{t2})I_{10\phi}(\tilde{I}, \xi_{t1})}{\Delta(t)} \end{aligned}$$

When the values for the Q elements are substituted into the equations for the T elements we see that the scattering matrix values are identical to those derived earlier. Thus, the representation we will use for computing the scattering matrix is

$$\bar{T}_{11}(\tilde{k}, \tilde{I}) = (TK)^{-1} \cdot B(\tilde{k}, \tilde{I}) \cdot (IL)^{-1} / (2\pi)^6$$

where

$$(TK)^{-1} = \begin{bmatrix} I_{01\phi}(k, \xi_{r2}) & -I_{01\phi}(k, \xi_{r1}) \\ -I_{01\phi}(\tilde{k}, \xi_{r2}) & I_{01\phi}(\tilde{k}, \xi_{r1}) \end{bmatrix} / \Delta(r)$$

$$(IL)^{-1} = \begin{bmatrix} I_{01\phi}(\tilde{I}, \xi_{t2}) & -I_{01\phi}(\tilde{I}, \xi_{t1}) \\ -I_{01\phi}(\tilde{I}, \xi_{t1}) & I_{01\phi}(\tilde{I}, \xi_{t2}) \end{bmatrix} / \Delta(t)$$

$$\Delta(r) = I_{01\phi}(\tilde{k}, \xi_{r1}) I_{01\phi}(\tilde{k}, \xi_{r2}) - I_{01\phi}(\tilde{k}, \xi_{r2}) I_{01\phi}(\tilde{k}, \xi_{r1})$$

$$\Delta(t) = I_{01\phi}(\tilde{I}, \xi_{t1}) I_{01\phi}(\tilde{I}, \xi_{t2}) - I_{01\phi}(\tilde{I}, \xi_{t2}) I_{01\phi}(\tilde{I}, \xi_{t1})$$

and

$$B = \begin{bmatrix} B_{r1 t1} & B_{r1 t2} \\ B_{r2 t1} & B_{r2 t2} \end{bmatrix}.$$

C. FUNCTIONAL EXPANSION

We consider here a method for reducing the computational and storage burden of the near-field computations. The basis for the method is a representation of the measured data field by a suitable expansion function which is truncated to limit the number of field function derivatives (to yield a relatively "smooth" estimate of the scattering matrix) and which minimizes some specified error function of the estimated scattering matrix. The equations are written in terms of the previously determined values, $\bar{T}_{11}(\vec{k}, \vec{l})$, of the scattering matrix and the next value, $\bar{T}_{11}(\vec{k} + \Delta\vec{k}, \vec{l} + \Delta\vec{l})$, of the scattering matrix to be determined. As an example, we will consider an estimate for the scattering matrix which minimizes the norm, $N(d)$, of the equation defining the scattering matrix, i.e.

$$N(d) = | \bar{T}_{11}(\vec{k}, \vec{l}) - (IK)^{-1} \cdot E \cdot (EL)^{-1} / (2\pi)^6 |_{\text{norm}}$$

The specific matrix normalization which might be used need not be specified at this time for the purposes of this example. The minimization is subject to the constraint that in the region of each set of estimated values, the scattering matrix has no derivatives above the second order. Therefore

$$\bar{T}_{11}(\vec{k} + \Delta\vec{k}, \vec{l} + \Delta\vec{l}) = \sum_{n=0}^2 [\nabla_{\vec{k}} \cdot \Delta\vec{k} \partial/\partial\vec{k} + \nabla_{\vec{l}} \cdot \Delta\vec{l} \partial/\partial\vec{l}]^{(n)} \bar{T}_{11}(\vec{k}, \vec{l})$$

where $\nabla_{\vec{k}}$ and $\nabla_{\vec{l}}$ are the gradients of the function $\bar{T}_{11}(\vec{k}, \vec{l})$ with respect to \vec{k} and \vec{l} and $[\cdot]^{(n)}$ represents the gradient and partial differential operators in the bracketed quantity being raised to the nth power before operating on the process functions. The minimization and constraint conditions are combined using a LaGrange multiplier as shown below:

$$Q = N(d) + \lambda | (\bar{T}_{11}(\vec{k} + \Delta\vec{k}, \vec{l} + \Delta\vec{l}) - \sum_{n=0}^2 [\nabla_{\vec{k}} \cdot \Delta\vec{k} \partial/\partial\vec{k} + \nabla_{\vec{l}} \cdot \Delta\vec{l} \partial/\partial\vec{l}]^{(n)} \bar{T}_{11}(\vec{k}, \vec{l})) |_{\text{norm}}$$

The equation for Q is now minimized with respect to λ and also $\bar{T}_{11}(\vec{k}, \vec{l})$ for given values of $\Delta\vec{k}$ and $\Delta\vec{l}$ in order to compute $\bar{T}_{11}(\vec{k} + \Delta\vec{k}, \vec{l} + \Delta\vec{l})$. The intent of the operations is to solve for consecutive values of $\bar{T}_{11}(\vec{k} + \Delta\vec{k}, \vec{l} + \Delta\vec{l})$ for spacings of $\Delta\vec{k}$ and $\Delta\vec{l}$ which are greater than those which might be required if the process constraints were not applied. If the resultant spacings of $\Delta\vec{k}$ and $\Delta\vec{l}$ are greater than those that would be required based on

the effective aperture of the scattering object, then we will have reduced the density of data sampling for the near-field measurements.

The equations must next be written in terms of the measurement parameters $(IK(\vec{k}))^{-1}$, $(\Pi(\vec{l}))^{-1}$ and $(2\pi)^6$ and the data variable $B(\vec{k}, \vec{l})$.

The expansion terms in the constraint equation are next written as

$$\sum_{n=0}^2 [\nabla_{\vec{k}} \cdot \Delta \vec{k} \partial / \partial \vec{k} + \nabla_{\vec{l}} \cdot \Delta \vec{l} \partial / \partial \vec{l}]^{(n)} \bar{T}_{11}(\vec{k}, \vec{l}) = \sum_{n=0}^2 [\nabla_{\vec{k}} \cdot \Delta \vec{k} \partial / \partial \vec{k} + \nabla_{\vec{l}} \cdot \Delta \vec{l} \partial / \partial \vec{l}]^{(n)} (IK(\vec{k}))^{-1} \cdot B(\vec{k}, \vec{l}) \cdot (\Pi(\vec{l}))^{-1} / (2\pi)^6.$$

The expansion for $n=0$ yields

$$(IK(\vec{k}))^{-1} \cdot B(\vec{k}, \vec{l}) \cdot (\Pi(\vec{l}))^{-1} / (2\pi)^6.$$

The expansion for $n=1$ yields

$$\begin{aligned} & [\nabla_{\vec{k}} \cdot \Delta \vec{k} \partial / \partial \vec{k} + \nabla_{\vec{l}} \cdot \Delta \vec{l} \partial / \partial \vec{l}]^{(1)} (IK(\vec{k}))^{-1} \cdot B(\vec{k}, \vec{l}) \cdot (\Pi(\vec{l}))^{-1} / (2\pi)^6 = \\ & [(-1)IK(\vec{k})^{-1} \cdot (\nabla_{\vec{k}} \cdot \Delta \vec{k} \partial / \partial \vec{k}) IK(\vec{k}) \cdot IK(\vec{k})^{-1} \cdot B(\vec{k}, \vec{l}) \cdot (\Pi(\vec{l}))^{-1} + \\ & IK(\vec{k})^{-1} \cdot (\nabla_{\vec{k}} \cdot \Delta \vec{k} \partial / \partial \vec{k}) B(\vec{k}, \vec{l}) \cdot (\Pi(\vec{l}))^{-1} + \\ & IK(\vec{k})^{-1} \cdot (\nabla_{\vec{l}} \cdot \Delta \vec{l} \partial / \partial \vec{l}) B(\vec{k}, \vec{l}) \cdot (\Pi(\vec{l}))^{-1} + \\ & IK(\vec{k})^{-1} \cdot B(\vec{k}, \vec{l}) \cdot (-1)(\Pi(\vec{l}))^{-1} \cdot (\nabla_{\vec{l}} \cdot \Delta \vec{l} \partial / \partial \vec{l}) (\Pi(\vec{l})) \cdot (\Pi(\vec{l}))^{-1}] / (2\pi)^6. \end{aligned}$$

The expansion for $n=2$ yields

$$\begin{aligned} & [\nabla_{\vec{k}} \cdot \Delta \vec{k} \partial / \partial \vec{k} + \nabla_{\vec{l}} \cdot \Delta \vec{l} \partial / \partial \vec{l}]^{(2)} (IK(\vec{k}))^{-1} \cdot B(\vec{k}, \vec{l}) \cdot (\Pi(\vec{l}))^{-1} / (2\pi)^6 = \\ & [\nabla_{\vec{k}}^2 \cdot \Delta \vec{k} \partial^2 / \partial \vec{k}^2 + 2 \cdot \nabla_{\vec{k}} \cdot \Delta \vec{k} \nabla_{\vec{l}} \cdot \Delta \vec{l} \partial^2 / \partial \vec{k} \partial \vec{l} + \nabla_{\vec{l}}^2 \cdot \Delta \vec{l} \partial^2 / \partial \vec{l}^2] \cdot \\ & (IK(\vec{k}))^{-1} \cdot B(\vec{k}, \vec{l}) \cdot (\Pi(\vec{l}))^{-1} / (2\pi)^6. \end{aligned}$$

Rather than complete the expansion for the second order terms, it is helpful to consider the implications of the expansion terms relative to reducing the sampling density of measurements while providing a satisfactory estimate of the scattering matrix. For example, we might examine the computational and sampling implications of using a measurement process which assured that the $\partial^2 IK(\vec{k}) / \partial^2 \vec{k}$ and $\partial^2 IK(\vec{l}) / \partial \vec{l}$ terms would be zero.

The final steps are to perform the minimization with respect to λ and the components of $(IK(\vec{k}))^{-1} \cdot B(\vec{k}, \vec{l}) \cdot (\Pi(\vec{l}))^{-1}$ in the expansion equations and solve for

$\bar{T}_{11}(\vec{k}+\Delta\vec{k}, \vec{l}+\Delta\vec{l})$. The estimated value for $\bar{T}_{11}(\vec{k}+\Delta\vec{k}, \vec{l}+\Delta\vec{l})$ is then compared with the measured value of $\bar{T}_{11}(\vec{k}+\Delta\vec{k}, \vec{l}+\Delta\vec{l})$. If the difference between the two values exceeds a specified tolerance value, we have several alternatives depending on the region over which the function minimization was performed. If the region is local, the required spacings of the data samples can be determined adaptively and changed as required at each measurement location. If the minimization region is global then the local error estimates can be used as a basis for changing the constraint conditions of the algorithm.

CHAPTER VII

DEFINITION OF MEASUREMENT LIMITATIONS

A. INTRODUCTION

The purpose of this task was to investigate the limitations, both theoretical and experimental, of the near-field RCS measurement method. We concentrated on two topics: (1) data acquisition limitations and (2) measurement of wide-angle bistatic RCS. Investigation into the data acquisition limitations considered the design of the receiver, the antenna configuration, and the storage requirements. The investigation into wide-angle bistatic RCS concentrated on the difficulties of performing such a measurement.

Results of this investigation are that, depending upon the frequency of interest, near-field RCS is practical with current technology for objects ranging in size from small missiles to B-1 Bombers for monostatic RCS and small-angle bistatic RCS. For wide-angle bistatic RCS, we concluded that new technology and/or modified near-field theory is needed. Additionally, application of near-field RCS for large objects at frequencies above 1 gigahertz is dependent upon the development of large array antennas appropriate for near-field.

B. DATA ACQUISITION LIMITATIONS

Investigations into the data acquisition limitations covered the topics of receiver design, antenna requirements, and data storage requirements. This investigation demonstrates that near-field RCS is possible for a wide class of problems with current technology and that, with the advancement of new technology, it has the potential to be applicable for many classes of RCS measurement configurations. In this section, only monostatic and small-angle bistatic RCS is considered.

1. Receiver Design

A potential design for the receiver in the near-field measurement method is shown in Figure VII-1. The receiver shown is a synchronous detector and is similar to receivers used on typical radar systems. This type of receiver is proposed because of its

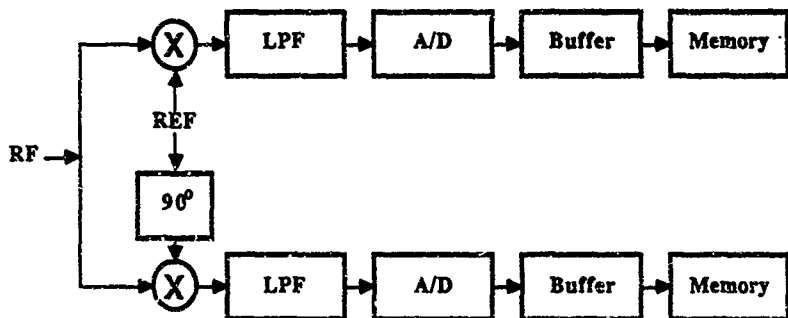


Figure VII-1. Synchronous Detector Receiver Design

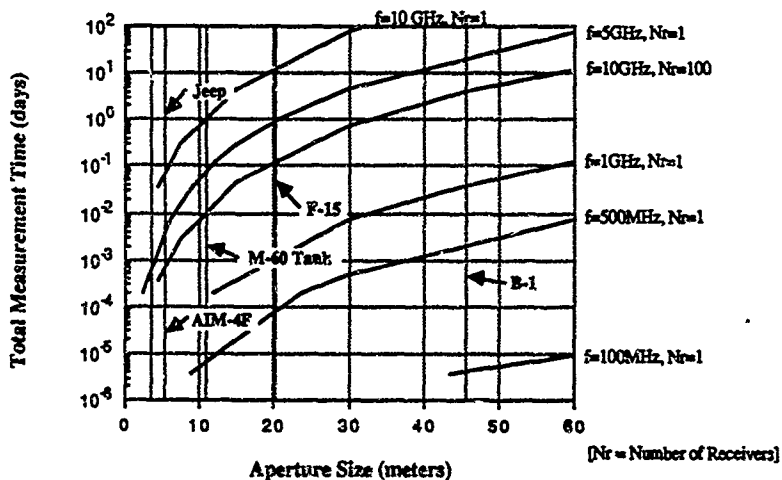


Figure VII-2. Near-field Measurement Times For Fixed Aperture Antennas

ability to rapidly measure the real and imaginary parts of the received signal. The real part of the RF signal is obtained by multiplying the RF signal by a reference signal from the local oscillator and low-pass filtering the result. The imaginary part is obtained by multiplying the RF signal by the quadrature of the reference signal and filtering as before. These signals are then converted to digital form and stored.

In most cases, data storage will be the slowest function in the receiver. However, if a buffer is devised to switch between several storage devices, one could realize a system which is limited by the A/D conversion and the settling time of the low-pass filter. In most practical cases, the A/D conversion time will be the limiting factor on speed if one is willing to use a wide-band low-pass filter and accept the increased noise that will be associated with the wide bandwidth. Conversion times of under one microsecond for 12 bit A/D conversion are common.

Figure VII-2 shows the measurement time required to make near-field RCS measurements assuming that the only limitation is the sampling time for the A/D conversion. In this example an array antenna with $\lambda/2$ spacing is used, the A/D conversion time is 0.1 microsecond, and the time to move the transmit probe is assumed negligible. This graph shows that for practical frequencies and for targets as large as the B-1 bomber, A/D conversion times are not a limitation with near-field measurements given enough receivers. The main limitation of this configuration, however, is the design of the array antenna and receiver system, and the cost of such a system. Arrays with 10^6 to 10^7 array elements and 10^2 to 10^3 receivers will be required at higher frequencies.

2. Data Storage

Data storage requirements are extremely large for many practical measurement configurations. Figure VII-3 shows the data volume generated assuming conventional sampling techniques and no data compression. The large amounts of data that must be stored required some kind of data compression to make near-field RCS practical for large scattering objects at high frequencies. Several techniques for reducing

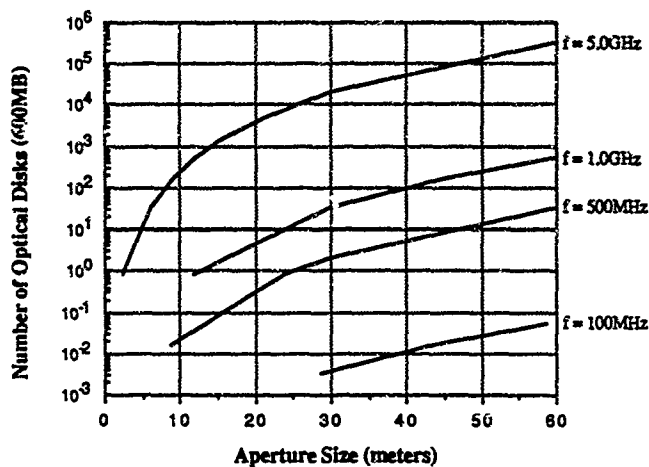


Figure VII-3. Data Storage Requirements

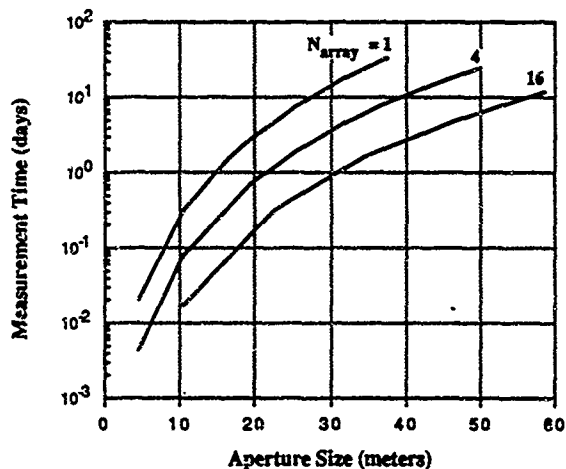


Figure VII-4. Near-field Measurement Times at 100 MHz

the volume of data are discussed in Chapter VI. Even without data compression, however, it appears feasible to measure objects ranging from a jeep at 5 Ghz to a B-1 Bomber at 100 Mhz.

3. Existing Technology

In the previous section it was shown that near-field measurement times are reasonable given a suitably-designed array antenna and receiver system. This technology has not been demonstrated yet, and therefore near-field measurement times were investigated assuming implementations using existing technology.

From Figure VII-2, note that measurement times of weeks are needed for large scattering objects in the gigahertz frequency bands given an optimally designed antenna system. The only measurement speed limitation of that system was the A/D conversion time. Therefore, one can conclude that near-field RCS measurements of large objects will require multi-antenna arrays to achieve the necessary measurement speed.

Measurement times for near-field RCS were developed as a function of the number of probe antennas (or array elements), the frequency, and the aperture scan area. Current technology generally uses a waveguide probe antenna. Although this type of probe has limited application here due to its high scattering cross section, it may be usable as long as the total number of probes is relatively small (i.e., the total cross section of the probes must remain small). Figure VII-4 through VII-8 show the resulting measurement times at different frequencies for various size apertures. Table VII-1 shows the practical limitation on target size as a function of frequency using these probe scanning techniques. As shown in the table, many practical systems can be measured with current probe scanning techniques and an expensive array antenna system need not be developed for these cases.

C. WIDE-ANGLE BISTATIC RCS

The near-field theory developed by Dinallo requires that the probe-to-probe coupling of the transmitter and receiver be negligible. This can be accomplished either by

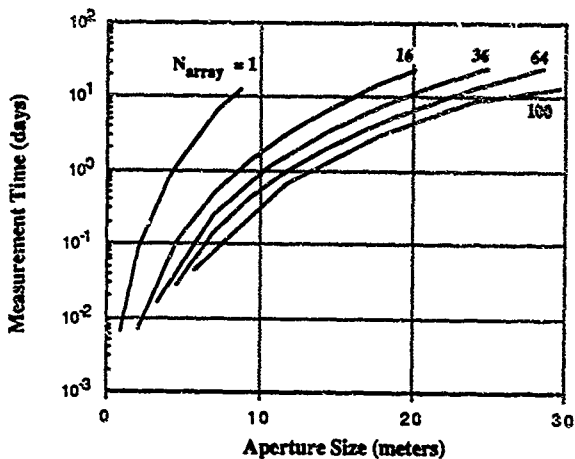


Figure VII-5. Near-field Measurement Times at 500 MHz

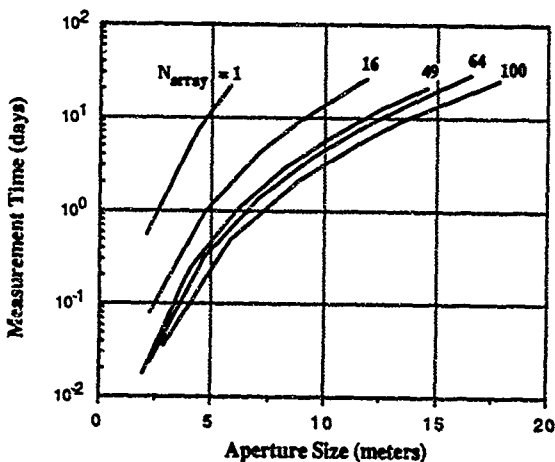


Figure VII-6. Near-field Measurement Times at 1 GHz

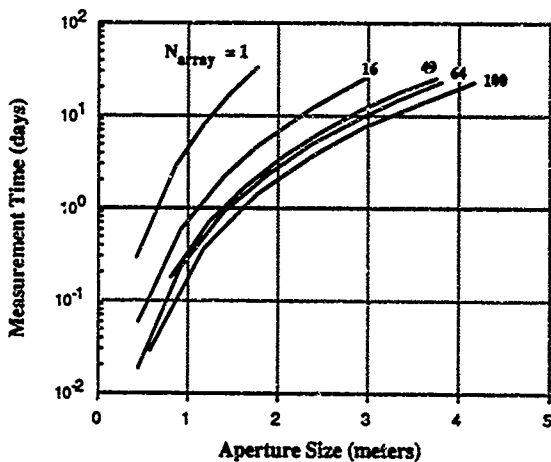


Figure VII-7. Near-field Measurement Times at 5 GHz

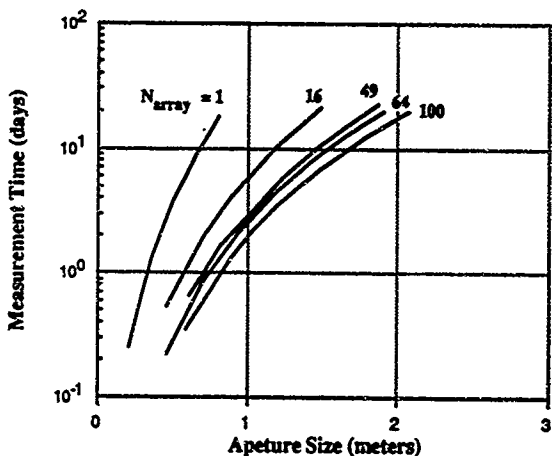


Figure VII-8. Near-field Measurement Times at 10 GHz

Table VII-1.

Practical Target Size Limitations Versus
Frequency Using Current Probe Scanning Techniques.

Frequency	Target
100 MHz	B-1 bomber
500 MHz	F-15 fighter
1 GHz	M60 tank
5 GHz	Jeep
10 GHz	< 2m diameter target

using probes with minimal mutual coupling or measurement techniques such as time gating, FM modulation of the background (range filtering), k-space filtering (angular filtering), and so forth. Each of these experimental techniques has its limitations. The problem that arises is that there will always be potential geometric orientations for which angular, range, or time filtering alone cannot distinguish between the received signals from the scatterer and the transmit probe antenna. This problem might be solved by using two or more of these techniques in tandem. Additional development of the theory of near-field RCS measurement may also be fruitful. Wide-angle bistatic RCS is conceptually feasible, but has yet to be demonstrated. Further investigation into using multiple filtering techniques and/or additional theoretical development need to be performed.

D. CONCLUSIONS

This brief investigation has shown that near-field monostatic and small-angle bistatic RCS measurements are practical for some interesting classes of problems using current technology. It also shows the need to develop both large array antenna systems and inexpensive multi-channel receivers. The need for array antennas, and thus multi-channel receiving, increases with increasing target size and frequency. Data storage problems also increase with increasing target size and frequency.

The data quantity reduction techniques discussed in Chapter V have the potential of relaxing the constraints for both the data storage and the complexity of the array antenna by requiring fewer data samples, and therefore requiring fewer array elements.

CHAPTER VIII

CONCLUSIONS

A. INTRODUCTION

This final report presents the technical work performed by BDM for the Rome Air Development Center to perform laboratory measurements and analysis to validate a planar near-field RCS measurement technique.

The major issues of the technical effort are discussed in the previous chapters of this report. The probe corrected near-field theory is well-developed and is directly applicable to the planar measurement configuration. Software to implement the theory has been developed. Near-field measurements were obtained with a low-cost computer-controlled scanning table designed and constructed in the BDM Laboratory. Agreement between measurements and predictions was excellent. We have identified several approaches to reducing the quantity of data required for near-field RCS measurements, and have identified some of the limitations of the method.

Although we do not see any fundamental obstacles to implementing this RCS measurement technique on a larger scale, our recent work has given us insight into the type of development needed to bring this concept to fruition. While building on the mature near-field antenna measurement technology, planar near-field RCS measurement itself is obviously not a mature technology. BDM is not at a point to design turn-key systems implementing this technology, although we have been leaders in developing and validating the mathematics and experimental protocols for these measurements.

We do feel, however, that this is a very promising avenue for near-field RCS measurement. It shows promise of addressing several important issues of RCS measurement:

- (1) measuring RCS of low-observable objects,
- (2) measuring monostatic and bistatic RCS,
- (3) providing a secure facility for RCS measurement,

- (4) increased accuracy, and
- (5) increased repeatability.

In the following sections we discuss some technology areas that need further development. Specific areas of planar near-field RCS technology are discussed in the terms of topic problem areas and tentative solutions. Environmental factors are also noted where appropriate.

B. REALISTIC RCS MEASUREMENT REQUIREMENTS

There is currently a credibility gap that must be surmounted. Although the theoretical basis for converting near-field RCS to far-field RCS is firm, there has been no large-scale demonstration that near-field RCS data will yield valid, believable far-field RCS for realistic military targets. It is necessary to establish analytical bases for relating conventional far-field RCS measurements and near-field RCS measurements, identify limitations of both far-field and near-field RCS measurements, and investigate the extent to which the statistical characteristics of far-field and near-field data are complementary.

There will be some difficulties encountered in measuring low-observable RCS, since, as in conventional far-field ranges, the RCS may be comparable to the background scattering levels in the system. It is necessary to identify mechanisms for dealing optimally with low signal/noise measurement environments.

The actual requirements for RCS data quantity and precision are not clear. While very accurate RCS from many angles is desirable, what is actually acceptable? There is a need for realistic RCS requirements assessments based upon system specifications and mission requirements.

The analysis of near-field RCS data has moderate computational complexity. Studies are needed to identify trade-off elements, precision, and computational complexity and apply a systems view of the problem to determine computational trade-offs.

C. THEORETICAL BASIS

The theoretical basis for near-field RCS measurements needs expanding. Among the effects that need additional investigation are multiple interactions between probes and objects, ways of reducing the computational burden, effects of undersampling the data field, maximum entropy constraints to reduce what would be redundant information in a noise-free environment, algorithm modifications to compute parameters of estimated statistical distributions directly for RCS or antenna patterns, and more effective probe antenna designs and patterns.

D. CALIBRATION

Existing RF technology is generally adequate to support this RCS measurement technique. Care must be taken in stable design of signal sources, feeds, and receivers. The mechanical and electrical design of the antennas and feeds will require ingenuity. Calibration of such a near-field RCS measurement facility would probably require built-in calibration loops in the RF paths to allow adaptive self-test and recalibration during data runs. Implications of such self-test loops, and the possibility of using created white (or other suitably defined) spatial and frequency noise sources and out-of-band techniques to check calibration in real time, should be investigated.

E. MEASURING THE NECESSARY DATA

The two key problems for this near-field measurement approach are the amount of data that must be measured, and the time that will be required to make the measurements. There is no fundamental obstacle to recording the necessary data, but it calls for clever measurement system design and data processing algorithms.

The measured near-field data will be voluminous. Ways are needed to reduce the amount of data required, and to efficiently store the data once they are measured. Possible paths to pursue are to achieve data density reductions by alternative computation and analysis algorithms; data coding algorithms to reduce data volume for acquisition, storage, and processing; trade-offs between data precision, storage requirements, and analysis

accuracy; new algorithms (eigenstructure, analytic and series functions, and orthogonal expansions) for reducing sampling density; determining what can be done numerically to utilize magnitude-only or phase-only measurements; use of error-free versus non-error-free data compression; use of densely-packed antenna arrays; and investigation of various high-density digital data storage media including optical disk and holographic storage.

Other avenues of investigation include fully-automated measurements systems, computer-controlled data collection and probe and target positioning with process quality feedback, time-division and frequency-division multiplex antenna and feed systems, fast-response servo control systems for probe antenna positioning, existing laser metrology systems for closed-loop control of antenna position, multiple transmit and receive channels with broad-band intermediate frequency strips to allow high-speed I-Q measurements, parallel computationally-specific dedicated processors, and combined data measurement and analog computation.

The various RF coupling paths between measurements system and object must be analyzed as part of the error analysis. Signal-to-noise limitations must be evaluated, particularly in light of low-observable targets, broad IF bandwidths in receivers, and system noise figure. Other signal-to-noise issues include using multiple coherent data measurements, background scatter reduction, coherent or incoherent background subtraction and suppression, absorption and signature techniques, effects of multiple reflections, explicit time gating and implicit gating using synthetic spectra and data signatures, environmental changes and deviations from ideal, and factor analysis.

Part of that investigation would be to evaluate the level of specular and diffuse reflections that may be present from both object and background, and possibly create modified algorithms tailored respectively to emphasize or reject specular and diffuse reflections via a feed-back loop, using results to isolate undesired components of the background.

Obtaining the necessary metrology accuracy is not a trivial problem, but is well within the state of the art. Tools to be used here include laser interferometry, closed loop control, real-time RF frequency and phase error measurement and adaptive correction, and phase locking techniques. Timing errors can be minimized by referring all measurements to a master clock to correct the time references of data as required.

It is necessary to evaluate reproducibility of measurement conditions. Reproducibility is impacted by environmental effects, equipment drift, structural stability, target stability, and aging, and might be measured in terms of pattern distributions and statistical confidence intervals.

Effects of non-ideal measurement components (e.g., amplifiers, mixers) must be evaluated. One approach is to exercise and modify algorithms as required to examine data behavior given non-ideal components, including error analyses, simulation, and experiments to evaluate effects of component variability.

Possible methods of alleviating undesired effects of probe characteristics include using broad-band, low mutual coupling, variable polarization, active nonlinear elements. Adequate polarization and geometry control may allow simplifications in the data processing algorithms; this will require detailed antenna analysis and design and feed systems using PIN diode switching and compensating elements.

Environmental noise components might be isolated and compensated for by measuring and assigning data signatures to various environmental and measurement elements and demodulating the undesired signatures in real time. Environmental interference might also be reduced by using out-of-band data from known targets to isolate environmental interference on a real-time basis.

Approaches to reducing data computational burden include using canonic simplifications based on alternative measurement and analysis algorithms, and simultaneous measurement, computation, and analysis using buffered computations and direct transform algorithms.

Data collection monitoring and quality control call for automated operations and on-line factor analysis to determine data error sensitivity. The need for identifying unusual measurement problems during data acquisition suggests that one should create an evolving data pattern generated incrementally as measurement data are obtained, so that algorithms can detect divergence from the emerging pattern.

F. DATA ANALYSIS

The relations between input and output data quantity and quality, and numerical effects in the data analysis algorithms, need additional investigation. Possible approaches are to employ a 64-bit (or longer) word-length computer to simulate a variable word length computer and thus determine the numerical sensitivity of the algorithms and optimize the algorithms for minimum sensitivity; investigate dynamic range limitations due to numerical considerations of using large Fast Fourier Transforms (FFTs); and possible use of phase-only data. Simulations are needed to help determine error relations between data inputs and outputs. Data analysis time and resources could be reduced by using dedicated hardware FFTs and processors.

Additional paths to reducing computational complexity include using the physical situation's constraints (both target and environment), using mathematical structure constraints, adding other constraints on information content, matching the information content of the channel between measurements and canonic results, factor analysis, and various operations research techniques (including linear programming).

Other possible data and algorithm modifications include using blank data cells (under sampling), truncation (blanking), zero interpolation, blanking interpolation, various simplifications and alternatives to the existing near-field theory, solving dual/analog problems, identifying relations between simplification and useful outputs, computing pattern statistics rather than RCS patterns, and using object and algorithm functional symmetry.

G. OPERATIONAL CONSIDERATIONS

We emphasize again that it is not clear what RCS data are really needed for existing aircraft and missiles. It would be a noteworthy capability simply to be able to measure monostatic RCS at, say, one degree intervals for angles within ± 30 degrees of the horizon, but it is not clear whether mission effectiveness would be truly enhanced by such detailed knowledge. Perhaps it would be more useful to be able to state that the maximum RCS over a specified solid angle is less than x with probability y . The range of angles and the angular resolution of the data have major technical (measurement time and data volume) and economic (time and cost) impact. As aids to baselining this measurement approach, time and data volume could be estimated for specific measurement scenarios, given the angular range and resolution needed.

The absolute RCS accuracy required for mission evaluation has a major impact upon how much data are needed, how long it takes to measure the data, and what kind of algorithms are used to process and display the data. Acceptable and desirable measurement accuracy constraints for mission scenarios must be established.

The mission scenario elements together impose stringent requirements upon the measurement system. As part of identifying true measurement needs, a system level evaluation of mission and operations use of RCS data is needed, to determine feasible costs (time, capital, and staff), and to perform trade-off analyses and simulations.

REFERENCES

1. Hewlett-Packard 8408B System Manual, P/N 08408-90009, August 1982.
2. Yaghjian, A.D., "Approximate Formulas for the Far Field and Gain of Open-Ended Rectangular Waveguide", IEEE Trans. Ant. Prop., Vol AP-32, No. 4., April 1984.
3. M. Born & E. Wolf, Principles of Optics, Pergamon Press, 1965, Appendix III.
4. Stutzman & Thiele, Antenna Theory and Design, Wiley, 1981, page 16.
5. Kerns D.M., Plane-Wave Scattering Matrix Theory of Antennas and Antenna-Antenna Interactions, National Bureau of Standards Monograph 162, June 1981, page 62.
6. C.A. Balanis, Antenna Theory: Analysis and Design, Harper & Row, 1982.
7. Yaghjian, A.D., "An Overview of Near-Field Antenna Measurements," IEEE Trans. Ant. Prop., Vol. AP-34, No. 1, January 1986.
8. Yaghjian, A.D., "Overview...", p. 37.
9. Joy, E.B., and Paris, D.T., "Spatial Sampling and Filtering in Near-Field Measurements," IEEE Trans. Ant. Prop., Vol. AP-20, No. 3, May 1972.
10. Newell, A.C., Planar Near-Field Measurements, June 1985 (unpublished).
11. Kerns, D.M., NBS Monograph 162, p. 73.
12. Oppenheim, A.V., and Shafer, R.W., Digital Signal Processing, Prentice-Hall, 1975.
13. J.S. Bendat and A.G. Piersol, Measurement and Analysis of Random Data, Wiley & Sons, 1966.
14. Papoulis, A., Probability, Random Variables, and Stochastic Processes, McGraw-Hill, 1965.
15. Natarajan, N.A., Discrete-Time Signals and Systems, Reston Publishing Co., Inc., Reston, VA, 1983.
16. Dinallo, M.A., "Extension of Plane-Wave Scattering-Matrix Theory of Antenna-Antenna Interactions to Three Antennas: A Near-Field Radar Cross-Section Concept," Proc. Antenna Applications Symposium, University of Illinois, September 1984.
17. Dinallo, 1984, eq (18).
18. Papoulis, A., The Fourier Integral and its Applications, McGraw-Hill, 1962.
19. Stratton, Electromagnetic Theory, McGraw-Hill, 1941, pp. 563 to 573.

APPENDIX A

COORDINATE SYSTEMS

A. COORDINATE SYSTEMS

There are two coordinate systems (Figure A-1) to deal with in performing near-field measurements: the scan table coordinate system (S') and the antenna coordinate system (S). In the context of bistatic RCS measurements, the antenna coordinate system is referred to as the test object coordinate system.

The scan table coordinate system is the "laboratory" coordinate frame in which measurements are taken, while the antenna coordinate system is the natural coordinate frame for the antenna or object under test. Both are right-handed coordinate systems.

The scan table coordinate system is defined with horizontal $x'-y'$ plane and z' -axis upwards. The x' -axis corresponds to movement of a platform only, while the y' -axis corresponds to movement of a carriage along with its platform.

The origin of the scan table coordinate system is at the center of the aperture of the TX probe antenna when the TX platform is at its initial ("home") position. The horizontal position of the origin coincides with the TX probe antenna mounting hole in the TX platform, while the height of the origin above laboratory floor level depends upon the height of the TX probe antenna that is installed.

The origin of the antenna coordinate system S is placed at some convenient reference point on the AUT. If \vec{r}'_0 is the representation in S' of a vector from the origin of S' to the origin of S , then a vector \vec{r}' expressed in S' transforms to S as

$$\vec{r} = \underline{V} \cdot (\vec{r}' - \vec{r}'_0),$$

where

$$\begin{aligned} \vec{r}'_0 &\equiv r'_{0x} \hat{e}'_x + r'_{0y} \hat{e}'_y + r'_{0z} \hat{e}'_z, \\ \underline{V} &= \begin{bmatrix} 1 & 0 & 0 \\ 0 & -1 & 0 \\ 0 & 0 & -1 \end{bmatrix}, \\ \vec{r} &\equiv r_x \hat{e}_x + r_y \hat{e}_y + r_z \hat{e}_z, \text{ and} \end{aligned}$$

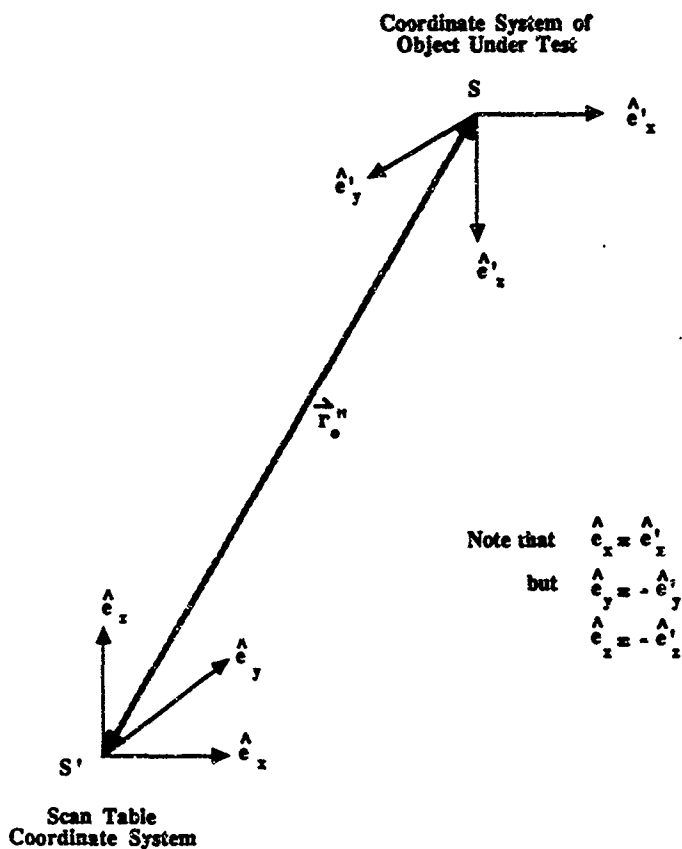


Figure A-1. Coordinate Systems

If the unit direction vector \vec{A} is expressed in spherical coordinates as (r, θ, ϕ) , then its negative $(-\vec{A})$ is written as $(r, \pi - \theta, \pi + \phi)$.

If the unit direction vector \vec{A} is expressed in spherical coordinates in S as (r, θ, ϕ) , then it is expressed in S' as $\vec{A}' = (r', \theta', \phi')$, where

$$r' = r$$

$$\theta' = \pi - \theta$$

$$\phi' = -\phi.$$

If the unit direction vector \vec{A} is expressed in spherical coordinates in S as (r, θ, ϕ) , then its negative $(-\vec{A})$ expressed in S' is $-\vec{A} = (r', \theta', \phi')$, where

$$r' = r$$

$$\theta' = \theta$$

$$\phi' = -(\pi + \phi).$$

The above relations can be verified by inspection of the coordinate systems involved. We require that

$$r \geq 0$$

$$0 \leq \theta \leq \pi$$

$$-\pi \leq \phi \leq \pi.$$

S' is used to describe the probe antenna TX and RX characteristics since these functions do not depend on a probe's location in S' .

C. ILLUMINATING PLANE WAVE

The target is illuminated by a plane wave with polarization \vec{E}_1 ($\vec{E}_1 \cdot \vec{k}_1 = 0$) that is effectively emitted from coordinates (x'_1, y'_1, z'_1) in S' toward the target centered at known coordinates (x'_0, y'_0, z'_0) in S' . Define a unit vector \vec{r}_1 in S' in the direction $(x'_0 - x'_1, y'_0 - y'_1, z'_0 - z'_1)$. The vector \vec{r}_1 is known, since \vec{r}_1 is a unit wave-vector from the far-field illumination direction (if TX probe is scanning), or (x'_1, y'_1, z'_1) is the TX probe position and \vec{r}_1 can be calculated (if the TX probe is stationary).

If the unit direction vector \vec{A} is expressed in spherical coordinates as (r, θ, ϕ) , then its negative $(-\vec{A})$ is written as $(r, \pi - \theta, \pi + \phi)$.

If the unit direction vector \vec{A} is expressed in spherical coordinates in S as (r, θ, ϕ) , then it is expressed in S' as $\vec{A}' = (r', \theta', \phi')$, where

$$r' = r$$

$$\theta' = \pi - \theta$$

$$\phi' = -\phi.$$

If the unit direction vector \vec{A} is expressed in spherical coordinates in S as (r, θ, ϕ) , then its negative $(-\vec{A})$ expressed in S' is $-\vec{A} = (r', \theta', \phi')$, where

$$r' = r$$

$$\theta' = \theta$$

$$\phi' = -(\pi + \phi).$$

The above relations can be verified by inspection of the coordinate systems involved. We require that

$$r \geq 0$$

$$0 \leq \theta \leq \pi$$

$$-\pi \leq \phi \leq \pi.$$

S' is used to describe the probe antenna TX and RX characteristics since these functions do not depend on a probe's location in S' .

C. ILLUMINATING PLANE WAVE

The target is illuminated by a plane wave with polarization \vec{E}_1 ($\vec{E}_1 \cdot \vec{k}_1 = 0$) that is effectively emitted from coordinates (x'_1, y'_1, z'_1) in S' toward the target centered at known coordinates (x'_0, y'_0, z'_0) in S' . Define a unit vector \vec{r}_1 in S' in the direction $(x'_0 - x'_1, y'_0 - y'_1, z'_0 - z'_1)$. The vector \vec{r}_1 is known, since \vec{r}_1 is a unit wave-vector from the far-field illumination direction (if TX probe is scanning), or (x'_1, y'_1, z'_1) is the TX probe position and \vec{r}_1 can be calculated (if the TX probe is stationary).

The propagation vector \vec{k}_1 is expressed as

$$k'_{x1} = r'_{x1} k$$

$$k'_{y1} = r'_{y1} k$$

$$k'_{z1} = r'_{z1} k$$

or

$$r'_1 = k$$

$$\theta'_1 = \cos^{-1}(r'_{z1})$$

$$\phi'_1 = \tan^{-1}(r'_{y1}/r'_{x1})$$

where

$$k \equiv 2\pi/\lambda.$$

We also know, or will specify arbitrarily, the polarization of the illuminating plane wave. If the TX probe is scanning, we select the polarization(s) E'_θ or E'_ϕ for a particular simulation. If the TX probe is a stationary standard gain horn pointed at the object, we will orient the horn so that the object is on-axis and the E-plane of the horn is either vertical or horizontal in S' , so that the transmitted polarization is either purely E'_θ or purely E'_ϕ .

If the polarization is known in the basis set

$$\vec{E}'_1 \equiv (E'_{x1}, E'_{y1}, E'_{z1}),$$

then the spherical components of the polarization are

$$E'_{r1} = E'_{x1} \sin \theta_1 \cos \phi_1 + E'_{y1} \sin \theta_1 \sin \phi_1 + E'_{z1} \cos \theta_1$$

$$E'_{\theta 1} = E'_{x1} \cos \theta_1 \cos \phi_1 + E'_{y1} \cos \theta_1 \sin \phi_1 - E'_{z1} \sin \theta_1$$

$$E'_{\phi 1} = -E'_{x1} \sin \phi_1 + E'_{y1} \cos \phi_1.$$

If the polarization is known in the basis set

$$\vec{E}'_1 \equiv (E'_{r1}, E'_{\theta 1}, E'_{\phi 1}),$$

then the Cartesian components of polarization are

$$E'_{x1} = E'_{r1} \sin \theta_1 \cos \phi_1 + E'_{\theta 1} \cos \theta_1 \cos \phi_1 - E'_{\phi 1} \sin \phi_1$$

$$E'_{y1} = E'_{r1} \sin \theta_1 \sin \phi_1 + E'_{\theta 1} \cos \theta_1 \sin \phi_1 + E'_{\phi 1} \cos \phi_1$$

$$E'_{z1} = E'_{r1} \cos \theta_1 - E'_{\theta 1} \sin \theta_1,$$

and E'_r must be selected to ensure that $\vec{k}'_1 \cdot \vec{E}'_1 = 0$. Thus \vec{E}'_1 can be expressed in either Cartesian or spherical coordinates using the above transformation equations.

The propagation vector \vec{k}'_1 is expressed in S via the transformations

$$k_{x1} = +k'_{x1}$$

$$k_{y1} = -k'_{y1}$$

$$k_{z1} = -k'_{z1}$$

or

$$r_1 = r'_{11}$$

$$\theta_1 = \pi - \theta'_1$$

$$\phi_1 = -\phi'_1.$$

The polarization vector \vec{E}'_1 is expressed in S via the transformations

$$E_{x1} = +E'_{x1}$$

$$E_{y1} = -E'_{y1}$$

$$E_{z1} = -E'_{z1}$$

or

$$E_{r1} = +E'_{r1}$$

$$E_{\theta 1} = -E'_{\theta 1}$$

$$E_{\phi 1} = -E'_{\phi 1}.$$

Therefore we can express the incident wave-vector (\vec{k}'_1) and polarization (\vec{E}'_1) in either Cartesian or spherical components in S, which is the coordinate system of the target.

D. SCATTERED PLANE WAVE

The target scatters the illuminating plane wave into plane waves in various directions. In order to evaluate the scattering, we select a particular scattering direction based upon where the observer is in the far-field.

Consider a plane wave that is scattered toward the known coordinates (x'_2, y'_2, z'_2) in S' . Define a unit vector \vec{r}'_2 in S' in the direction ($x'_2 - x'_0, y'_2 - y'_0, z'_2 - z'_0$). The propagation

vector \vec{k}'_2 is expressed as

$$k'_{x2} = r'_{x2}k$$

$$k'_{y2} = r'_{y2}k$$

$$k'_{z2} = r'_{z2}k$$

or

$$r'_2 = k$$

$$\theta'_2 = \cos^{-1}(r'_{z2})$$

$$\phi'_2 = \tan^{-1}(r'_{y2}, r'_{x2})$$

where $k \equiv 2\pi/\lambda$.

If scattering in a known direction is desired rather than scattering toward a known coordinate, then \vec{r}'_2 (expressed in S') is the scattering direction and (x'_2, y'_2, z'_2) need not be known.

The propagation vector \vec{k}_2 is expressed in S via the transformations

$$k_{x2} = +k'_{x2}$$

$$k_{y2} = -k'_{y2}$$

$$k_{z2} = -k'_{z2}$$

or

$$r_2 = r'_2$$

$$\theta_2 = \pi - \theta'_2$$

$$\phi_2 = -\phi'_2$$

E. SCATTERING CALCULATION

At this point we know the incident k -vector (\vec{k}_1), the incident polarization (\vec{E}_1), and the scattering k -vector (\vec{k}_2), all expressed in S , so we can compute the polarization vector (\vec{E}_2) of the far-field scattered plane wave (Figure A-2) by means of an analytic or numerical model of the scattering object. The usual range-dependent phase factor can be ingored.

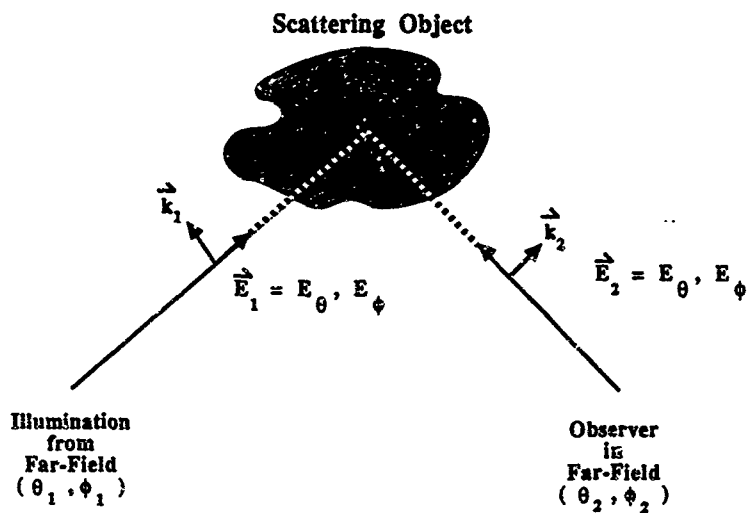


Figure A-2. Scattering Geometry

The scattering analysis of the sphere requires that the object be in a preferred coordinate system S'' in which it is illuminated by an incident plane wave having propagation vector $|\vec{k}| \hat{e}_z$ and linear polarization $|\vec{E}| \hat{e}_x$. Since \vec{k}_1 and \vec{E}_1 are not so constrained, we must construct a coordinate rotation matrix \underline{A} that defines a new coordinate system S'' in which

$$\underline{A} \cdot \vec{k}_1 = |\vec{k}_1| \hat{e}_z'' \text{ and}$$

$$\underline{A} \cdot \vec{E}_1 = |\vec{E}_1| \hat{e}_x'',$$

where we must have

$$\vec{k}_1 \cdot \vec{E}_1 = 0$$

$$\vec{k}_2 \cdot \vec{E}_2 = 0.$$

The coordinate rotation \underline{A} transforms an arbitrary linearly polarized incident plane wave into a plane wave propagating in the \hat{e}_z'' direction with \hat{e}_x'' polarization. The scattering direction is also transformed as

$$\vec{k}_2'' = \underline{A} \cdot \vec{k}_2.$$

At this point \vec{k}_1 , \vec{E}_1 , and \vec{k}_2 are known numerically, so the scattered polarization \vec{E}_2'' can be calculated in S'' using the appropriate analysis (e.g., Stratton for the dielectric sphere) and then transformed back to S as

$$\vec{E}_2 = \underline{A}^{-1} \cdot \vec{E}_2''.$$

The matrix \underline{A} is computed in three steps. Let \underline{A}_x be a matrix that rotates a vector \vec{k} (for which we will actually use \vec{k}_1) about \hat{e}_x by an angle

$$\alpha_1 = -\tan^{-1} \left[\frac{k_y}{k_z} \right].$$

This rotation reduces k_y to zero, so the rotated \vec{k} (which we will call $\vec{k}^{(1)}$) lies in the $\hat{e}_x \hat{e}_z$ plane. The matrix is

$$\underline{A}_x = \begin{bmatrix} 1 & 0 & 0 \\ 0 & \cos(\alpha_1) & \sin(\alpha_1) \\ 0 & -\sin(\alpha_1) & \cos(\alpha_1) \end{bmatrix},$$

so

$$\hat{k}^{(1)} = \underline{A}_x \cdot \hat{k},$$

and applying the same rotation to \hat{E} gives

$$\hat{E}^{(1)} = \underline{A}_x \cdot \hat{E}.$$

Next, let \underline{A}_y be a matrix that rotates a vector about \hat{e}_y by an angle

$$\alpha_2 = -\tan^{-1} \left[\frac{k_x^{(1)}}{k_z^{(1)}} \right].$$

This rotation reduces $k_x^{(1)}$ to zero, so the rotated $\hat{k}^{(1)}$ (which we will call $\hat{k}^{(2)}$) lies on the \hat{e}_z axis. The matrix for this rotation is

$$\underline{A}_y = \begin{bmatrix} \cos(\alpha_2) & 0 & \sin(\alpha_2) \\ 0 & 1 & 0 \\ -\sin(\alpha_2) & 0 & \cos(\alpha_2) \end{bmatrix},$$

so

$$\hat{k}^{(2)} = \underline{A}_x \cdot \hat{k}^{(1)}$$

$$\hat{E}^{(2)} = \underline{A}_x \cdot \hat{E}^{(1)}.$$

At this point, $\hat{k}^{(2)}$ is on the \hat{e}_z axis, as desired, and $\hat{E}^{(2)}$ is in the $\hat{e}_x\hat{e}_y$ plane.

Finally, let \underline{A}_z be a matrix that rotates a vector about \hat{e}_z by an angle

$$\alpha_3 = \tan^{-1} \left[\frac{E_y^{(2)}}{E_x^{(2)}} \right].$$

This rotation reduces $E_y^{(2)}$ to zero, so the rotated $\hat{E}^{(2)}$ (which we will call $\hat{E}^{(3)}$) will lie on the \hat{e}_x axis. The matrix is

$$\underline{A}_z = \begin{bmatrix} \cos(\alpha_3) & \sin(\alpha_3) & 0 \\ -\sin(\alpha_3) & \cos(\alpha_3) & 0 \\ 0 & 0 & 1 \end{bmatrix}.$$

The desired coordinate rotation matrix is

$$\underline{A} = \underline{A}_z \cdot \underline{A}_y \cdot \underline{A}_x.$$

The scattering analysis of the disk requires that the object be in a preferred coordinate system S'' in which it is illuminated by an incident plane wave from above the \hat{e}_x - \hat{e}_y plane having propagation vector $\hat{k} = (-\sin\theta''\hat{e}_x - \cos\theta''\hat{e}_z)$ and linear

polarization $E_{0\parallel}\hat{e}_{\parallel} + E_{0\perp}\hat{e}_{\perp}$, where \hat{e}_{\parallel} is in the plane $\hat{k}-\hat{e}_z$ and $\hat{e}_{\perp}\perp\hat{e}_y$. Since \hat{k}_1 and \hat{E}_1 are not so constrained, we must construct a coordinate rotation matrix \underline{A} that defines a new coordinate system S'' in which

$$\underline{A}\cdot\hat{k}_1 = |\hat{k}_1| (-\sin\theta''\hat{e}_x - \cos\theta''\hat{e}_z) \text{ and}$$

$$\underline{A}\cdot\hat{E}_1 = E_{1\parallel}\hat{e}_{\parallel} + E_{1\perp}\hat{e}_{\perp},$$

where we must still have

$$\hat{k}_1\cdot\hat{E}_1=0$$

$$\hat{k}_2\cdot\hat{E}_2=0.$$

The scattering direction is also transformed as $\hat{k}_2'' = \underline{A}\cdot\hat{k}_2$.

The matrix \underline{A} is computed in two steps. Let \underline{A}_x be a matrix that rotates a vector \hat{k} (for which we will actually use \hat{k}_1) about \hat{e}_x by an angle

$$\alpha_1 = \begin{cases} 0 & \text{if } k_z < 0 \\ \pi & \text{if } k_z > 0 \end{cases}.$$

This rotation ensures that k_z is non-positive, as required, so the rotated \hat{k} (which we will call $\hat{k}^{(1)}$) lies below the $\hat{e}_x\hat{e}_y$ plane. The matrix is

$$\underline{A}_x = \begin{bmatrix} 1 & 0 & 0 \\ 0 & \cos(\alpha_1) & \sin(\alpha_1) \\ 0 & -\sin(\alpha_1) & \cos(\alpha_1) \end{bmatrix}.$$

so

$$\hat{k}^{(1)} = \underline{A}_x\cdot\hat{k},$$

and applying the same rotation to \hat{E} gives

$$\hat{E}^{(1)} = \underline{A}_x\cdot\hat{E}.$$

Then let \underline{A}_z be a matrix that rotates a vector about \hat{e}_z by an angle

$$\alpha_2 = \tan^{-1} \left[\frac{k_y^{(1)}}{k_x^{(1)}} \right] + \pi.$$

This rotation reduces $k_y^{(1)}$ to zero and makes $k_x^{(1)}$ negative. The matrix is

$$\underline{A}_z = \begin{bmatrix} \cos(\alpha_2) & \sin(\alpha_2) & 0 \\ -\sin(\alpha_2) & \cos(\alpha_2) & 0 \\ 0 & 0 & 1 \end{bmatrix}.$$

The desired coordinate rotation matrix is $\underline{A} = \underline{A}_z \cdot \underline{A}_x$. Applying \underline{A} to \vec{E}_1 ,

$$\begin{aligned}\vec{E}_1'' &= \underline{A} \vec{E}_1 \\ &= E_{1x}'' \hat{e}_x + E_{1y}'' \hat{e}_y + E_{1z}'' \hat{e}_z\end{aligned}$$

In S'' the angles of incidence and emergence of the plane waves are

$$\theta_1'' = \cos^{-1} (k_{1z}''/k_1)$$

$$\phi_1'' = 0,$$

and

$$\begin{aligned}\theta_2'' &= \cos^{-1} (k_{2z}''/k_2) \\ \phi_2'' &= \tan^{-1} \left[\frac{k_{2y}''}{k_{2x}''} \right].\end{aligned}$$

The incident polarization parallel and perpendicular to the plane of incidence in S'' are

$$\begin{aligned}\vec{E}_{1\parallel}'' &= |\vec{E}_1''| (-\cos\theta_1'' \hat{e}_x + \sin\theta_1'' \hat{e}_z) \\ \vec{E}_{1\perp}'' &= |\vec{E}_1''| \hat{e}_y.\end{aligned}$$

At this point \vec{k}_1'' , \vec{E}_1'' , and \vec{k}_2'' are known numerically, so the scattered polarization \vec{E}_2'' can be calculated in S'' as a linear combination of $E_{1\parallel}''$ and $E_{1\perp}''$:

$$\begin{bmatrix} E_{2\parallel}'' \\ E_{2\perp}'' \end{bmatrix} = \begin{bmatrix} S_{11} & S_{12} \\ S_{21} & S_{22} \end{bmatrix} \begin{bmatrix} E_{1\parallel}'' \\ E_{1\perp}'' \end{bmatrix}.$$

In terms of $\hat{e}_x'' \hat{e}_y'' \hat{e}_z''$,

$$\vec{E}_2'' = E_{2\parallel}'' \cos\theta_2'' \hat{e}_x'' + E_{2\perp}'' \hat{e}_y'' + E_{2\parallel}'' \sin\theta_2'' \hat{e}_z'',$$

which is transformed back to S as

$$\vec{E}_2 = \underline{A}^{-1} \cdot \vec{E}_2''.$$

F. Transformation of Scattered Wave

If the predicted far-field scattered plane wave's polarization vector is $\vec{E}_2 = (E_{x2}, E_{y2}, E_{z2})$ when expressed in S , then the spherical components of polarization are

$$E_{r2} = E_{x2} \sin\theta_2 \cos\phi_2 + E_{y2} \sin\theta_2 \sin\phi_2 + E_{z2} \cos\theta_2$$

$$E_{\theta2} = E_{x2} \cos\theta_2 \cos\phi_2 + E_{y2} \cos\theta_2 \sin\phi_2 - E_{z2} \sin\theta_2$$

$$E_{\phi2} = -E_{x2} \sin\phi_2 + E_{y2} \cos\phi_2.$$

If the calculated polarization in spherical coordinates is

$$\vec{E}_2 \equiv (E_{r2}, E_{\theta2}, E_{\phi2})$$

when expressed in S, then the Cartesian components are

$$E_{x2} = E_{r2} \sin \theta_2 \cos \phi_2 + E_{\theta2} \cos \theta_2 \cos \phi_2 - E_{\phi2} \sin \phi_2$$

$$E_{y2} = E_{r2} \sin \theta_2 \sin \phi_2 + E_{\theta2} \cos \theta_2 \sin \phi_2 + E_{\phi2} \cos \phi_2$$

$$E_{z2} = E_{r2} \cos \theta_2 - E_{\theta2} \sin \theta_2$$

The polarization vector is expressed in S' via the transformations

$$E'_{x2} = +E_{x2}$$

$$E'_{y2} = -E_{y2}$$

$$E'_{z2} = -E_{z2}$$

or

$$E'_{r2} = +E_{r2}$$

$$E'_{\theta2} = -E_{\theta2}$$

$$E'_{\phi2} = -E_{\phi2}$$

By means of the above equations, the scattered wave-vector (\vec{k}_2) and polarization (\vec{E}_2) can be expressed in S' using either Cartesian or spherical components.

The far-field scattered electric field is given by \vec{E}_2 and \vec{k}_2 , which can be expressed in terms of S or S'. It is probably best to stay in S, which is the natural coordinate system for the scattering object.

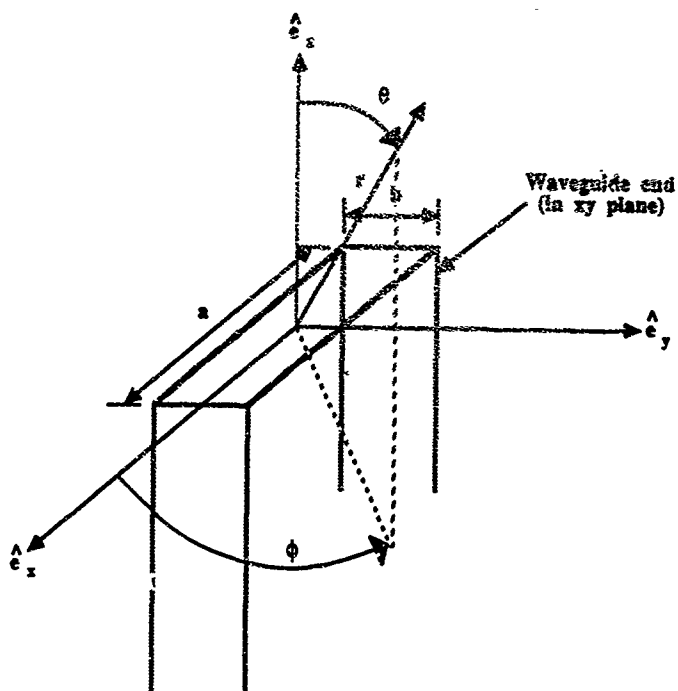


Figure B-1. Open-End Waveguide Geometry

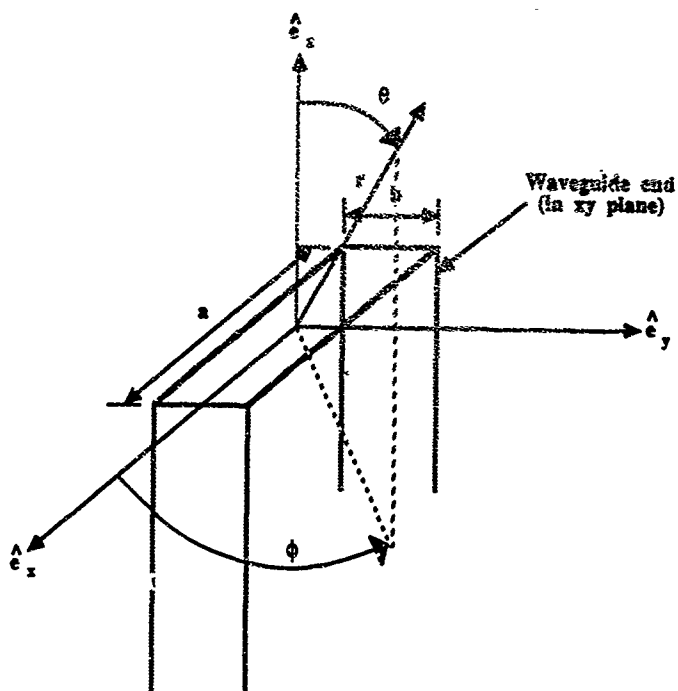


Figure B-1. Open-End Waveguide Geometry

B. METHOD OF STATIONARY PHASE

In this section we summarize the relationship between the angular plane-wave spectrum of an E-field and the far-field E-field that emerges by applying the method of stationary phase to calculation of far-field E-field.

Consider an E-field expressed in the following form

$$\vec{E}(\vec{r}) = \iint \vec{B}(\vec{k}) e^{i\vec{k} \cdot \vec{r}} d\vec{k}_x d\vec{k}_y.$$

The first step in finding the far field is to convert to spherical coordinates. Thus, we define

$$\vec{P}(\theta, \phi) \equiv k^2 \sin \theta \cos \phi \vec{B}(\vec{k})$$

$$\vec{k} \equiv k (\sin \theta \cos \phi \hat{e}_x + \sin \theta \sin \phi \hat{e}_y + \cos \theta \hat{e}_z)$$

$$\vec{r} \equiv r (\sin \alpha \cos \beta \hat{e}_x + \sin \alpha \sin \beta \hat{e}_y + \cos \alpha \hat{e}_z),$$

from which for $k|\vec{r}|$ we obtain

$$\vec{E}(\vec{r}) = \iint \vec{P}(\theta, \phi) e^{ikr[\cos \theta \cos \alpha + \sin \theta \sin \alpha \cos(\theta - \alpha)]} d\theta d\phi.$$

This is now in the correct form for invoking the method of stationary phase [3].

Since the method is somewhat involved, we quote the result and reference the details to Born and Wolf. In their notation (Appendix III, pp. 753-754, eq 16 and 19),

$$\iint g(x, y) e^{ikf(x, y)} dx dy = \frac{2\pi i \sigma}{|\alpha\beta - \gamma^2|} g(x_0, y_0) \frac{e^{ikf(x_0, y_0)}}{k},$$

where

$$\alpha = \frac{\partial^2 f}{\partial x^2}$$

$$\beta = \frac{\partial^2 f}{\partial y^2}$$

$$\gamma = \frac{\partial^2 f}{\partial x \partial y}$$

$$\sigma = \begin{cases} +1 & \text{if } \alpha\beta > \gamma^2 \text{ and } \alpha > 0 \\ -1 & \text{if } \alpha\beta > \gamma^2 \text{ and } \alpha < 0 \\ -i & \text{if } \alpha\beta < \gamma^2 \end{cases}$$

and (x_0, y_0) is the critical point at which

$$\frac{\partial f}{\partial x} = \frac{\partial f}{\partial y} = 0.$$

Thus, in our notation, the far field is

$$\begin{aligned} \lim_{|\vec{r}| \rightarrow \infty} \vec{E}(\vec{r}) &= \frac{2\pi k e}{i r} \cos(\theta) \vec{B}(\vec{k}) \\ &= \frac{2\pi k e}{i r} \cos(\theta) [B_\theta(\theta, \phi) \hat{e}_\theta + B_\phi(\theta, \phi) \hat{e}_\phi], \end{aligned}$$

where

$$\cos \theta = \frac{k_z}{k}.$$

Suppose we have a far field

$$\lim_{|\vec{r}| \rightarrow \infty} \vec{E}(\vec{r}) = a_0 [E_\theta(\theta, \phi) \hat{e}_\theta + E_\phi(\theta, \phi) \hat{e}_\phi] \frac{e^{ikr}}{kr}.$$

Substituting into the previous equation gives

$$B_\theta(\theta, \phi) = \frac{i a_0}{2\pi k^2 \cos \theta} E_\theta(\theta, \phi)$$

and

$$B_\phi(\theta, \phi) = \frac{i a_0}{2\pi k^2 \cos \theta} E_\phi(\theta, \phi).$$

Thus the angular plane-wave spectrum $\vec{B}(\vec{k})$ of an E-field can be expressed in terms of the known far-field E-field by the relation

$$\vec{B}(\vec{k}) = \frac{i}{2\pi k^2 \cos \theta} \cdot \lim_{|\vec{r}| \rightarrow \infty} [kr e^{-i\vec{k} \cdot \vec{r}} \vec{E}(\vec{r})],$$

where $\vec{k} \parallel \vec{r}$.

Later, when using plane wave spectra to define the transmit characteristic of an antenna, we use the symbol $\vec{s}_{10}(\vec{k})$ instead of $\vec{B}(\vec{k})$. Hence,

$$\vec{s}_{10}(\vec{k}) = \frac{i}{2\pi k^2 \cos \theta} \cdot \lim_{|\vec{r}| \rightarrow \infty} [kr e^{-i\vec{k} \cdot \vec{r}} \vec{E}(\vec{r})].$$

C. OPEN-ENDED WAVEGUIDE

In this section we determine the magnitude of the TE_{10} mode excited in an open-ended waveguide (OEWG) when illuminated by a plane wave. The motivation for this analysis is clarification of the field relations and coefficients of proportionality.

The geometry of this problem is illustrated in Figure B-2. Assume that the incident E-field at the origin is a plane wave

$$\vec{E}^{inc} = E_{\theta}^{inc}(\theta, \phi) \hat{e}_{\theta} + E_{\phi}^{inc}(\theta, \phi) \hat{e}_{\phi},$$

where $E_{\theta}^{inc}(\theta, \phi)$ and $E_{\phi}^{inc}(\theta, \phi)$ are complex scalars with an identical phase.

We will create an elemental dipole in the far field that could excite this plane wave. The E-field of a dipole is [4]

$$\vec{E}^{dip}(\vec{r}) = \frac{\kappa e}{kr} \sin(\theta) Id\vec{l},$$

where we have defined $\kappa = \frac{-i\eta}{4\pi}$, and η is the intrinsic impedance of free space.

We first choose a dipole in the far field parallel to \vec{E}^{inc} to create \vec{E}^{inc} at the origin:

$$E_{\theta}^{inc} = \frac{\kappa e}{kr} (Id\vec{l})_{\theta}$$

$$E_{\phi}^{inc} = \frac{\kappa e}{kr} (Id\vec{l})_{\phi}$$

where $d\vec{l}$ is parallel to \vec{E}^{inc} . Note that, in the $\sin(\theta)$ factor in $\vec{E}^{dip}(\vec{r})$, θ is the angle between $d\vec{l}$ and \vec{k} and is therefore $\pi/2$.

So,

$$Id\vec{l} = \frac{kr}{\kappa e^{-ikr}} \vec{E}^{inc},$$

which produces the observed incident field \vec{E}^{inc} .

We now wish to find the wave launched into the OEWG by the dipole $Id\vec{l}$. To do so, we invoke reciprocity and calculate the E-field at the dipole due to an excitation of the OEWG. Suppose, in the waveguide, we launch a wave of magnitude E_0 towards the end of the OEWG. At the aperture, we have

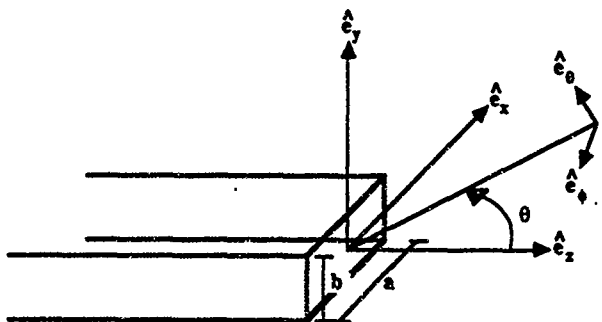


Figure B-2. Open-End Waveguide Coordinate System for Far Field

$$E_y = E_0 (1+\Gamma) \cos\left[\frac{\pi x}{a}\right] \text{ and}$$

$$H_x = -\frac{E_0}{Z_c} (1-\Gamma) \cos\left[\frac{\pi x}{a}\right],$$

where

$$Z_c = \frac{\eta}{\sqrt{1 - \left\{\frac{\pi}{ka}\right\}^2}}.$$

Next we determine a current distribution that excites this mode in the OEWG at a point λ_g from the opening (Figure B-3)

$$J_x = 2 \cdot H_x$$

$$= -2 \cdot \frac{E_0}{Z_c} \cos\left[\frac{\pi x}{a}\right],$$

where

$$\lambda_g = \frac{\lambda}{\sqrt{1 - \left\{\frac{\pi}{ka}\right\}^2}}.$$

Hence, the above current produces the open-ended waveguide far field

$$\vec{E}(\vec{r}) = A_E \frac{e^{ikr}}{kr} \left[f_\theta^{oe} \hat{e}_\theta + f_\phi^{oe} \hat{e}_\phi \right],$$

where for notational convenience we have defined

$$f_\theta^{oe}(\theta, \phi) = \frac{E_E(\theta, \phi) \sin(\phi)}{A_E}$$

$$f_\phi^{oe}(\theta, \phi) = \frac{E_H(\theta, \phi) \cos(\phi)}{A_E},$$

and $E_E(\theta, \phi)$, $E_H(\theta, \phi)$, and A_E are as defined by Yaghjian. Note that f_θ and f_ϕ are now simple unitless functions.

If we now generalize for an arbitrary antenna, we find

$$\vec{f}(\theta, \phi) = \lim_{|r| \rightarrow \infty} \frac{\vec{E}(\vec{r}, \theta, \phi) e^{-ikr}}{|E(\vec{r}, \theta=0)|}.$$

The reciprocity theorem states that

$$\iiint \vec{E}^a \cdot \vec{J}^b dV = \iiint \vec{E}^b \cdot \vec{J}^a dV.$$

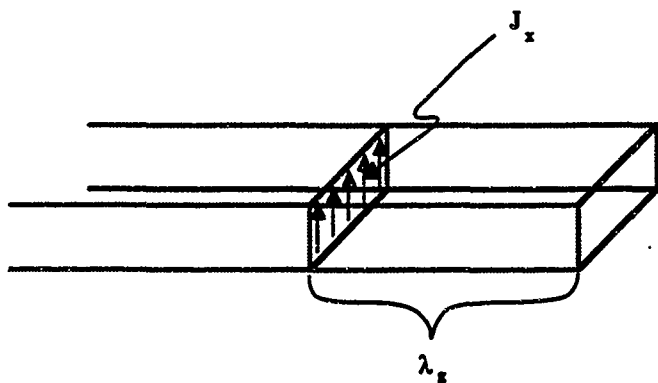


Figure B-3. Open-End Waveguide Reference Plane

In this instance the two cases (a) and (b) are:

- (a) the current sheet in the OEWG excites the far field, and
- (b) the small dipole in the far field excites the TE_{10} mode in the OEWG.

Now, the mode excited by the plane wave in the OEWG at a distance λ_g inside the open end is

$$E_y = b_0 \cos\left(\frac{\pi x}{a}\right)$$

where b_0 is unknown. Invoking reciprocity, we find

$$\tilde{J}^a = -2 \cdot \frac{E_0}{Z_c} \cos\left[\frac{\pi x}{a}\right] \hat{e}_y,$$

$$\tilde{E}^a = A_E \frac{e^{ikr}}{kr} \left[f_{\theta}^{oe} \hat{e}_{\theta} + f_{\phi}^{oe} \hat{e}_{\phi} \right],$$

$$\begin{aligned} \tilde{J}^b &= Id\hat{l}, \\ &= \frac{k r}{\kappa} e^{-ikr} \left[E_{\theta}^{inc} \hat{e}_{\theta} + E_{\phi}^{inc} \hat{e}_{\phi} \right] \end{aligned}$$

and

$$E^b = b_0 \cos\left[\frac{\pi x}{a}\right] \hat{e}_y.$$

The left-hand side of the reciprocity equation above becomes

$$\begin{aligned} \iiint \tilde{E}^a \cdot \tilde{J}^b dV &= A_E \frac{e^{ikr}}{kr} \left[f_{\theta}^{oe} \hat{e}_{\theta} + f_{\phi}^{oe} \hat{e}_{\phi} \right] \cdot \frac{k r}{\kappa} e^{-ikr} \left[E_{\theta}^{inc} \hat{e}_{\theta} + E_{\phi}^{inc} \hat{e}_{\phi} \right] \\ &= \frac{A_E}{\kappa} \left\{ f_{\theta}^{oe} E_{\theta}^{inc} + f_{\phi}^{oe} E_{\phi}^{inc} \right\} \end{aligned}$$

while the right-hand side becomes

$$\begin{aligned} \iiint \tilde{E}^b \cdot \tilde{J}^a dV &= \int_{-b/2}^{+b/2} \int_{-a/2}^{+a/2} \left\{ b_0 \cos\left[\frac{\pi x}{a}\right] \hat{e}_y \cdot \frac{-2E_0}{Z_c} \cos\left[\frac{\pi x}{a}\right] \hat{e}_y \right\} dx dy \\ &= \frac{-2b_0 E_0}{Z_c} \int_{-b/2}^{+b/2} \int_{-a/2}^{+a/2} \cos^2\left[\frac{\pi x}{a}\right] dx dy. \end{aligned}$$

Using

$$\int_{-a/2}^{+a/2} \cos^2 \left[\frac{\pi x}{a} \right] dx = \frac{a}{2},$$

the integral is

$$\iiint \vec{E}^b \cdot \vec{J}^a dV = \frac{-b_0 E_0 ab}{Z_c}.$$

Equating the left- and right-hand sides of the reciprocity equation,

$$\frac{-b_0 E_0 ab}{Z_c} = \frac{A_E}{\kappa} \{ f_{\theta}^{oe} E_{\theta}^{inc} + f_{\phi}^{oe} E_{\phi}^{inc} \},$$

so

$$b_0 = \frac{-Z_c 4\pi i A_E}{ab \eta k^2 E_0} \cdot \{ f_{\theta}^{oe} E_{\theta}^{inc} + f_{\phi}^{oe} E_{\phi}^{inc} \}.$$

Using the relation

$$Z_c = \frac{\eta}{\sqrt{1 - \left[\frac{\pi}{k a} \right]^2}}$$

we get

$$b_0 = \frac{-4\pi i A_E}{ab k^2 \sqrt{1 - \left[\frac{\pi}{k a} \right]^2} E_0} \cdot \{ f_{\theta}^{oe} E_{\theta}^{inc} + f_{\phi}^{oe} E_{\phi}^{inc} \}.$$

The above equation gives us the magnitude b_0 of the TE_{10} mode excited in an open-ended waveguide when illuminated by an incident field \vec{E}^{inc} . The receiving characteristic of the OEWG is thus

$$\vec{s}_{01}(\vec{k}) = \frac{-4\pi i A_E}{ab k^2 \sqrt{1 - \left[\frac{\pi}{k a} \right]^2} E_0} \cdot \{ f_{\theta}^{oe} \hat{e}_{\theta} + f_{\phi}^{oe} \hat{e}_{\phi} \}.$$

The ratio A_E/E_0 is calculated elsewhere.

Now let open-ended waveguide (OEWG) be illuminated by an antenna with known far-field pattern and excitation. The waveguide feed for the antenna is assumed to be identical to the waveguide used as the OEWG. The geometry for this analysis is shown in

Figure B-4. Note that the source antenna is placed in the unprimed coordinate system, and the OEWG probe is in the primed system. We define

a_0 = excitation in waveguide of known antenna, and

b_0 = excitation in OEWG.

Both a_0 and b_0 are defined at a distance λ_g from the origin of the respective coordinate systems.

In the coordinate system O (that of the antenna under test), the far-field E-field of the antenna is

$$\vec{E}(\vec{r}) = a_0 \left[E_\theta(\theta, \phi) \hat{e}_\theta + E_\phi(\theta, \phi) \hat{e}_\phi + 0 \cdot \hat{e}_r \right] \frac{e^{ikr}}{kr},$$

where $E_\theta(\theta, \phi)$ and $E_\phi(\theta, \phi)$ are known functions, a_0 is the excitation, and angles θ and ϕ are related to the propagation vector \vec{k} by

$$\theta = \cos^{-1} \left[\frac{k_z}{k} \right]$$

and

$$\phi = \tan^{-1} \left[\frac{k_y}{k_x} \right].$$

It has been shown that $\vec{E}(\vec{r})$ can be expressed in terms of the Fourier transform of the components of $\vec{E}(\vec{r})$ that lie in the x-y plane. The Fourier transform of those components is commonly referred to as the angular spectrum (of plane waves) of $\vec{E}(\vec{r})$ and is denoted here by $\vec{B}(\vec{k})$. Using the method of stationary phase, the angular spectrum of $\vec{E}(\vec{r})$ can be related to the far-field E-field, making the above expression for $\vec{E}(\vec{r})$ equivalent to

$$\vec{E}(\vec{r}) = \iint \vec{B}(\vec{k}) e^{i\vec{k} \cdot \vec{r}} dk_x dk_y,$$

where

$$\vec{B}(\vec{k}) = \frac{ia_0}{2\pi k^2 \cos \theta} \left[E_\theta(\theta, \phi) \hat{e}_\theta + E_\phi(\theta, \phi) \hat{e}_\phi \right],$$

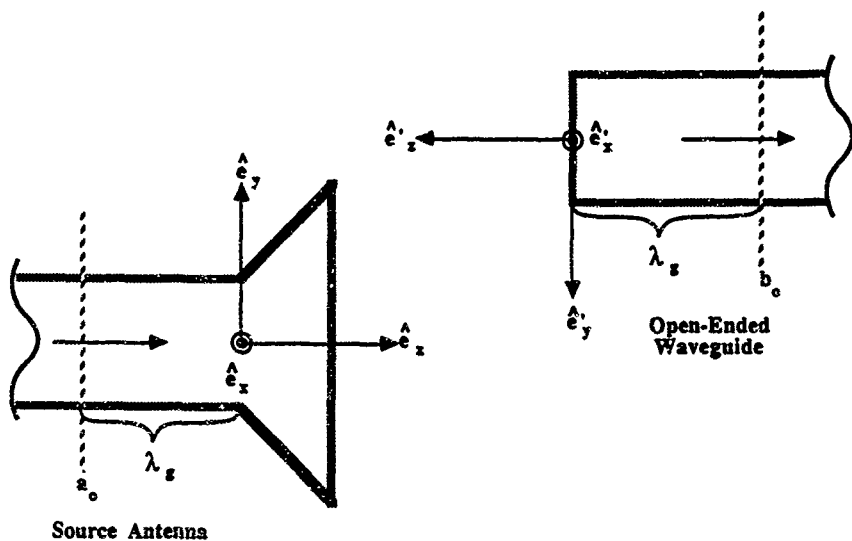


Figure B-4. Coordinate Conventions for Horn Measurements

or, in more general notation,

$$\tilde{s}_{10}(\vec{k}) = \frac{i}{2\pi k^2 \cos \theta} \lim_{|r| \rightarrow \infty} \left[k r e^{-i\vec{k} \cdot \vec{r}} \tilde{E}(\vec{r}) \right].$$

These plane waves propagate from the antenna to the origin O' of the primed coordinate system. When they reach O' , they are shifted in phase by a factor $e^{ik_z d}$, so the field transmitted to O' , expressed in terms of coordinate system O, is

$$\tilde{E}(0,0,d) = \frac{ia_0}{2\pi k^2} \iint \left[\frac{E_\theta(\theta, \phi) \hat{e}_\theta + E_\phi(\theta, \phi) \hat{e}_\phi}{\cos(\theta)} \right] e^{ik_z d} dk_x dk_y.$$

If now the probe is scanned over the plane $z=d$, we introduce an additional phase factor to get

$$\tilde{E}(x,y,d) = \frac{ia_0}{2\pi k^2} \iint \left[\frac{E_\theta(\theta, \phi) \hat{e}_\theta + E_\phi(\theta, \phi) \hat{e}_\phi}{\cos(\theta)} \right] e^{i(k_x x + k_y y)} e^{ik_z d} dk_x dk_y.$$

Having established the incident field at the OEWG as a summation of plane waves, the next step is to calculate the OEWG excitation b_0 due to a single incident plane wave. Consider a plane wave

$$\tilde{E}(\vec{r}') = [E_\theta(\theta', \phi') \hat{e}_\theta + E_\phi(\theta', \phi') \hat{e}_\phi] \delta(k'_x - k_{x_0}) \delta(k'_y - k_{y_0})$$

with propagation vector \vec{k}' , expressed in terms of coordinate system O' , incident upon an open-ended waveguide. It was shown above that

$$b_0 = \frac{-4\pi i}{abk^2 \sqrt{1 - \left(\frac{\pi}{ka}\right)^2}} \cdot \frac{A_E}{E_0} \cdot [E'_\theta(\theta', \phi') f_\theta(\theta', \phi') + E'_\phi(\theta', \phi') f_\phi(\theta', \phi')]$$

where $f'_\theta(\theta', \phi')$ and $f'_\phi(\theta', \phi')$ are the known pattern factors of the OEWG:

$$\tilde{E}_{\text{OEWG}}(\vec{r}) = A_E \frac{e^{ikr}}{kr} [f_\theta(\theta', \phi') \hat{e}_\theta + f_\phi(\theta', \phi') \hat{e}_\phi].$$

In fact, a plane wave from the antenna at O , and incident upon the OEWG at O' , in the unprimed coordinates of the antenna under test, is

$$E'_\theta(\theta, \phi) = \frac{ia_0 e^{ik_z d}}{2\pi k^2 \cos \theta} E_\theta(\theta, \phi) e^{i(k_x x + k_y y)}$$

$$E_{\phi}(\theta, \phi) = \frac{ia_0 e^{ik_z d}}{2\pi k \cos \theta} E_{\phi}(\theta, \phi) e^{i(k_x x + k_y y)}$$

$$b_0 = \frac{A_E}{E_0} \cdot \frac{-4\pi i}{abk^4 \sqrt{1 - \left[\frac{\pi}{ka}\right]^2}} \frac{ia_0 e^{ik_z d}}{2\pi \cos(\theta)} e^{i(k_x x + k_y y)} \left[E_{\theta}(\theta, \phi) \cdot f_{\theta}(\theta', \phi') + E_{\phi}(\theta, \phi) \cdot f_{\phi}(\theta', \phi') \right]$$

Simplifying, and using the relations

$$f_{\theta}(\theta, \phi) = f_{\theta}(\theta', \pi - \phi')$$

$$f_{\phi}(\theta, \phi) = f_{\phi}(\theta', \pi - \phi')$$

where $\theta' = \theta$ and $\phi' = \pi - \phi$, we get

$$b_0 = a_0 \frac{A_E}{E_0} \cdot \frac{-2ie^{ik_z d} e^{i(k_x x + k_y y)}}{abk^4 \sqrt{1 - \left[\frac{\pi}{ka}\right]^2} \cos(\theta)} \left[E_{\theta}(\theta, \phi) f_{\theta}(\theta, \pi - \phi) + E_{\phi}(\theta, \phi) f_{\phi}(\theta, \pi - \phi) \right]$$

Summing over a continuum of plane waves:

$$b_0 = \frac{A_E}{E_0} \cdot \frac{-2ia_0}{abk^4 \sqrt{1 - \left[\frac{\pi}{ka}\right]^2}} \left[\frac{E_{\theta}(\theta, \phi) f_{\theta}(\theta, \pi - \phi) + E_{\phi}(\theta, \phi) f_{\phi}(\theta, \pi - \phi)}{\cos(\theta)} \right] e^{ik_z d} e^{i(k_x x + k_y y)} dk_x dk_y$$

The above is a complete and rigorous description in the coordinate system of the antenna under test. In general, however, the measurements will be made in a coordinate system that is attached to a fixed point on the scanning table, and is thus defined by

$$\begin{bmatrix} x'' \\ y'' \\ z'' \end{bmatrix} = \begin{bmatrix} 1 & 0 & 0 \\ 0 & -1 & 0 \\ 0 & 0 & -1 \end{bmatrix} \cdot \begin{bmatrix} x - x_0 \\ y - y_0 \\ z - d \end{bmatrix},$$

where the origin of the coordinate system is at the probe antenna coordinates $O'' = (x_0, y_0, d)$. Hence, after taking the data, the first step of the analysis is to convert from the doubly-primed coordinate system of the scanning table to the unprimed

coordinate system of the antenna under test. We now have

$$\begin{bmatrix} x \\ y \end{bmatrix} = \begin{bmatrix} 1 & 0 \\ 0 & -1 \end{bmatrix} \begin{bmatrix} x'' \\ y'' \end{bmatrix} + \begin{bmatrix} x_0 \\ y_0 \end{bmatrix}$$

$$z = d,$$

$$\theta = \sin^{-1} \left[\frac{z}{\sqrt{x^2 + y^2}} \right]$$

$$\phi = \tan^{-1} \left[\frac{y}{x} \right].$$

D. PROBE ANTENNA CHARACTERISTIC

The transmit characteristic of the probe antenna is related to its far-field E-field by [5]

$$\vec{s}_{10}(\vec{k}) = \frac{i}{2\pi k^2 \cos \theta} \lim_{r \rightarrow \infty} \left\{ kr e^{-i\vec{k} \cdot \vec{r}} \cdot \vec{E}(\vec{r}) \right\},$$

where \vec{k} is parallel to \vec{r} . Assuming a reciprocal antenna, the receiving characteristic is

$$\vec{r}_{01}(\vec{k}) = \frac{Y_0 \cos(\theta)}{\eta_0} \vec{s}_{10}(-\vec{k}).$$

The constants Y_0 and η_0 are admittances that may be normalized to unity. If we wish to perform an absolute measurement, it will be necessary to specify the ratio Y_0/η_0 exactly. To do so, we return to the expression for the received signal derived earlier

$$b_0 = \frac{-2ia_0}{abk^4 \sqrt{1 - \left[\frac{x}{k-a} \right]^2}} \left[\int \frac{E_\theta(\theta, \phi) f_\theta(\theta, \pi - \phi) + E_\phi(\theta, \phi) f_\phi(\theta, \pi - \phi)}{\cos(\theta)} e^{ik_2 d} \right. \\ \left. e^{i(k_x x + k_y y)} dk_x dk_y \right].$$

This we compare to the expression

$$b(\vec{r}) = \frac{1}{4\pi^2} \iint \vec{r}_{01}(\vec{K}) \cdot \vec{s}(\vec{k}) e^{i\vec{k} \cdot \vec{r}} d\vec{K}.$$

We now consider the transmit antenna to be an OEWG with excitation E_0 . We have therefore

$$b_0 = \frac{-2iA_E}{abk^4 \sqrt{1 - \left[\frac{\pi}{ka}\right]^2}} \frac{A_E}{E_0} \iint \frac{f_\theta(\theta, \phi) f_\theta(\theta, \pi - \phi) + f_\phi(\theta, \phi) f_\phi(\theta, \pi - \phi)}{\cos(\theta)} e^{ik_z d} e^{i(k_x x + k_y y)} dk_x dk_y,$$

where b_0 , A_E , and E_0 are all in units of volts/meter. By equating the two expressions we get

$$\frac{1}{4\pi^2} \vec{r}_{01}(\vec{k}) \cdot \vec{s}_{10}(\vec{k}) = \frac{-2\pi i}{abk^4 \sqrt{1 - \left[\frac{\pi}{ka}\right]^2}} \left[\frac{A_E}{E_0} \right]^2 \frac{\vec{f}(\vec{k}) \cdot \vec{f}(-\vec{k})}{\cos \theta}.$$

From a previous section we have

$$\begin{aligned} \vec{s}_{10}(\vec{k}) &= \frac{i}{2\pi k^2 \cos \theta} \lim_{|\vec{r}| \rightarrow \infty} \left[k\vec{r} e^{-i\vec{k} \cdot \vec{r}} \vec{E}(\vec{r}) \right] \\ \vec{s}_{10}(\vec{k}) &= \frac{i}{2\pi k^2 \cos \theta} A_E \vec{f}(\vec{k}). \end{aligned}$$

Furthermore,

$$\begin{aligned} \vec{r}_{01}(\vec{k}) &= \frac{Y_0}{\eta_0} \cos \theta \vec{s}_{10}(-\vec{k}) \\ &= \frac{Y_0}{\eta_0} \frac{i}{2\pi k^2 \cos \theta} A_E \vec{f}(-\vec{k}). \end{aligned}$$

Substituting, we get

$$\begin{aligned} \frac{1}{4\pi^2} \frac{Y_0}{\eta_0} \frac{-A_E^2}{4\pi^2 k^4 \cos \theta} &= \frac{-2\pi i}{abk^4 \sqrt{1 - \left[\frac{\pi}{ka}\right]^2}} \left[\frac{A_E}{E_0} \right]^2 \frac{1}{\cos \theta} \\ \frac{Y_0}{\eta_0} &= \frac{32\pi^5 i}{E_0 ab \sqrt{1 - \left[\frac{\pi}{ka}\right]^2}}. \end{aligned}$$

Hence,

$$\begin{aligned} \vec{r}_{01}(\vec{k}) &= \frac{Y_0 \cos \theta}{\eta_0} \vec{s}_{10}(-\vec{k}) \\ \vec{r}_{01}(\vec{k}) &= \frac{-16\pi^4 \cos \theta}{ab \sqrt{1 - \left[\frac{\pi}{ka}\right]^2}} \frac{1}{k^2 \cos \theta} \frac{A_E}{E_0} \vec{f}(-\vec{k}) \end{aligned}$$

for an OEWG, or

$$\vec{r}_{01}(\vec{k}) = \frac{-16\pi^4}{ab \sqrt{1 - \left[\frac{\pi}{k a}\right]^2}} \frac{1}{k^2 \cos \theta E_0} \lim_{|r| \rightarrow \infty} \left[k r e^{-i\vec{k} \cdot \vec{r}} \vec{E}(\vec{r}) \right]$$

where $\vec{E}(\theta, \phi)$ is the transmitted field due to an excitation E_0 in an OEWG

$$\vec{E}^{ex}(x) = E_0 \cos \frac{\pi x}{a} \hat{e}_y.$$

E. FAR FIELD OF PYRAMIDAL HORN ANTENNA

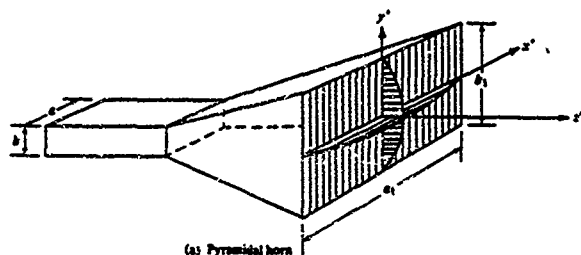
The pyramidal horn probe antenna has the advantage that it has higher gain, which increases the signal-to-noise ratio (SNR) on-axis. Of course, the horn's higher directivity reduces the SNR off-axis, and the presence of nulls in the horn pattern is undesirable. Since the horn antenna is well-characterized, it is also a good choice for a test antenna for near-field antenna measurements.

The following discussion of the pattern of the pyramidal horn is taken from Balanis [6]. The pyramidal horn geometry is shown in Figure B-5 (Balanis' Figure 12.18). The following parameters are assumed to be known:

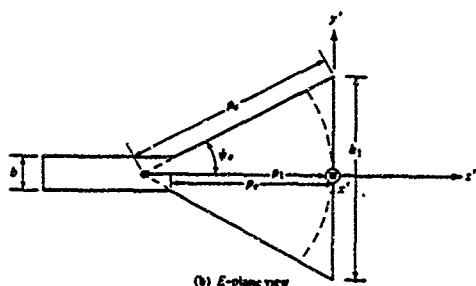
- $a \equiv$ waveguide feed dimension (larger), along \hat{e}_x ,
- $b \equiv$ waveguide feed dimension (smaller), along \hat{e}_y ,
- $a_1 \equiv$ horn dimension (larger), along \hat{e}_x ,
- $b_1 \equiv$ horn dimension (smaller), along \hat{e}_y ,
- $\rho_1 \equiv$ distance from aperture to E-plane phase center,
- $\rho_2 \equiv$ distance from aperture to H-plane phase center,
- $E_0 \equiv$ waveguide excitation (TE₁₀ mode), and
- $\lambda \equiv$ free-space wavelength.

The tangential components of the E- and H-fields at the horn aperture are approximately

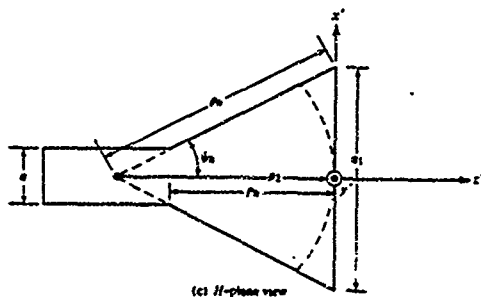
$$\begin{aligned} E_y'(x', y') &= E_0 \cos \left[\frac{\pi}{a_1} x' \right] e^{+ik \left[\frac{x'^2}{2\rho_2} + \frac{y'^2}{2\rho_1} \right]}, \\ H_x'(x', y') &= \frac{-E_y'(x', y')}{\eta}. \end{aligned}$$



(a) Pyramidal horn



(b) E-plane view



(c) H-plane view

Figure B-5. Pyramidal Horn and Coordinate Systems
(Figure 12.18 from Balanis)

The far-field E-field can be derived (after tedious manipulation)

$$E_r = 0,$$

$$E_\theta = E_0 \frac{-ik}{4\pi r} e^{+ikr} \left[\sin(\phi) \cdot [1 + \cos(\theta)] \cdot I_1 I_2 \right], \text{ and}$$

$$E_\phi = E_0 \frac{-ik}{4\pi r} e^{+ikr} \left[\cos(\phi) \cdot [1 + \cos(\theta)] \cdot I_1 I_2 \right],$$

where

$$I_1 = \sqrt{\frac{\pi \rho_2}{4k}} \left\{ e^{-i \left[\frac{k_x'^2 \rho_2}{2k} \right]} \left\{ [C(t_2') - C(t_1')] + i[S(t_2') - S(t_1')] \right\} + \right. \\ \left. e^{-i \left[\frac{k_x''^2 \rho_2}{2k} \right]} \left\{ [C(t_2'') - C(t_1'')] + i[S(t_2'') - S(t_1'')] \right\} \right\},$$

$$I_2 = \sqrt{\frac{\pi \rho_1}{k}} \left\{ e^{-i \left[\frac{k_y^2 \rho_1}{2k} \right]} \left\{ [C(t_2) - C(t_1)] + i[S(t_2) - S(t_1)] \right\} \right\},$$

$$t_1 = \sqrt{\frac{1}{\pi k \rho_1}} \left\{ -\frac{k b_1}{2} - k_y \rho_1 \right\},$$

$$t_2 = \sqrt{\frac{1}{\pi k \rho_1}} \left\{ +\frac{k b_1}{2} - k_y \rho_1 \right\},$$

$$k = 2\pi/\lambda,$$

$$t_1' = \sqrt{\frac{1}{\pi k \rho_2}} \left\{ -\frac{k a_1}{2} - k_x' \rho_2 \right\},$$

$$t_2' = \sqrt{\frac{1}{\pi k \rho_2}} \left\{ +\frac{k a_1}{2} - k_x' \rho_2 \right\},$$

$$k_x' = k \sin(\theta) \cos(\phi) + \pi/a_1,$$

$$t_1'' = \sqrt{\frac{1}{\pi k \rho_2}} \left\{ -\frac{k a_1}{2} - k_x'' \rho_2 \right\},$$

$$t_2'' = \sqrt{\frac{1}{\pi k \rho_2}} \left\{ + \frac{k a_1}{2} - k_x'' \rho_2 \right\},$$

$$k_x'' = k \sin(\theta) \cos(\phi) - \pi/a_1,$$

$$k_y = k \sin(\theta) \sin(\phi);$$

and

$$C(x) = \int_0^x \cos \left[\frac{\pi t^2}{2} \right] dt$$

$$S(x) = \int_0^x \sin \left[\frac{\pi t^2}{2} \right] dt$$

are the Fresnel cosine and sine integrals.

We use the Narda 640 horn antenna at 10 Ghz driven by X-band waveguide.

Typical parameters are

$$a = .02286 \text{ m}$$

$$b = .01016 \text{ m}$$

$$a_1 = .0737 \text{ m},$$

$$b_1 = .0544 \text{ m},$$

$$\rho_1 = .0916 \text{ m},$$

$$\rho_2 = .1169 \text{ m}.$$

$$\lambda = .03 \text{ m}.$$

APPENDIX C

SCATTERING BY CONDUCTING SPHERE

The conducting sphere is a canonical object for which an analytical solution exists. In this appendix we present a solution [19] for scattering by a perfectly conducting sphere, followed by a derivation of the coordinate transformations necessary to utilize this solution in verifying the measured scattering matrix.

For convenience, we will work initially in an unprimed coordinate system. A perfectly conducting sphere of radius a is placed at the origin (Figure C-1) and is illuminated by a monochromatic incident plane wave traveling in the $+\hat{e}_z$ direction with x-polarization

$$\vec{k} = k_z \hat{e}_z$$

$$\vec{E}_{\text{inc}} = E_0 e^{i(k_z z - \omega t)} \hat{e}_x$$

Dropping the $e^{-i\omega t}$ dependency, write \vec{E}_{inc} in spherical form

$$\vec{E}_{\text{inc}} = E_0 \sum_{n=1}^{\infty} (i)^n \frac{2n+1}{n(n+1)} \left[\hat{m}_{\text{oln}}^{(1)} - i \hat{n}_{\text{eln}}^{(1)} \right]$$

where

$$\hat{m}_{\text{oln}}^{(1)} = \frac{j_n(k_2 R) \cdot P_n^1(\cos \theta) \cos \phi}{\sin \theta} \hat{e}_\theta - j_n(k_2 R) \frac{\partial P_n^1(\cos \theta)}{\partial \theta} \sin \phi \hat{e}_\phi$$

$$\hat{n}_{\text{eln}}^{(1)} = n(n+1) \cdot \frac{j_n(k_2 R)}{k_2 R} \cdot P_n^1(\cos \theta) \cos \phi \hat{e}_r +$$

$$\frac{1}{k_2 R} \frac{\partial [k_2 R j_n(k_2 R)]}{\partial (k_2 R)} \frac{\partial P_n^1(\cos \theta)}{\partial \theta} \cos \phi \hat{e}_\theta +$$

$$\frac{1}{k_2 R \sin \theta} \frac{\partial [k_2 R j_n(k_2 R)]}{\partial (k_2 R)} P_n^1(\cos \theta) \sin \phi \hat{e}_\phi$$

and

k_1 = propagation constant inside sphere,

k_2 = propagation constant outside sphere, and

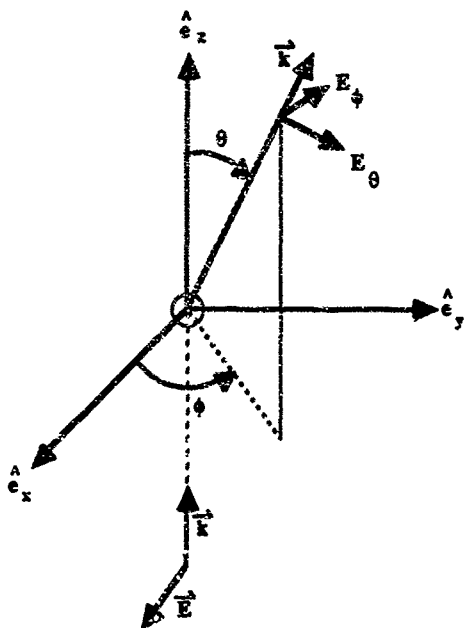


Figure C-1. Coordinate System for Sphere Scattering Prediction

R = radius to observation point.

For $R > a$, the scattered field will have the form

$$\vec{E}^s = E_0 \sum_{n=1}^{\infty} (i)^n \frac{2n+1}{n(n+1)} \left[a_n^r \cdot \vec{m}_{01n}^{(3)} - i b_n^r \cdot \vec{n}_{e1n}^{(3)} \right],$$

where

$$\begin{aligned} \vec{m}_{01n}^{(3)} &= \pm \frac{h_n^{(1)}(k_2 R) \cdot P_n^1(\cos \theta) \cos \phi}{\sin \theta} \hat{e}_\theta - h_n^{(1)}(k_2 R) \cdot \frac{\partial P_n^1(\cos \theta)}{\partial \theta} \sin \phi \hat{e}_\phi \\ \vec{n}_{e1n}^{(3)} &= n(n+1) \frac{h_n^{(1)}(k_2 R)}{k_2 R} \cdot P_n^1(\cos \theta) \cos \phi \hat{e}_r + \\ &\quad \frac{1}{k_2 R} \frac{\partial [k_2 R h_n^{(1)}(k_2 R)]}{\partial (k_2 R)} \frac{\partial P_n^1(\cos \theta)}{\partial \theta} \cos \phi \hat{e}_\theta \pm \\ &\quad \frac{1}{k_2 R \sin \theta} \frac{\partial [k_2 R h_n^{(1)}(k_2 R)]}{\partial (k_2 R)} \cdot P_n^1(\cos \theta) \sin \phi \hat{e}_\phi. \end{aligned}$$

We define

$$k_1 = N \cdot k_2,$$

$$\rho = k_2 \cdot a,$$

so

$$k_1 \cdot a = N \cdot \rho.$$

The boundary condition at $R = a$ requires that

$$a_n^r = \frac{-\mu_1 j_n(N\rho) \frac{\partial}{\partial \rho} \left[\rho j_n(\rho) \right] - \mu_2 j_n(\rho) \frac{\partial}{\partial (N\rho)} \left[N\rho j_n(N\rho) \right]}{\mu_1 j_n(N\rho) \frac{\partial}{\partial \rho} \left[\rho h_n^{(1)}(\rho) \right] - \mu_2 h_n^{(1)}(\rho) \frac{\partial}{\partial (N\rho)} \left[N\rho j_n(N\rho) \right]}$$

and

$$b_n^r = \frac{-\mu_1 j_n(N\rho) \frac{\partial}{\partial (N\rho)} \left[N\rho j_n(N\rho) \right] - \mu_2 N^2 j_n(N\rho) \frac{\partial}{\partial \rho} \left[\rho j_n(\rho) \right]}{\mu_1 h_n^{(1)}(\rho) \frac{\partial}{\partial (N\rho)} \left[N\rho j_n(N\rho) \right] - \mu_2 N^2 j_n(N\rho) \frac{\partial}{\partial \rho} \left[\rho h_n^{(1)}(\rho) \right]}.$$

The above equations are valid for a sphere with arbitrary dielectric properties. If the sphere is aluminum, and the surrounding medium is air, then

$$\mu_1 = \mu_2 = \mu_0 = 1.257 \times 10^{-6} \text{ henry/meter,}$$

$$\epsilon_1 = \epsilon_2 = \epsilon_0 = 8.854 \times 10^{-12} \text{ farad/meter,}$$

$$\sigma_1 = 3.5 \times 10^7 \text{ mho/meter, and}$$

$$\sigma_2 = 0.$$

The general form of the propagation constant is

$$k^2 = \epsilon\mu\omega^2 + i\omega\mu\sigma$$

$$= \epsilon\mu\omega^2(1 + i\eta),$$

where

$$\eta \equiv \frac{\sigma}{\epsilon\omega}.$$

$$\text{At } f = 10 \text{ Ghz,}$$

$$\eta_1 = \frac{\sigma_1}{\epsilon_1\omega} \approx 6.3 \times 10^7$$

so

$$k_1^2 \approx i\epsilon_1\mu_1\omega^2\eta_1, \text{ and}$$

$$k_1 \approx \pm \sqrt{i} \cdot 1.66 \times 10^6 \text{ /meter.}$$

Also,

$$k_2^2 = \epsilon_2\mu_2\omega^2$$

$$k_2 \approx 209.4 \text{ /meter.}$$

Choosing a 6-inch diameter sphere, $a = .0762$ meter, so

$$\rho = k_2 a$$

$$= 15.96$$

and

$$N\rho \approx \pm \sqrt{i} \cdot 1.26 \times 10^5 \text{ /meter.}$$

Since $|N\rho| \gg 1$, we can use the asymptotic relations

$$j_n(N\rho) \approx \frac{\cos \left[N\rho - \frac{n+1}{2}\pi \right]}{N\rho}$$

and

$$\frac{\partial [N \rho j_n(N\rho)]}{\partial(N\rho)} \approx -\sin \left[N\rho - \frac{n+1}{2}\pi \right]$$

to simplify the above equations for a_n^r and b_n^r , yielding

$$a_n^r \approx -\frac{j_n(\rho)}{h_n^{(1)}(\rho)}$$

$$b_n^r \approx -\frac{\frac{\partial}{\partial \rho} [\rho j_n(\rho)]}{\frac{\partial}{\partial \rho} [\rho h_n^{(1)}(\rho)]}$$

where

$$h_n^{(1)}(\rho) \equiv j_n(\rho) + i \cdot \eta_n(\rho).$$

After the usual sort of manipulation,

$$E_\theta^r = E_0 \frac{e}{iK_2 R} \cos(\phi) \sum_{n=1}^{\infty} \frac{2n+1}{n(n+1)} \left\{ a_n^r \frac{P_n^1(\cos \theta)}{\sin \theta} + b_n^r \frac{\partial [P_n^1(\cos \theta)]}{\partial \theta} \right\}$$

and

$$E_\phi^r = -E_0 \frac{e}{iK_2 R} \sin(\phi) \sum_{n=1}^{\infty} \frac{2n+1}{n(n+1)} \left\{ a_n^r \frac{\partial [P_n^1(\cos \theta)]}{\partial \theta} + b_n^r \cdot P_n^1(\cos \theta) \right\}.$$

APPENDIX D

SCATTERING BY CONDUCTING DISK

To calculate scattering from a conducting disk we use a physical optics solution due to Capt. Keith Trott of RADC. Using the theory of physical optics [20], on a scattering object

$$\mathbf{J}^s \cong 2 \hat{n} \times \hat{H}$$

where

$\mathbf{J}^s \equiv$ total surface current,

$\hat{n} \equiv$ unit normal vector pointing away from surface,

$\hat{H} \equiv$ incident H field.

This is a good approximation for large objects but tends to break down with smaller objects because it is not valid near edges. If the incident plane wave \hat{E} is known, then one can compute, in sequence, \hat{H} , \mathbf{J} , and the vector potential

$$\vec{A} = \frac{1}{4\pi} \iint \frac{\mathbf{J}^s e^{+ik|\vec{r}-\vec{r}'|}}{|\vec{r}-\vec{r}'|} dS'$$

and the scattered E-field is

$$\vec{E} = \frac{-1}{i\omega\epsilon_0} \vec{\nabla} \times \vec{\nabla} \times \vec{A}.$$

In the unprimed frame the disk is at the origin (Figure C-1), lies in the x-y plane, and has radius a. It is illuminated from above the x-y plane by the incident wave vector

$$\vec{k}_i = -(\cos\phi_1 \sin\theta_1 \cdot \hat{e}_x + \sin\phi_1 \sin\theta_1 \cdot \hat{e}_y + \cos\theta_1 \cdot \hat{e}_z) |\vec{k}|.$$

Assume \vec{k}_i lies in the x-z plane, so $\phi_1=0$, and

$$\vec{k}_i = -(\sin\theta_1 \cdot \hat{e}_x + 0 \cdot \hat{e}_y + \cos\theta_1 \cdot \hat{e}_z) |\vec{k}_i|.$$

The observation location is also above the x-y plane at

$$\begin{aligned} \vec{r} &= x \cdot \hat{e}_x + y \cdot \hat{e}_y + z \cdot \hat{e}_z \\ &= r (\cos\phi \sin\theta \hat{e}_x + \sin\phi \sin\theta \hat{e}_y + \cos\theta \hat{e}_z), \end{aligned}$$

so

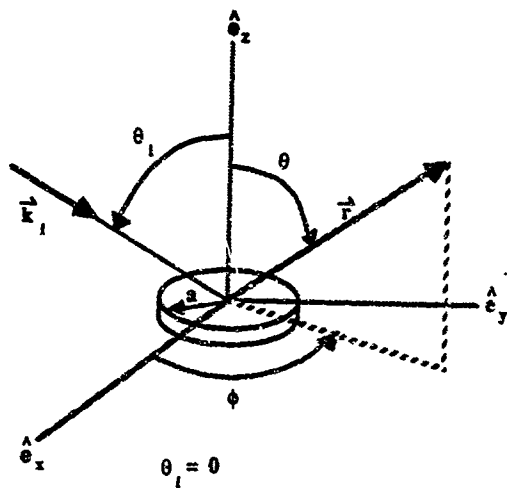


Figure D-1. Coordinate System for Disk Scattering Prediction

$$\vec{k}_1 \cdot \vec{r} = -k_1 r (\sin \theta_1 \cos \phi \sin \theta + \cos \theta_1 \cos \theta).$$

The plane of incidence is defined by \vec{k}_1 and \hat{e}_z . There are two polarizations of the incident field — parallel and perpendicular to the plane of incidence. An arbitrary planar illumination \vec{E}_0 with \vec{k}_1 ($\phi_1=0$) can be expressed in terms of those two polarizations:

$$\vec{E}_{\parallel} = E_{0\parallel} e^{+i\vec{k}_1 \cdot \vec{r}} (-\cos \theta_1 \hat{e}_x + \sin \theta_1 \hat{e}_z)$$

$$\vec{E}_{\perp} = E_{0\perp} e^{+i\vec{k}_1 \cdot \vec{r}} \hat{e}_y$$

Considering the parallel polarization first, we have

$$\vec{H} = \frac{E_{0\parallel}}{\eta} e^{+i\vec{k}_1 \cdot \vec{r}} \hat{e}_y$$

On the disk ($\theta'=\pi/2$) we use primed coordinates to indicate a source, so

$$\vec{H} \Big|_{\theta=\pi/2} = \frac{E_{0\parallel}}{\eta} e^{-ikr' \sin \theta_1 \cos \phi} \hat{e}_y$$

Then

$$\begin{aligned} \vec{J}^s(\vec{r}') &= 2 \hat{e}_z \times \vec{H} \Big|_{\theta=\pi/2} \\ &= \frac{-2E_{0\parallel}}{\eta} e^{-ikr' \sin \theta_1 \cos \phi'} \hat{e}_x \end{aligned}$$

The observation point is

$$\vec{r} = |\vec{r}| (\cos \phi \sin \theta \hat{e}_x + \sin \phi \sin \theta \hat{e}_y + \cos \theta \hat{e}_z)$$

while on the disk itself $\theta'=\pi/2$, so

$$\vec{r}' = |\vec{r}| (\cos \phi' \hat{e}_x + \sin \phi' \hat{e}_y).$$

The factor $|\vec{r}-\vec{r}'|$ in the integral for \vec{A} is

$$\begin{aligned} |\vec{r}-\vec{r}'| &= \sqrt{(r \cos \phi \sin \theta - r' \cos \phi')^2 + (r \sin \phi \sin \theta - r' \sin \phi')^2 + r^2 \cos^2 \theta} \\ &= \sqrt{r^2 + r'^2 - 2rr' \sin \theta \cos(\phi - \phi')} \end{aligned}$$

In the denominator of the integral, $|\vec{r}-\vec{r}'|$ can be approximated by $|\vec{r}|$. In the numerator phase factor, a better approximation is required. Ignoring quadratic terms inside the radical, expanding in a Taylor series, and retaining the first two terms

$$|\vec{r}-\vec{r}'| \cong r - r' \sin \theta \cos(\phi - \phi').$$

Then

$$\tilde{A} = \frac{1}{4\pi r} \iint \left[\frac{-2E_{0\parallel}}{\eta} \hat{e}_x e^{-ikr' \sin \theta_1 \cos \phi'} + ik(r-r') \sin \theta \cos(\phi-\phi') \right] r' d\phi' dr'.$$

After tedious manipulation,

$$\begin{aligned} \tilde{A} &= \frac{-aE_{0\parallel}}{\eta r} e^{-ikr} \frac{J_1(k\Lambda z)}{k\Lambda} \hat{e}_x \\ &= \frac{-aE_{0\parallel}}{\eta r} e^{-ikr} \frac{J_1(k\Lambda z)}{k\Lambda} [\cos \theta \cos \phi \hat{e}_\theta - \sin \phi \hat{e}_\phi] \end{aligned}$$

where

$$\Lambda = \sqrt{\sin^2 \theta + \sin^2 \theta_1 + 2 \sin \theta_1 \sin \theta \cos \phi}.$$

In the far field, retaining r^{-1} terms only,

$$E_\theta = \eta H_\phi = +ik\eta A_\theta$$

$$E_\phi = -\eta H_\theta = +ik\eta A_\phi$$

so the scattered field due to parallel illumination is

$$\tilde{E}_{s\parallel} = iE_{0\parallel} e^{-ikr} \frac{a}{r\Lambda} J_1(ak\Lambda) [-\cos \theta \cos \phi \hat{e}_\theta + \sin \phi \hat{e}_\phi]$$

Considering perpendicular polarization,

$$\begin{aligned} \tilde{H} &= \frac{E_{0\perp}}{\eta} \left[\cos \theta_1 \hat{e}_x - \sin \theta_1 \hat{e}_z \right] e^{+ik\vec{r}_1 \cdot \vec{r}} \\ &= \frac{E_{0\perp}}{\eta} \left[\cos \theta_1 \hat{e}_x - \sin \theta_1 \hat{e}_z \right] e^{+ikr' \sin \theta_1 \cos \phi} \end{aligned}$$

Then

$$\begin{aligned} \tilde{J} &= \frac{2E_{0\perp}}{\eta} \cos \theta_1 e^{+ikr' \sin \theta_1 \cos \phi} \hat{e}_y \\ \tilde{A} &= \frac{E_{0\perp}}{\eta r} \cos \theta_1 a \frac{J_1(ka\Lambda)}{k\Lambda} \hat{e}_y \\ &= \frac{E_{0\perp}}{\eta r} \cos \theta_1 a \frac{J_1(ka\Lambda)}{k\Lambda} [\cos \theta \sin \phi \hat{e}_\theta + \cos \phi \hat{e}_\phi] \end{aligned}$$

and the scattered field due to perpendicular illumination is

$$\tilde{E}_{s\perp} = +iE_{0\perp} e^{+ikr} \frac{a}{r\Lambda} J_1(ak\Lambda) [\cos \theta_1 (\cos \theta \sin \phi \hat{e}_\theta + \cos \phi \hat{e}_\phi)]$$

Since $\tilde{E}_{s\parallel}$ and $\tilde{E}_{s\perp}$ have identical time phase, the scattered E-field is

$$\begin{bmatrix} E_{s\theta} \\ E_{s\phi} \end{bmatrix} = +i \frac{e^{-ikr}}{kr} \frac{a}{\Lambda} J_1(ka\Lambda) \begin{bmatrix} -\cos \theta \cos \phi & \cos \theta_1 \cos \theta \sin \phi \\ \sin \phi & \cos \theta_1 \cos \phi \end{bmatrix} \cdot \begin{bmatrix} E_{0\parallel} \\ E_{0\perp} \end{bmatrix}.$$



MISSION of Rome Air Development Center

RADC plans and executes research, development, test and selected acquisition programs in support of Command, Control, Communications and Intelligence (C²I) activities. Technical and engineering support within areas of competence is provided to ESD Program Offices (POs) and other ESD elements to perform effective acquisition of C²I systems. The areas of technical competence include communications, command and control, battle management information processing, surveillance sensors, intelligence data collection and handling, solid state sciences, electromagnetics, and propagation, and electronic reliability/maintainability and compatibility.